SCUOLA DI DOTTORATO
UNIVERSITÀ DEGLI STUDI DI MILANO-BICOCCA

Department of Earth and Environmental Sciences

PhD program: Chemical, Geological and Environmental Sciences Cycle XXXVI

Curriculum - Geological sciences

Quantitative evaluation of rock fracturing state across scales using Infrared Thermography: theoretical analysis, experimental modeling and upscaling to in situ conditions

Cotutel thesis

UNIL | Université de Lausanne

Surname: Franzosi Name: Federico

Registration number: 790260

Tutor: Prof. Frattini Paolo

Supervisor: Prof. Agliardi Federico

Co-supervisor: Prof. Jaboyedoff Michel

Coordinatore / Coordinator: Prof. Malusà Marco G.

ANNO ACCADEMICO / ACADEMIC YEAR 2022/2023

Table of contents

Abstract

The fracturing state of rocks is a fundamental control on their hydro-mechanical properties at all scales. In fact, reliable in situ quantification of rock mass fracturing and its engineering quality is critical for slope stability, surface mining and rock engineering applications.

Fracturing state can be quantified in the laboratory by non-destructive geophysical techniques that are hardly applicable in situ, where biased mapping and statistical sampling strategies are commonly used. Infrared thermography (IRT) has been used to infer the fracturing state of rock masses by measuring their thermal response to thermal perturbations, but a physics-based predictive approach is lacking. Our work focused on the investigation of the process of thermal perturbation in rock volumes at different scales to answer different research questions:(a) Is it possible to find a physical link between degree of fracturing and thermal response of the fractured rocks put to thermal perturbations (e.g., heating, cooling)? (b) Is it possible to meaningfully measure differences in behavior between media characterized by different degrees of fracturing using IRT? (c) Is it possible to quantify these differences to develop quantitative diagnostic methodologies for fracturing degree assessment?

To this end, we started performing an experimental study on the cooling behavior of pre-fractured gneiss and mica schist samples, whose 3D fracture networks were reconstructed using Micro-CT and quantified by unbiased fracture abundance measures. We carried out cooling experiments in both controlled (laboratory) and natural (outdoor) conditions, monitoring temperature with a thermal camera. Multi-temporal thermograms were processed to extract temperature distribution patterns and cooling temperature-time histories, described in terms of synthetic descriptors that show statistically significant correlations with fracture abundance measures. More intensely fractured rocks cool at faster rates and outdoor experiments shows that differences in thermal response can be detected even in natural environmental conditions. 3D FEM models reproducing laboratory experiments outline the fundamental control of fracture pattern and convective boundary conditions on cooling dynamics. Based on a lumped capacitance approach, we provided a synthetic description of cooling curves in terms of the Curve Shape Parameter (C_{SP}), independent of absolute thermal boundary conditions and lithology. This provides a

starting point toward the development of a quantitative methodology for the contactless in situ assessment of rock mass fracturing.

Then, starting from a robust theoretical framework and laboratory experimental investigation, we were able to explore the potential of the innovative IRT technique in predictive studies of the fracturing state of rock mass. To do this, it was necessary to translate the experience, theoretical aspects, and experimental approach developed in the laboratory to the in situ scale, through the characterization of the cooling behavior of rock mass outcrops using the C_{SP} *as a descriptor of outcrops cooling curves and function of fracturing.*

We based our approach to the problems on a systematic, sequential solution of the main upscaling issues, including: (a) definition of suitable rock mass quality descriptors, (b) scale effects affecting the definition of fractured rock masses; (c) environmental factor and disturbances controlling the applicability of IRT to rock mass characterization in outdoor settings, and (d) reconstruction and modelling of experimental cooling curves acquired in outdoor, unconstrained environmental conditions.

As a result of these studies, we propose a method to quantify and map the slope-scale geomechanical quality of fractured rock masses using Infrared thermography (IRT). We use the Mt. Gorsa quarry (Trentino, Italy) as a field laboratory to upscale the physics-based approach developed in the laboratory to in situ conditions, including the effects of fracture heterogeneity, environmental conditions and IRT limitations. We reconstructed the slope in 3D by UAV photogrammetry, characterized rock mass quality in the field at selected outcrops in terms of Geological Strength Index (GSI), and measured their cooling behavior through 18h time-lapse IRT surveys. With ad hoc field experiments, we developed a novel procedure to correct IRT data in outdoor environments with complex topography. This allowed a spatially distributed quantification of rock mass surface cooling behavior in terms of a Curve Shape Parameter (C_{SP}*) adjusted to outdoor conditions. Using nonlinear regression, we established a quantitative* C_{SP}*-GSI relationship allowed translating* C_{SP} *into GSI maps. Our results demonstrate the possibility to apply Infrared thermography to the slope-scale mapping of rock mass fracturing using a physics-based experimental methodology, which can potentially be useful in slope stability-related risk assessment for wide-ranging engineering problems.*

1 Introduction

This Ph.D. thesis investigates the effects and evolution of thermal perturbation in rock volumes at different scales in order to develop an innovative remote sensing approach for the study and characterization of rock mass fracturing state, with a focus on the use of the Infra-Red Thermography (IRT). The Ph.D project was carried out between November 2020 and November 2023.

The development of the analysis, and the resulting products, were carried out under a dual-degree co-tutorship agreement between the University of Milano-Bicocca (Italy) and the Université de Lausanne (Switzerland).

1.1 Aim of the work

Rock mass fracturing state is a fundamental parameter in the definition of the hydro-geomechanical properties of the rock mass. Different limitations of available in-situ techniques (low-resolution, dimensional and scale bias) represent a difficulty for quantitative characterization of the rock mass fracturing state, which remains a challenge.

Infra-Red Thermography (IRT), a promising application to rock-mechanics, is based on the study of the thermal response of rocks to different parameters (stress, saturation and porosity; Mineo & Pappalardo, 2016, 2019; Cai et al., 2020; Song et al., 2021), and is widely used for monitoring rock slope instability and for the study and characterization of rock mass geometries (Baroň et al., 2014; Mineo et al., 2015, 2022; Teza et al., 2015; Frodella et al., 2017; Guerin et al., 2019; Loiotine et al., 2022). Most applications are qualitative, based on the use of IRT images to identify and map fractures and damage at surface, and only few studies have proposed quantitative empirical approaches to relate the thermal response of rock masses to their geomechanical quality related to fracturing (Teza et al., 2012, Pappalardo et al. 2016, Grechi et al., 2021). These studies have indicated that the thermal behavior of rock masses during heating and cooling is related to their fracturing state.

The Ph.D project developed a physically-based, quantitative approach to the contactless characterization of rock fracturing states and rock mass quality using IRT, following a solid workflow (**Figure 1**) that can be divided into three work packages (WP):

- **WP1**: (a) Theoretical analysis of rocks fracturing state from a geological point of view, (b) study of physical processes and the factors controlling the cooling behavior of rocks with different degrees of fracturing and (c) theoretical and practical aspects of the experimental technology used in thermal monitoring of rock surfaces in this work using Infra-Red Thermography.
- **WP2**:(a) design and carry out innovative laboratory cooling experiments in which rock specimens with different fracturing states, quantified through non-destructive techniques (X-Ray CT), were heated and then cooled while being monitored in time lapse by Infrared Thermography and (b) develop a novel quantitative approach, based on a physical theory, to model cooling histories by means of a synthetic scalar descriptor that correlates well with unbiased fracture abundance measures;
- **WP3**:(a) upscale the approach developed in the laboratory to the in situ fractured rock mass scale, through the experimental analysis of the different environmental factors that affect the ability of IRT to significantly detect differences in the cooling behaviors of rock masses with different geomechanical quality; (b) develop a practical, contactless approach to correlate the in situ cooling behavior of rock masses and their Geological Strength Index, using the Mt. Gorsa Quarry (Trentino, Italy) as a natural laboratory.

1.2 Thesis structure

The thesis is organized into six chapters:

- **Chapter 1**: in this chapter, the generic and framing aspects of the thesis are expressed from the institutional and time perspective and the purpose of the research is articulated.
- **Chapter 2 (WP1)**: this chapter is the introduction to the theoretical aspects of rock fracturing state, starting with fracture definition, their attributes and in their important role in defining the physical characteristics of the rock mass. This chapter also discusses the main techniques and strategies of fracture detection and fracture state characterization, exposing their strengths and limitations.
- **Chapter 3 (WP1)**: this chapter focuses on analyzing the physical process that links the fracture state to the thermal behavior of a rock volume. To build our experimental hypothesis, key concepts of heat transport through matter were

explored, focusing on the dynamics of cooling a body in a physical system and by the processes of conduction and convection that govern it.

Secondly it also addresses the theoretical and practical aspects of the experimental technology used in the thermal monitoring of rock surfaces (IRT), from the physical principles that explain its functioning, to the main factors controlling laboratory and in situ measurements. This chapter also discusses the main applications of IRT in the field of applied geology in the current state of the art.

- **Chapter 4 (WP2)**: this chapter illustrates the first experimental step of the Ph.D. project (based on the article published concurrently with the execution of this thesis (Franzosi et al., 2023a). It shows how it was possible to link the fracture state of cylindrical rock specimens (reconstructed by X-ray microtomography) to their cooling dynamics, through forced heating and controlled cooling experiments in the laboratory, monitoring their surface temperature was monitored using an IR camera. Analyses on the experimental data were conducted according to the theoretical approach derived from the aspects addressed in Chapter 3.

- **Chapter 5 (WP3)**: this chapter illustrates the second experimental step of this work (based on the paper published concurrently with the execution of this thesis, (Franzosi et al., 2023b). This step involved the upscaling of the approach used at the laboratory scale to investigate the fracturing state of a rock mass by monitoring its natural night-time cooling. A natural laboratory, the Mt. Gorsa (TN) quarry, was selected, at which remote measurements of the rock face were carried out using an IR camera, and contextual measurements of the fracture state on the rock-mass wall were made.
- **Chapter 6**: general discussion and final remarks of the results and evidence obtained from the experimental workflow used in the overall work, with emphasis on the innovative aspects and comparison of experimental approaches and the results of both in laboratory and *in situ* investigations.

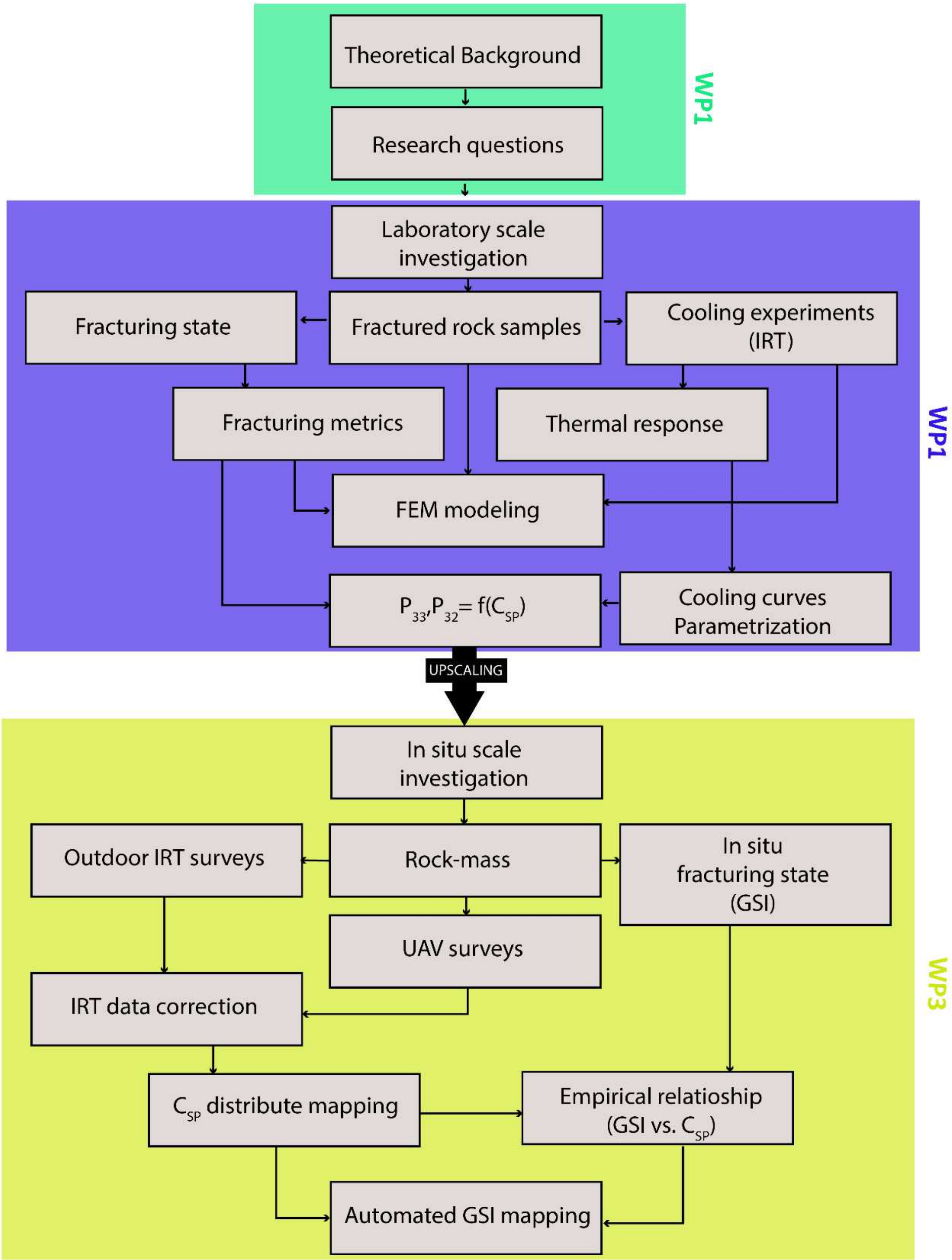

Figure 1 *Workflow of the entire project, divided into work packages (WP)*

2 Rock fractures and fracturing state

The fracturing state of rocks, defined as the abundance of fractures, is a fundamental control on their geomechanical properties including strength, stiffness and permeability (Oda et al., 1985, Hoek & Brown, 1997; Paterson & Wong, 2005; Hoek & Diederichs, 2006; Rutqvist et al., 2015). In turn, these properties strongly affect the hydro-mechanical behaviour (i.e permeability, strength) of fractured media at any scale of consideration (Hoek, 1983; Hoek & Brown, 1997; Rutqvist & Stephansson, 2003). Fracturing is also the main indicator of the damage state of rock masses, tracking brittle deformation processes across faults (Brideau et al., 2009; Peacock et al., 2017), around underground excavations (Cai et al., 2004; Martino & Chandler, 2004), and in natural and artificial slopes (Eberhardt et al., 2004; Agliardi et al., 2013; Riva et al., 2018). For these reasons, a reliable assessment of the fracturing state of rocks is critical to several geological, engineering and geohazard applications. These include understanding natural and induced seismicity (Gu et al., 1984; Rawling et al., 2001), the characterization of fractured reservoirs for water, hydrocarbon, and geothermal exploitation (Dershowitz & Miller, 1995; Gischig et al., 2020), and the assessment of rock mass properties for stability modelling of slopes and underground excavations in rocks (Hoek & Brown, 1997; Pine & Harrison, 2003; Wyllie & Mah, 2004; Brideau et al., 2009).

Figure 2 *Example of fractured rock-mass at Monte Gorsa quarry-site (TN, Northern Italy).*

The state of fracturing is a complex geological aspect that can be described and defined at different scales of observation (Krauland et al., 1989; Edelbro, 2004), and it can develop heterogeneously in different dimensions accompanying the rock medium in the transition between *intact rock*, *fractured rock* and *rock mass* (**Figure 2**).

As highlighted before, it is important to characterize the fracture state but it is also remained challenging and requires:

- Analysis of the processes that generate the fractures and control their geometry and spatial distribution.
- Sampling of fractures, considering size and scale issues and biases that could affect fracture quantification.
- Definition of quantitative parameters to describe the attributes of position, orientation, frequency, and size of fractures, useful in defining the abundance of fracture features in the space.
- Definition of correct techniques for fracturing quantification.

2.1 Fractures as discontinuities

Planar features in geological systems can have very different origins (ISRM, 1978; Priest & Hudson, 1981; Priest, 1993; Gudmundsson, 2011; Fossen, 2016) but on a geomechanical point of view they are grouped into structural *discontinuities* (Schultz, 2019) defined as all significant mechanical breaks or fractures of negligible tensile strength, low shear strength and high fluid conductivity in rocks, regardless of their age, geometry and origins (Priest, 1993).

Discontinuities can be mainly classified by their origin;

Fractures: defined as any discontinuity in rocks where, to simplify, the cohesion has been lost during a sequence of brittle deformations stages, associated with tectonic deformation, exhumation, and landscape development, affecting rock volume in the Earth’s crust during its geological history at large scales (Fossen, 2016; Lai et al., 2022). Fractures can be resumed in different features such as:

> *Joints*: Extensional joints are discontinuities formed by normal stress, opened in direction of minimum tensile strength, with no evidence of parallel slip-on wall surfaces. They can be associated to different geological processes, (i.e exhumation,

rapid cooling, hydrofracturing etc..). If some offset is present but negligible, joints could also be classified as shear joints.

Shear fractures: discontinuities formed by shear stress, on which surfaces have clearly visible evidence of fracture-parallel movements. Shear fractures are normally referred to as *faults*.

Bedding planes: strongly continuous discontinuities, present in sedimentary rock-masses marking an interruption in sedimentation, corresponding with following surfaces of deposition. They are usually parallel one to each other but can be strongly folded by geological deformation processes.

Foliation: plane surfaces present in mineral fabric of metamorphic rock-masses, created by re-orientation or recrystallization of platy minerals during metamorphic processes.

On natural outcrops, all these kind of discontinuities are generally organized into several sets with the same geometric characteristics whose orientation and intensity depends on the large-scale brittle geological processes that have affected the region (Einstein & Dershowitz, 1990; Fossen, 2016). Rock masses can thus be defined as a natural rock volumes subdivided into discrete blocks by these discontinuity sets (**Figure 1**; Hoek, 1983; Krauland et al., 1989; Hoek & Brown, 1997; Edelbro, 2004), whose shapes and dimensions depend on the geometry of the existing discontinuities network.

2.2 Sampling strategies for discontinuities on rock masses

ISRM (1978) suggested different sampling strategies for quantitative description of discontinuities in rock masses: linear and areal sampling. Linear sampling (**Figure 3a)** measures each discontinuity that is intersected by a scan line drawn arbitrarily on the surface of the rock mass, systematically characterizing the fractures and measuring their attributes (ISRM, 1978; Priest, 1993; Watkins et al., 2015). Areal sampling describe all discontinuities within an area that is usually square or circular (**Figure 3b**).

Both methodologies result applicable in different context and their use is widely diffuse, but are affected by some systematic errors (**Figure 4**) that can influence the quality of the measurements, in particular:

Orientation bias: major probability of intersecting discontinuity traces perpendicular to direction of sampling (line, plane), and a probability of intersecting parallel discontinuities close to zero.

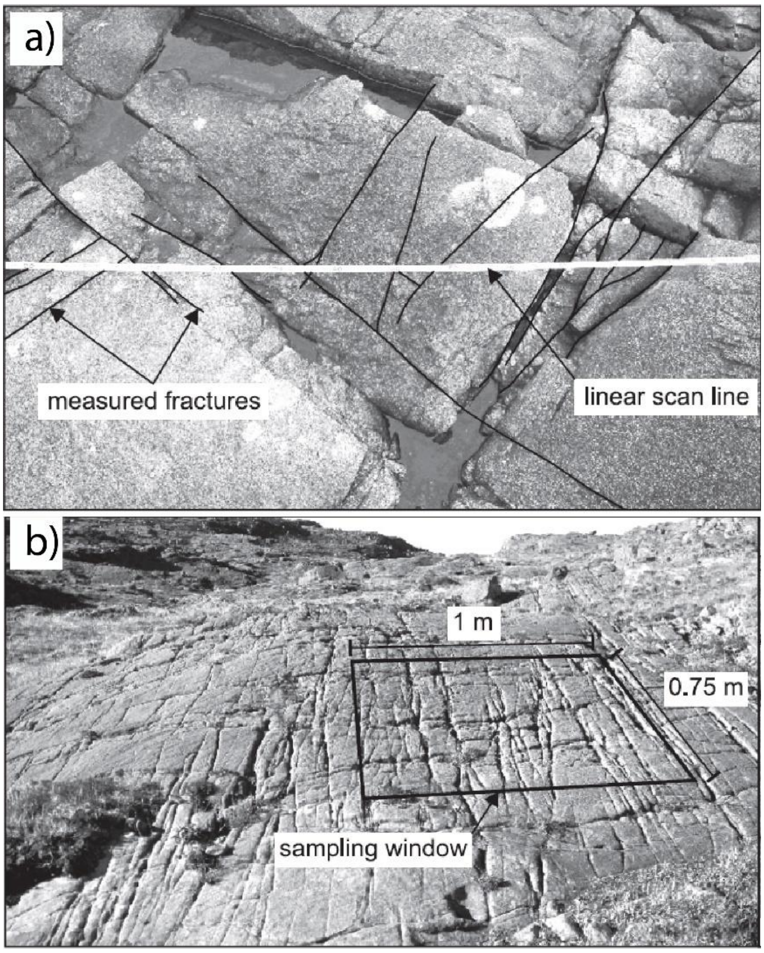

Figure 3 *Example of linear (a) and areal (b) sampling on fractured rock masses(modified after (after Watkins et al., 2015) .*

Length bias: the detection or measurement of smaller fractures is more challenging compared to larger fractures. If smaller fractures are systematically missed or underestimated, it can introduce a bias in the estimation of discontinuities populations.

Censoring bias: it refers to the incomplete observation or recording of fracture trace lengths. It can occur when fractures are truncated or terminated before reaching the boundary of the rock exposure or measurement area. Truncation can lead to underestimation or truncation of longer trace lengths, affecting the accuracy of the overall distribution.

Truncation bias: the practice of excluding or discarding fracture trace lengths that fall below a certain threshold or are considered insignificant. This can be subjective and introduce bias in the estimation of trace length distribution, particularly if the decision on what constitutes a significant length is arbitrary or inconsistent.

Linear sampling allows a quantitative characterization of all discontinuities intersecting the scanline but can be strongly influenced by orientation and size bias due to the dimension of sampling. Areal sampling allows a prior classification of discontinuities into sets and should reduce systematic errors, but it is complex to characterize systematically all discontinuities in the chosen area and the resultant characterization can be more qualitative.

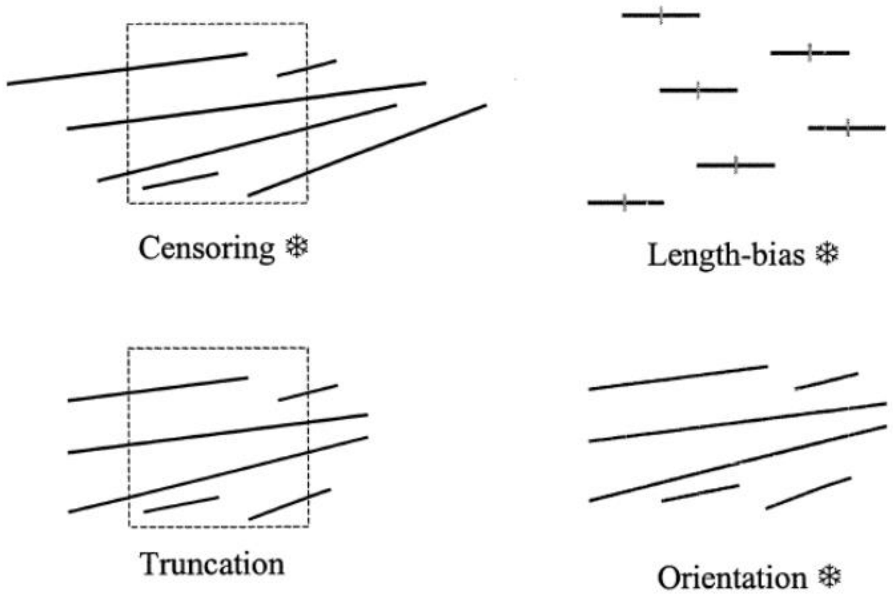

Figure 4 *Main systematic errors in discontinuities sampling strategies.*

2.3 Fracturing state: abundance metrics

Quantitative rock fracturing descriptors vary according to the sampling dimension used (count-1D, linear areal-2D or volumetric-3D) and the topology of the fractures (points, lines, areas, volumes). The correlation between fracture size and sampling size is well-defined through the matrix proposed by Dershowitz & Herda (1992), that clearly identifies the principal metrics of fracture abundance for rocks (**Figure 5**).

In particular, if we consider fractures as points and count the number of fractures within the sampling dimension used, we obtain the fracture density. When the sampling dimension is zero, the fracture density represents the number of fractures per sampling point, or simply the number of fractures (parameter P_{00}).

By increasing the sampling dimension, we move to the number of fractures per unit length (P_{10}) representing fracture linear intensity (i.e frequency), per unit area (P_{20}) and per unit volume (P_{30}) representing the volumetric fracture density. At the same time, interpreting the fracture topologically as a line or surface, we obtain areal (P_{21}) to volumetric (P_{32}) intensity measurements and considering fractures with their aperture (i.e., volumes) fracture porosity measurements (P_{33}).

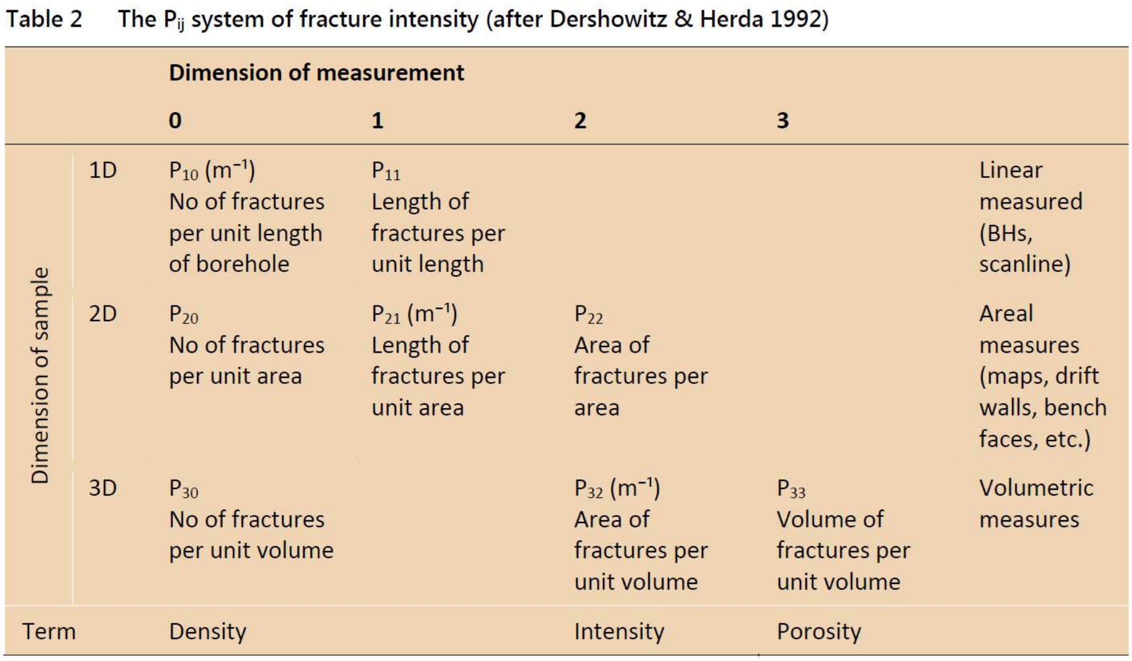

Table 2 The P_{ij} system of fracture intensity (after Dershowitz & Herda 1992)

		Dimension of measurement				
		0	1	2	3	
Dimension of sample	1D	P_{10} (m^{-1}) No of fractures per unit length of borehole	P_{11} Length of fractures per unit length			Linear measured (BHs, scanline)
	2D	P_{20} No of fractures per unit area	P_{21} (m^{-1}) Length of fractures per unit area	P_{22} Area of fractures per area		Areal measures (maps, drift walls, bench faces, etc.)
	3D	P_{30} No of fractures per unit volume		P_{32} (m^{-1}) Area of fractures per unit volume	P_{33} Volume of fractures per unit volume	Volumetric measures
Term		Density		Intensity	Porosity	

Figure 5 *Matrix of principals fracture abundance metrics* (Rogers et al., 2017)

A complete representation of the fracturing state in a 3D framework, expressed in terms of volumetric fracture intensity (P_{32}) and fracture porosity (P_{33}), can be obtained using non-destructive imaging techniques such as X-Ray Computed Tomography (Keller, 1998; Montemagno & Pyrak-Nolte, 1999; Agliardi et al., 2014; 2017). These high-resolution techniques are very powerful for laboratory-scale studies, while are unsuitable *in situ*, where geophysical techniques are usually applied (e.g. seismic methods, Ground Penetrating Radar; Grasmueck, 1996; Bakulin et al., 2000). However, geophysical imaging is often unable to support a reliable reconstruction of fracture networks due to lack of sufficient spatial resolution and related difficulties in identifying small fractures, that form most of fracture networks and act as key players of fracture connectivity, rock mass permeability and strength.

For this reason, areal or linear (scanline) field sampling strategies (ISRM, 1978) are mainly used *in situ*, yielding fracture abundance descriptors affected by size and orientation biases (e.g. frequency, P_{10}, or surface fracture intensity, P_{21}; (Zhang & Einstein, 1998; Mauldon et al., 2001) or empirical indices of "geomechanical quality".

2.4 Discrete discontinuities attributes

ISRM (1978) suggested the definition of most important attributes of discontinuities (**Figure 6**); some that influence the structure of *rock mass* (n° of sets, dip direction, persistence, spacing) and typical shape and size of their blocks, some that influence *rock-mass* mechanical and hydraulic properties (roughness, wall strength, aperture).

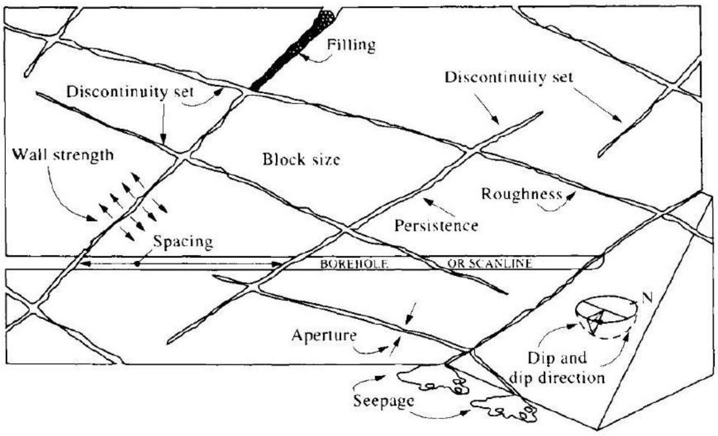

Figure 6 *Principals discontinuities attributes for rock mass survey, suggested by ISRM (1978), (Hudson & Harrison, 2000).*

Dip and Dip direction

Discontinuities planes can be defined in space using the values of azimuth (i.e dip direction) and dip respect to fixed coordinate systems; azimuth represents the horizontal direction of the plane relative to geographic North while dip represents the angle of the plane's inclination relative to the horizontal surface (**Figure 7**, Lisle & Leyshon, 2004).

Generally, the geometric representation of a discontinuity is provided on a stereographic projection (Lisle & Leyshon, 2004), which makes it possible to highlight each plane and analyse populations of discontinuity measurements on natural outcrops, defining their sets numbers and relative orientations within the rock mass. Statistical analysis is required to determine the sets, which is based on a density analysis of the planes' poles (Shanley & Mahtab, 1974; Fisher et al., 1993) so advanced statistical analysis algorithms have been developed over time (Hudson & Priest, 1983; Miller, 1983; Welch, n.d.).

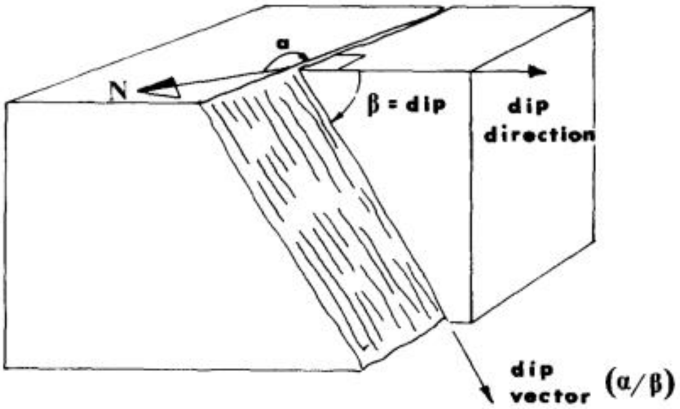

Figure 7 *Representation of vector Dip and Dip Direction respect to Geographic North* (Barton et al., 1974)

Spacing and Frequency

Total discontinuity spacing refers to the distance between two adjacent discontinuities along one direction. Priest & Hudson (1981) specifies that this parameter refers to set spacing if the measurement is made along discontinuities belonging to the same set (**Figure 6**), and normal set spacing if it is calculated along a scan line perpendicular to the mean orientation of the set (Terzaghi, 1965).

Frequency is defined as the number of discontinuities per unit length; mathematically, it is calculated as the reciprocal of the spacing. Frequency follows a negative exponential law, where smaller fractures have a higher frequency within a cluster of discontinuities, while larger fractures have a progressively lower frequency (Priest & Hudson, 1976) the most common distribution used in the literature for fractured materials is the lognormal and the negative exponential (**Figure 8**, Priest & Hudson, 1976; Rives et al., 1992):

$$f(x) = \lambda \exp(-\lambda x)$$

Equation 1

Where $f(x)$ is the discontinuities frequency (m^{-1}).

λ is the mean spacing of set (m).

x is the spacing class (m).

The evaluation of the number of sets, their orientation in space, and their spacing allows defining the shape of the rock block and the various scenarios of possible volume of blocks in rock masses.

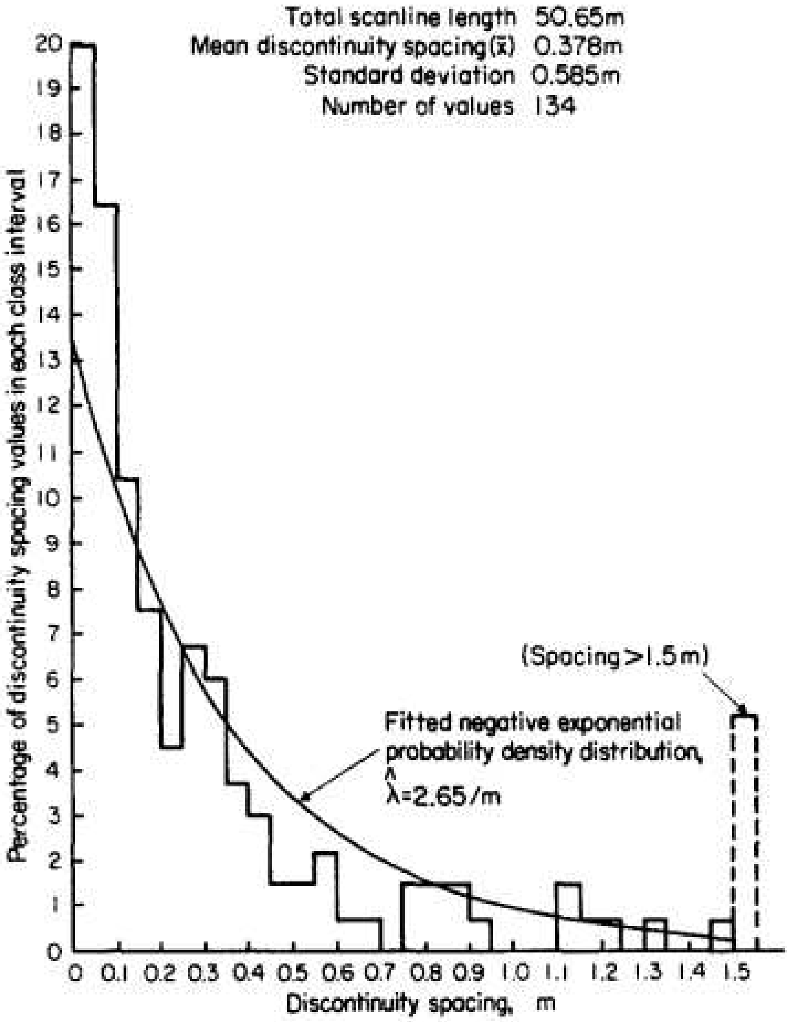

Figure 8 *Histogram shows spacing dataset measured on the field, fitted with the negative exponential law (Priest & Hudson, 1976)*

Fracture size: trace length and Persistence

The trace lengths of discontinuities are fundamental to estimate the discontinuity in common sampling strategies (ISRM, 1978). For limited extent outcrops it is common practice to measure the lengths of discontinuities located above or below the scanline, referred to as semi-trace lengths. Whether dealing with trace lengths or semi-trace lengths, several authors illustrated sources of errors in their estimation (Zhang & Einstein, 1998;

Mauldon et al., 2001). Hence, fracture length is one of the most challenging parameters to quantitatively estimate realistically (Laslett, 1982).

It is important to be aware of these errors and their potential impacts when characterizing fracture trace lengths in rock masses and proper methodologies and techniques should be applied to minimize these biases and ensure accurate and representative results, that strongly influence the estimation of areal fracture intensity in the selected window (P_{21}).

Persistence is the percentage ratio of the area occupied by the discontinuity to the area of the plane containing it, providing an estimate of the percentage of intact rock bridges that contribute to the stability of rock mass. Due to sampling difficulties, it is common practice to approximate the persistence of discontinuities based on their modal lengths (ISRM, 1978).

Roughness

This parameter, known as roughness (Barton, 1973), quantifies the geometric irregularities of a discontinuity and is typically measured as the deviation from the modal plane. It encompasses both small-scale roughness (on the order of centimetres) and large-scale roughness (on the order of decimetres to meters), the latter often referred to as waviness. The roughness of a discontinuity influences its mechanical behavior at both laboratory and field scales (**Figure 9**).

Small-scale roughness primarily impacts the resistance and shear strength of rock samples in laboratory testing. It introduces micro-asperities and contact irregularities, which affect the frictional characteristics and shear resistance along the discontinuity surface. The rougher the surface, the higher the resistance to shear displacement.

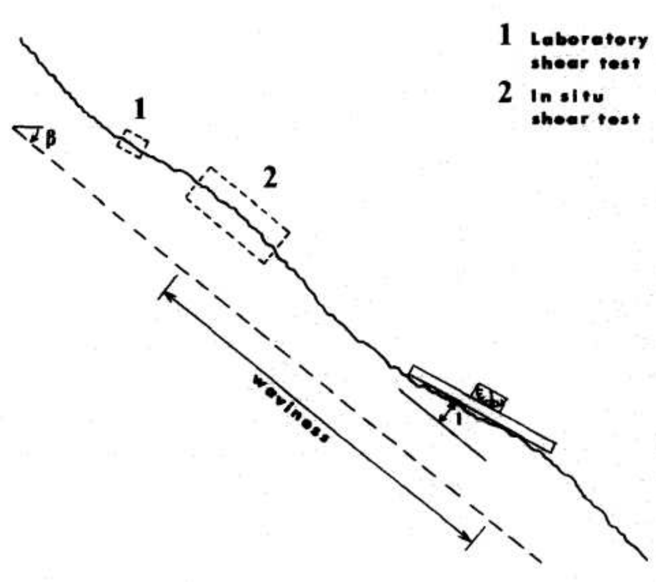

Figure 9 *Roughness of discontinuities play role at different scale from cm to m in function of the observation scale (ISRM, 1978)*

On the other hand, large-scale roughness, or waviness, has implications for the overall stability and behavior of rock masses at a larger scale. It affects the interaction between adjacent rock blocks and the overall structural integrity. Waviness can lead to stress concentrations, localized deformation, and potential failure mechanisms such as wedging or block sliding.

Barton (1973) introduced a classification of in situ roughness using the Joint Roughness Coefficient (JRC, Barton, 1973), which allows the roughness class of a discontinuity to be classified at the outcrop scale (cm) through the use of 10 standard profiles (**Figure 10**).

This parameter results can be used in empirical relationships to obtain the friction angle of discontinuities surfaces (Barton, 1973, see after).

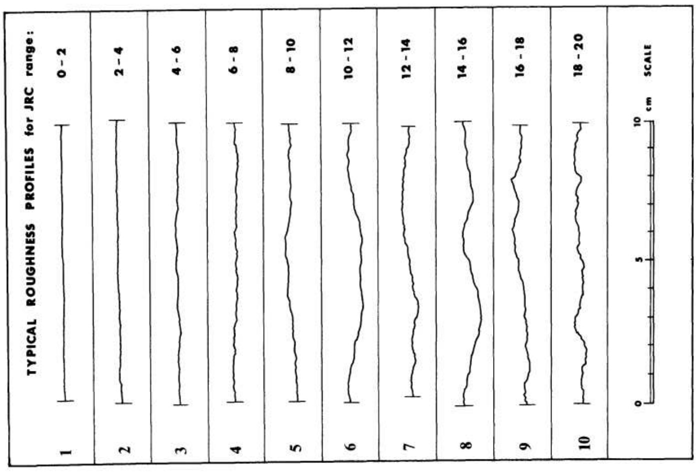

Figure 10 *Roughness standard profiles suggested by* (ISRM, 1978) *for practical JRC estimation.*

Furthermore, roughness has implications beyond mechanical behavior. It also influences the opening and hydraulic characteristics of discontinuities. Rough surfaces create localized flow paths and variations in flow velocity, affecting the permeability and fluid flow through the discontinuity network. This, in turn, can have consequences for groundwater flow, slope stability, and engineering design.

Surface Weathering

The degree of surface alteration of a discontinuity is important in determining its strength, since the presence of a surface film of alteration (or more pervasive), results in a loss of strength by the material itself. Estimation of the alteration of a discontinuity can be done qualitatively through various classification tables with standard descriptions (ISRM, 1978).

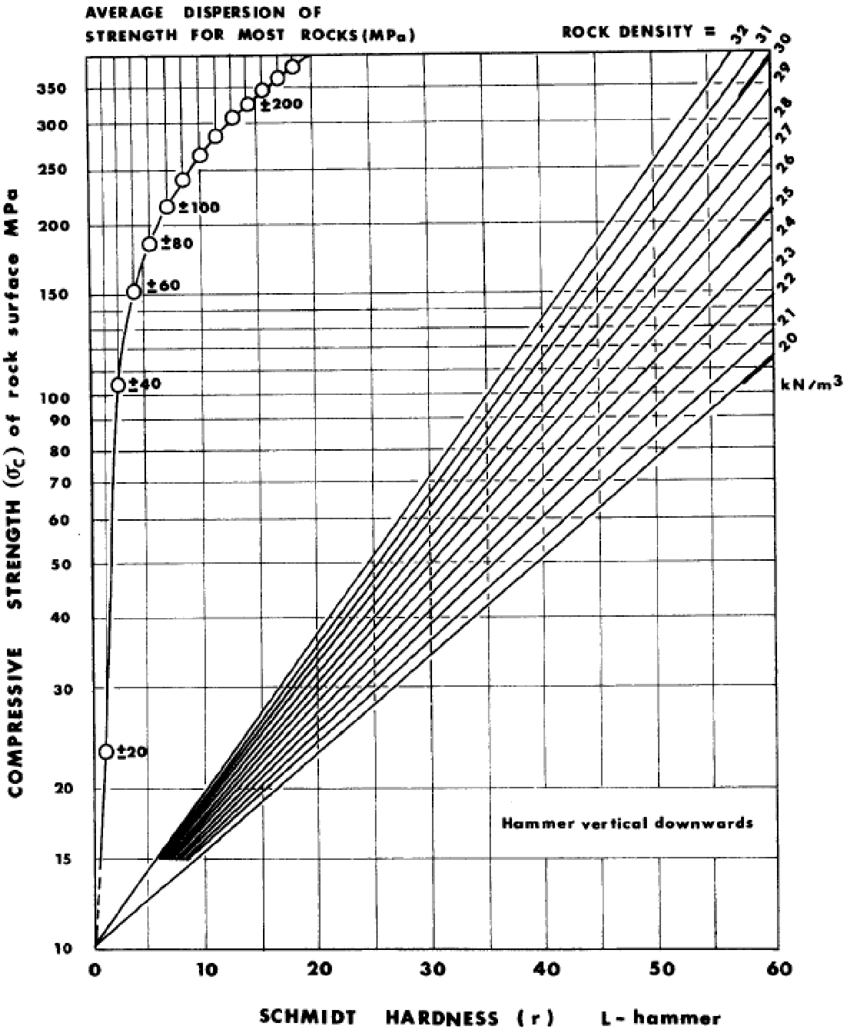

Figure 11 *Graph for JCS evaluation using estimate density for rock type and Schmidt Hammer values (Barton, 1973)*

ISRM (1978) also suggests a quantitative way by performing sclerometric tests (i.e Schmidt Hammer, Miller, 1965) on the surface itself and assuming rock density reference value for the lithology of interest, plotting values on the abacus in **Figure 11**, in order to define the strength of the altered rock surface defined as Joint Compressive Strength (JCS; Miller, 1965). The hammer consists of a cylindrical body with a spring-loaded plunger and a hammerhead at the end. The Schmidt hammer works based on the principle that the rebound of a spring-loaded mass striking the surface of a material is related to its hardness or strength. By measuring the rebound velocity, the device provides an indication of the material's compressive strength.

The JCS then turns out to be a descriptor of the mechanical properties of the discontinuity in terms of both compressive strength but also friction angle (ϕ) using the following empirical formula (Barton, 1973):

$$\phi = JRC log_{10}\left(\frac{JCS}{UCS}\right) + \phi_r$$

Equation 2

Where ϕ is the discontinuities friction angle of peak (°).

ϕ_r is the residual friction angle (°).

Aperture

The opening is the perpendicular distance between two surfaces of a discontinuity (**Figure 12**) and can varies from zero for closed discontinuities to mm, cm and up to m scale.

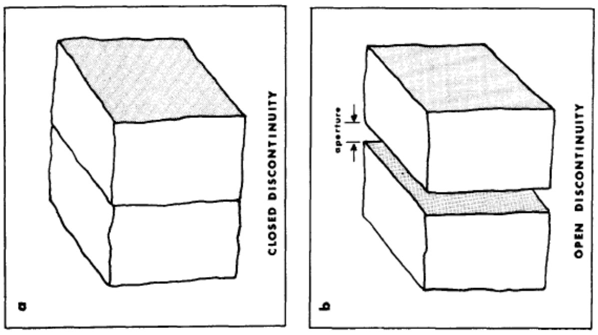

Figure 12 *Example of closed and open discontinuities* (ISRM, 1978)

Aperture mainly characterizes the hydraulic conductivity properties of the rock mass (Hoek & Bray, 1981; Sanderson & Zhang, 1999; Wang & Park, 2002; Baghbanan & Jing, 2008) and in general fluid circulation in rock masses. The opening is strongly dependent on the stress state of the fracture, which is often more open on the outcrop due to the low confinement of rock mass. Aperture of discontinuities became crucial in evaluate the fracture porosity (P_{33}), an unbiased measure of fracturing state in rocks, however it is one of the most challenging parameter to define *in situ*.

2.5 Discontinuities in Rock-masses: continuum vs discontinuum

Observing a rock mass with increasing observation scale, few discontinuities with high spacing and persistence will be included (**Figure 13**; (Hoek, 1983; Hoek & Brown, 1988;

Krauland et al., 1989; Edelbro, 2004). Observing at smaller and medium scales, the discontinuous fractured medium (**Figure 13**) can be described by intact rock properties and the discrete attributes of the discontinuities that are characterized by different spacing and persistence, degrees of roughness and alteration, which change their strength (Barton et al., 1974), as explained below. At these scales, quantitative fracturing abundance descriptors (Dershowitz & Herda, 1992) are still applicable and remain significant across increasing scales. Considering large-scale problems, rock mass is made up of several densely spaced sets of discontinuities, making the size of the blocks relatively smaller to the scale of the problem. These assumptions make it possible to relate the overall behaviour of a rock mass to that of an equivalent continuum (**Figure 13**, **Figure 14**), changing the significance of fracture abundance metrics and including the introduction of more empirical descriptors of fracturing state (e.g rock-mass quality classifications) that can be useful to describe fracturing state in an homogeneous way.

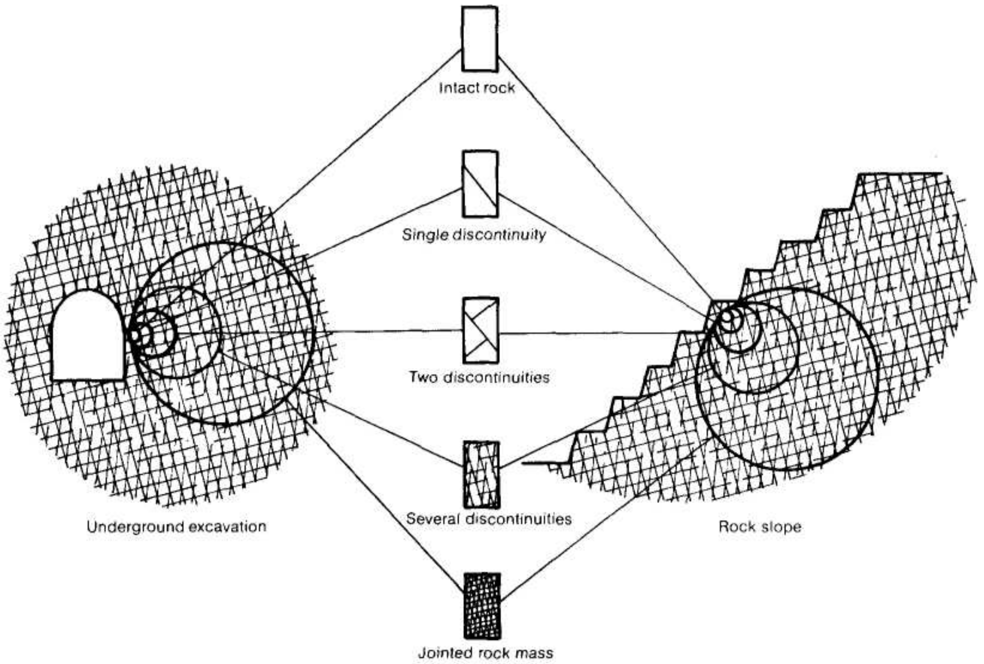

Figure 13 *Different scale of rock-mass observation for engineering applications; at medium scale of observation, rock-mass represents a discontinuous medium (Hoek, 1983)*

It is thus clear that discontinuous, non-homogeneous, often anisotropic medium (Hoek & Diederichs, 2006) physical characteristics of rock mass and hydraulic and geomechanical behavior are strongly dependent on the spatial scale considered, and challenging to be realistically evaluated (**Figure 13**). The hydro-geomechanical behavior of rock mass at smaller scales therefore depends on the interaction between the properties of the intact rock, such as strength and deformability, and the properties of the discrete discontinuities (Hoek & Brown, 1980; Hoek & Diederichs, 2006).

At larger scales rock-mass became a medium whose strength, deformability, and hydraulic properties can be traced back to those of an equivalent continuum medium (**Figure 13,;** (Hoek & Brown, 1980; Krauland et al., 1989).

2.5.1 Fracturing and hydro-geomechanical properties

As observed by Hoek & Brown (1980) on uniaxial compression tests, holding the length-to-diameter ratio of cylindrical rock samples constant, but increasing the size, what is observed is a decrease in compressive strength (Hoek & Brown, 1980).

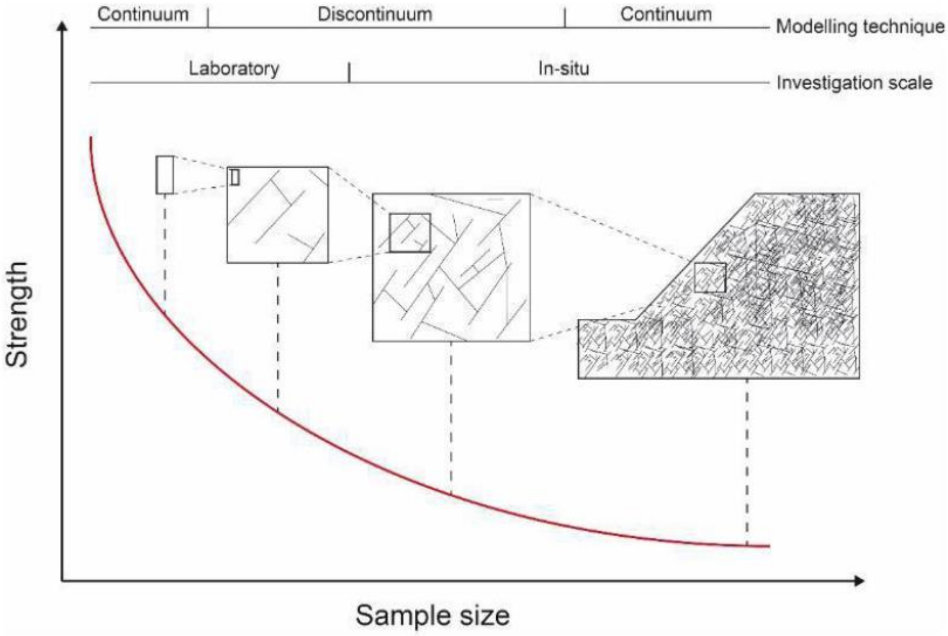

Figure 14 *Rock-mass physical behavior depends on investigation scale, as his mechanical properties influenced by the presence of discontinuities (Krauland et al., 1989)*

This scale-effect **Figure 14**; can be explained by the fact that a larger sample has a different statistical distribution of fractures, exhibiting a greater number of defects, i.e., a larger number of larger fracture sizes that significantly affect both the compressive strength and the post-peak behavior of the sample (Hoek & Brown, 1988; Krauland et al., 1989; Hudson & Harrison, 2000; Hoek & Diederichs, 2006) and clarify the play-role of discontinuities in scaling rock-masses geomechanical properties respect to the one of the intact rock (**Figure 14**).

The state of fracturing is also extremely important in the study of rock mass permeability because they both affect the geometry and connectivity of the pathways through which fluid can move, thus determining the permeability of the rock mass.

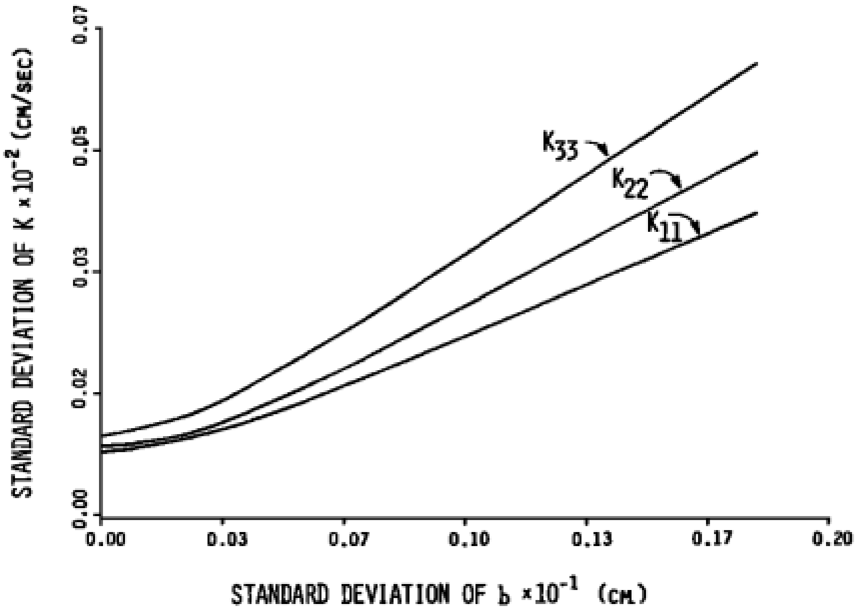

Figure 15 *Relationship between fracture opening b and permeability (Sagar & Runchal, 1982)*

Therefore, the presence and distribution of fractures may affect local permeability, allowing rapid flow through the fractures themselves, while flow through the rock matrix may be restricted. The aperture and length of a fracture influences the permeability of the rock mass at the local scale (**Figure 15**; Sagar & Runchal, 1982; Sanderson & Zhang, 1999), while the characteristic of the discontinuity sets of the fracture network influences the equivalent permeability (De Dreuzy et al., 2012; Min et al., 2004) at the scale of Representative Elementary Volume (REV) of the rock mass.

Orientation (Fisher et al., 1993), size (Mauldon et al., 2001) and fracture abundance descriptors (i.e., fracture density, Dershowitz & Herda, 1992) turn out to be key input parameters in the generation of Discrete Fracture Network models (DFN; Dershowitz, 1998; Jing & Stephansson, 2007). In a DFN model (**Figure 16**), the fractured media is represented as a network of discrete fractures, generated stochastically from input parameters (geometry, orientation, intensity etc..). Parameters are typically obtained through field observations, data analysis, or geological characterization techniques of discontinuities sets and fracturing state. DFN models are widely used for rock mass permeability studies in various fields of several practical application, such as geotechnical engineering, groundwater resource exploration, natural gas storage, and oil and gas extraction.

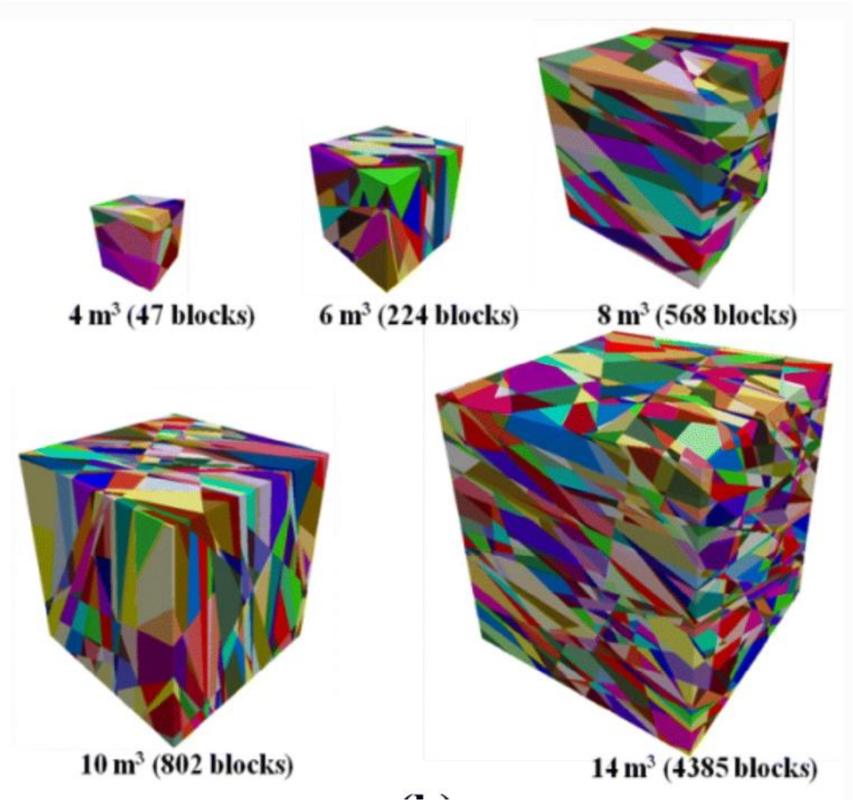

Figure 16 *Examples of DFN models for different rock-masses volumes (Wang & Cai, 2020)*

2.6 Quantitative descriptors of fracturing state

Fracturing abundance metrics defined by Dershowitz & Herda (1992) has been interpreted by several authors, and different quantitative descriptors have been defined in literature, obtained through parameters and methodologies applicable at different scales.

However, in situ estimation of unbiased fracture abundance measures (e.g., volumetric fracture intensity, P_{32}) requires geophysical imaging that usually lacks the required spatial resolution. Therefore, descriptors related to the biased fracture metrics are usually employed, which are affected by scale and orientation (Terzaghi, 1965; Priest & Hudson,

1981) and difficult to estimate when dealing with poor-quality, damaged or heterogeneous rock masses. For these reasons, most practical studies leverage on the empirical description of rock mass quality provided by empirical rating schemes as rock mass quality classification.

2.6.1 *Fracture density (P_{10}, P_{20} and P_{30})*

Regarding measurements of the orientations along a scanline, several authors pointed out the role of orientation bias in estimating discontinuities spacing and frequency.

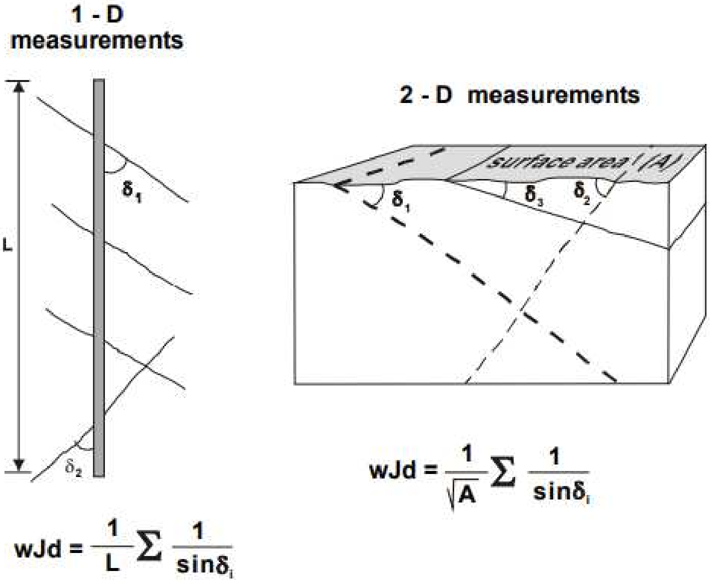

Figure 17 *Application of Wjd for P10 and P20 measures* (Palmström, 1996)

Terzaghi (1965) proposed a method for weight spacing measures for discontinuities that are not perpendicular to the scanline, introducing a weight factor (w; Terzaghi, 1965), calculated as the cosine of the angle of interception.

Based on this idea, Palmström (1996) proposed a method to estimate P_{10} and P_{20} , the Weighted Joint density (WJd; Palmström, 1996) as a fracture frequency index based on Terzaghi correction.

Palmström (1982) also suggest a parameter to estimate P_{30}, the Volumetric Joint Count (Jv; Palmstrom, 1982) as the number of discontinuities in 1m^3 of rock volume, related with block volumes (VRU, **Figure 18**, Palmstrom, 2005).

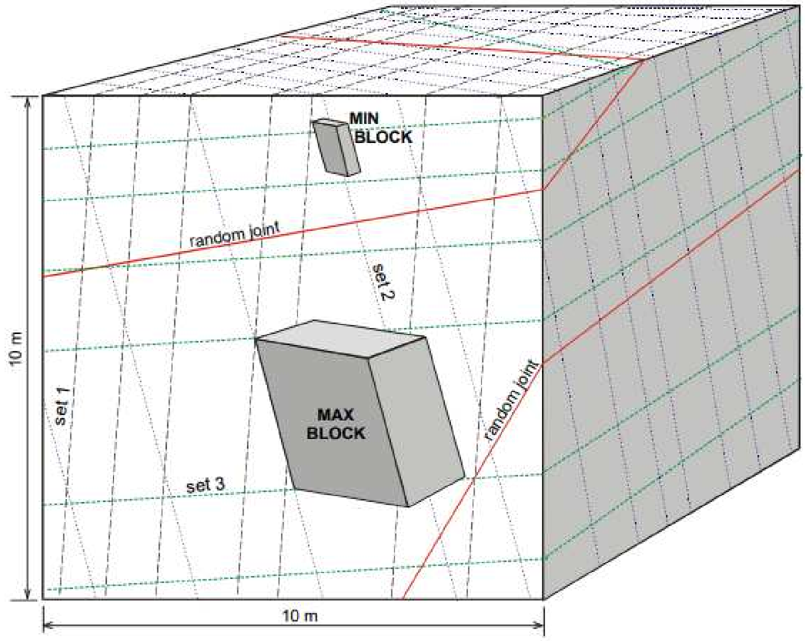

Figure 18 *Different block volumes isolated by 3 discontinuity sets in a rock-mass (Palmstrom, 2005)*

2.6.2 Linear fracture intensity (P_{21})

As anticipated earlier, the estimation of the correct trace lengths of discontinuities appears to be affected by length and censoring biases that compromise a quantitative realistic estimation of linear fracture intensity (P_{21}; Dershowitz & Herda, 1992; Rogers et al., 2017). However, trace length turns out to be a key parameter in the estimation of P_{21} in natural outcrops, especially those of limited size. Some authors suggest methodologies based on the use of a circular window for estimating the average trace length that is representative and less affected by systematic errors.

Zhang & Einstein (1998) suggest a methodology based on counting discontinuities within a circular window according to the following classification (**Figure 19**):

- N0: both discontinuities terminations are outside the sampling window.
- N1: one discontinuities termination is visible inside the sampling window.
- N2: both discontinuities terminations are inside the sampling window.

Based on this assumption for planar and uniform distributed mean point of traces, mean trace length (μ, Zhang & Einstein, 1998) can be calculated as:

$$\mu = \frac{\pi(N + N0 - N2)}{2(N - No + N2)} c$$

Equation 3

Where μ is the mean trace length

N is the discontinuities number (-).

c is the radius of the circular windows (m).

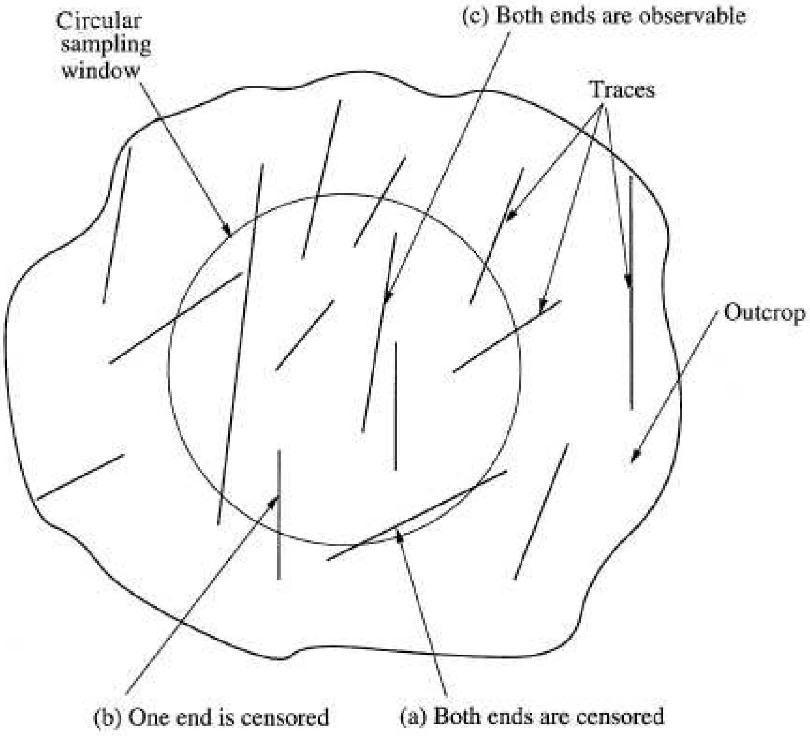

Figure 19 *Example of fracture type classification for estimation of mean trace length in natural outcrops for* (Zhang & Einstein, 1998).

Mauldon et al. (2001) proposed a similar approach counting the number of terminations inside the circular scanline (*m*) and the number of the intersection between discontinuities traces and the scanline (n) (**Figure 20**).

So mean trace length (μ, Mauldon et al., 2001) and P_{21} can be calculated as:

$$\mu = \frac{\pi r}{2} \frac{n}{m} ; P_{21} = \frac{n}{4r}$$

Equation 4

Where μ is the mean trace length

r is the radius of the circular windows (m).

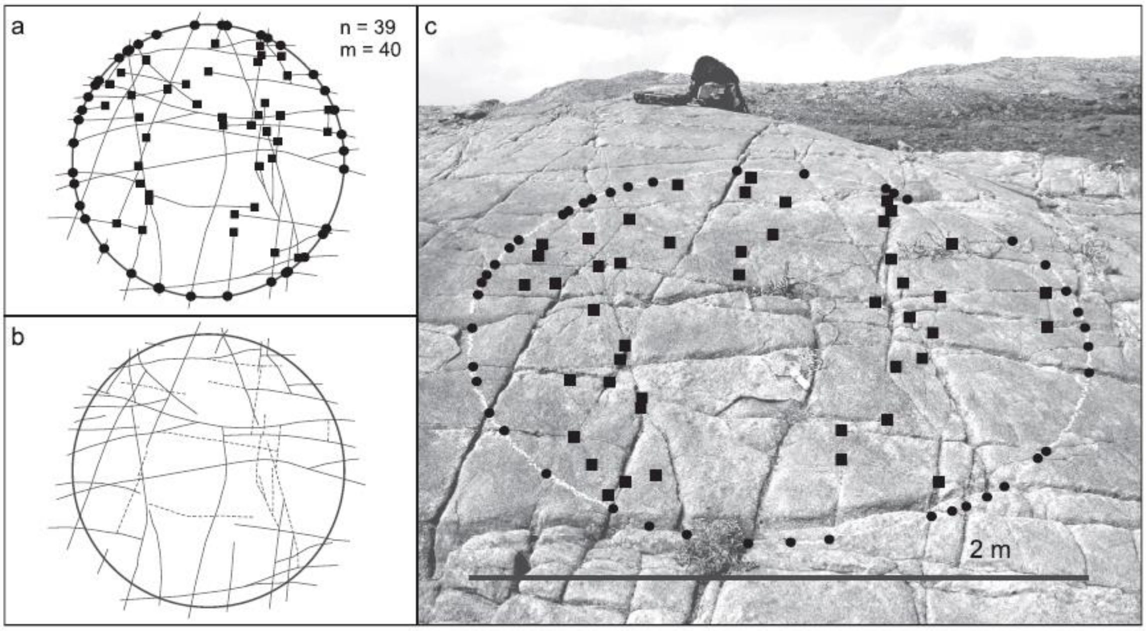

Figure 20 *Fracture termination count for mean trace length estimation for Mauldon et al. (2001) method (Watkins et al., 2015).*

These methods show how to measure in the field P_{10} and P_{21}, but they cannot be used as general parameters to characterize fracture intensity because of their directional dependence. For these reasons linear density or areal intensity are generally linearly correlated with P_{32} (Wang, 2005; Ren et al., 2017) using semi-analytical conversion factors widely used as input variables in DFN (Dershowitz, 1998; Harthong et al., 2012; Wang & Cai, 2020) for rock masses.

2.6.3 Rock-mass quality classifications

Rock Quality Designation (RQD)

Introduced by Deere (1967), RQD is a rock mass quality index that is based on the concept of linear frequency of discontinuities, so it can be used in scanlines on outcrop or to describe rock cores.

RQD expresses the percentage amount of intact rock sectors along the sampling direction that exceeds 10 cm, so it ranges from 0 to 100 as:

$$RQD = \frac{\sum length\ of\ intact\ rock\ line/core\ pieces > 0.1}{Total\ scanline/core\ length}$$

Equation 5

Some authors suggest empirical correlations between the value of RQD and the average frequency of discontinuities (λ, Priest & Hudson, 1976) or with the Jv (Palmstrom, 1982). RQD is intrinsically very related to directionality of sampling (e.g., cores) and is not a good descriptor of high-quality rock masses (RQD equals 100 above 10 cm spacing, **Figure 21**) but is widely used in other multi-parametric quality classifications.

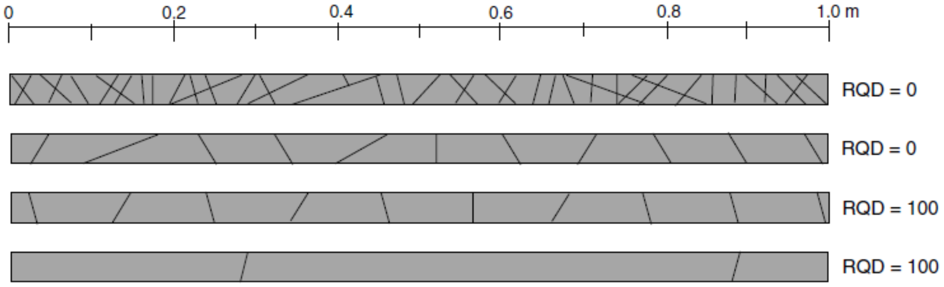

Figure 21 *Examples of RQD values for rock cores (*(Palmstrom, 2005)*)*

Rock Mass Rating (RMR)

Introduced by Bieniawski (1993), RMR is a multi-parametric rock mass quality classification scheme consisting of a simple sum of scores that depend on;

- A1: UCS of intact rock.
- A2: RQD.
- A3: Discontinuities spacing.
- A4: Discontinuities conditions.
- A5: Water presence.
- B: discontinuities orientation.

So, RMR can be calculated as:

$$RMR = A1 + A2 + A3 + A4 + A5 + \mathrm{B}$$

Equation 6

It is important that RMR is calculated for homogeneous structural domains separately within the area to be characterized, and it is better to use intermediate scores than the discrete scores indicated by the table (**Figure 22**).

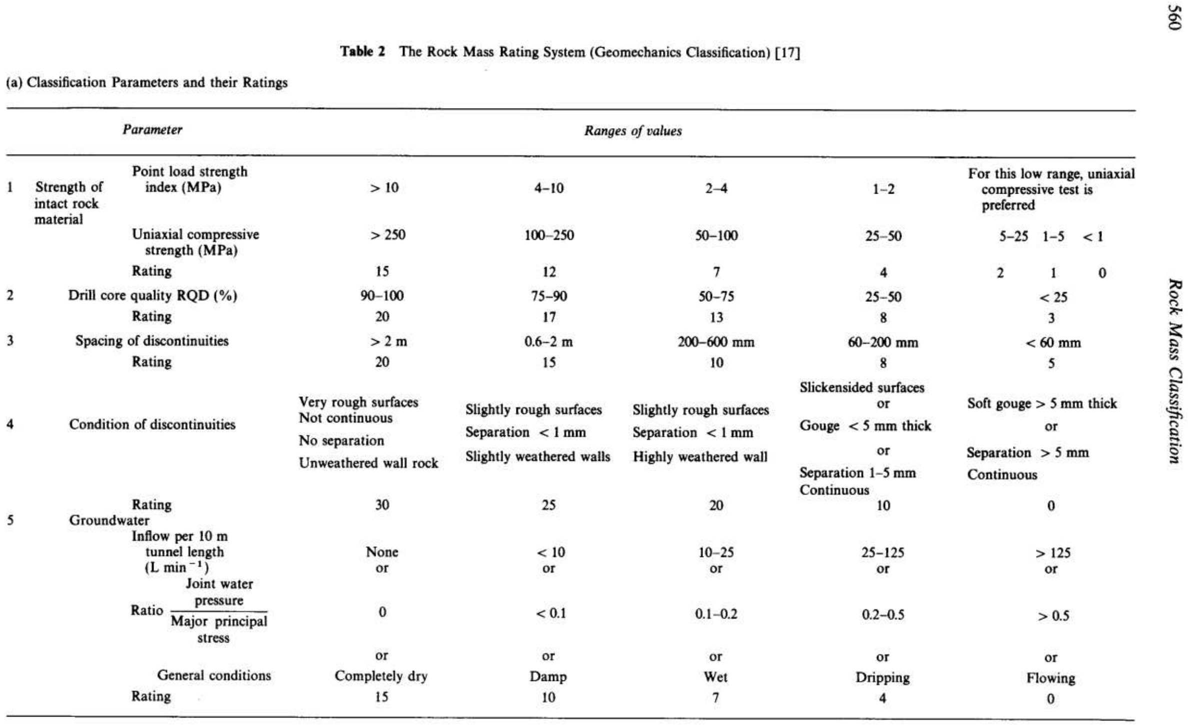

Table 2 The Rock Mass Rating System (Geomechanics Classification) [17]

(a) Classification Parameters and their Ratings

	Parameter		*Ranges of values*				
1	Strength of intact rock material	Point load strength index (MPa)	> 10	4–10	2–4	1–2	For this low range, uniaxial compressive test is preferred
		Uniaxial compressive strength (MPa)	> 250	100–250	50–100	25–50	5–25 1–5 < 1
		Rating	15	12	7	4	2 1 0
2	Drill core quality RQD (%)		90–100	75–90	50–75	25–50	< 25
		Rating	20	17	13	8	3
3	Spacing of discontinuities		> 2 m	0.6–2 m	200–600 mm	60–200 mm	< 60 mm
		Rating	20	15	10	8	5
4	Condition of discontinuities		Very rough surfaces Not continuous No separation Unweathered wall rock	Slightly rough surfaces Separation < 1 mm Slightly weathered walls	Slightly rough surfaces Separation < 1 mm Highly weathered wall	Slickensided surfaces or Gouge < 5 mm thick or Separation 1–5 mm Continuous	Soft gouge > 5 mm thick or Separation > 5 mm Continuous
		Rating	30	25	20	10	0
5	Groundwater						
		Inflow per 10 m tunnel length (L min^{-1})	None or	< 10 or	10–25 or	25–125 or	> 125 or
		Ratio $\frac{\text{Joint water pressure}}{\text{Major principal stress}}$	0 or	< 0.1 or	0.1–0.2 or	0.2–0.5 or	> 0.5 or
		General conditions	Completely dry	Damp	Wet	Dripping	Flowing
		Rating	15	10	7	4	0

Figure 22 *Score table for RMR classification* (Bieniawski, 1993).

<u>Rock tunnelling Quality System (Q-System)</u>

The multi-parametric Q-system was presented by Barton et al. (1974) for tunnel and underground excavations and successively extended to other applications in natural rock masses. The rock mass quality is estimated by means of the Q index, which takes into account the discontinuity properties (**Figure 23**):

$$Q = \frac{RQD}{Jn} + \frac{Jr}{Ja} + \frac{SRF}{Jw}$$

Equation 7

where Jn is the number of joint sets

Jr is the joint roughness parameter

Ja is the joint alteration parameter

Jw is the joint water parameter

SRF is the Stress Reduction Factor

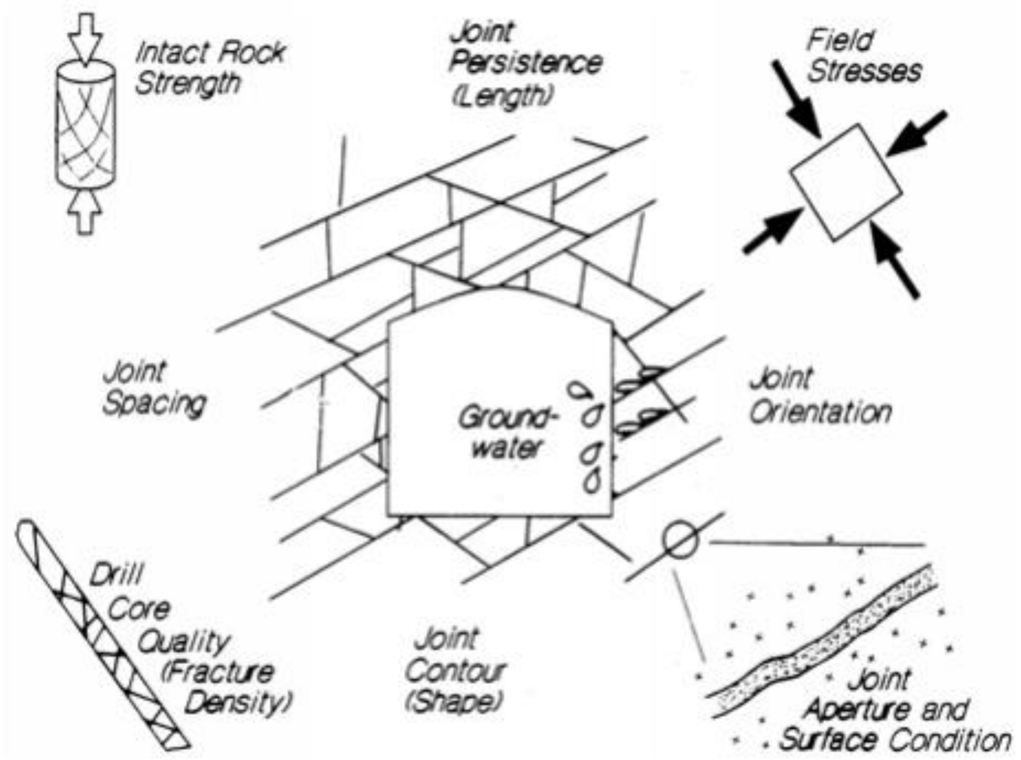

Figure 23 *Conceptual scheme of key-players in Q classification rate for rock-masses (Barton et al., 1974)*

Barton et al. (1974) discusses three ratios, respectively describing different geological aspects:

- RQD/Jn is descriptive of rock mass structure and block size.
- Jr/Ja describes the shear strength tendency of the blocks.
- SRF/Jw, on the other hand, is related to the stress state of the rock mass.

Is important to highlight that in this classification, the role of discontinuity orientation is not considered.

Geological Strength Index (GSI)

The GSI was introduced by Hoek et al. (1995), as a classification to support the Hoek-Brown original criterium for rock-mass strength.

The original GSI proposed by Hoek et al. (1995), proposed a classification in which the index varies between 5 and 95, based on two main geological observations:

- the structure of the rock-mass in terms of block interlocking and degree of disturbance by the fracture network
- the degree of weathering of discontinuities surfaces

Based on these observations, using the scheme in **Figure 24** is it possible to classify the rock-mass in a specific GSI interval, representative of this quality.

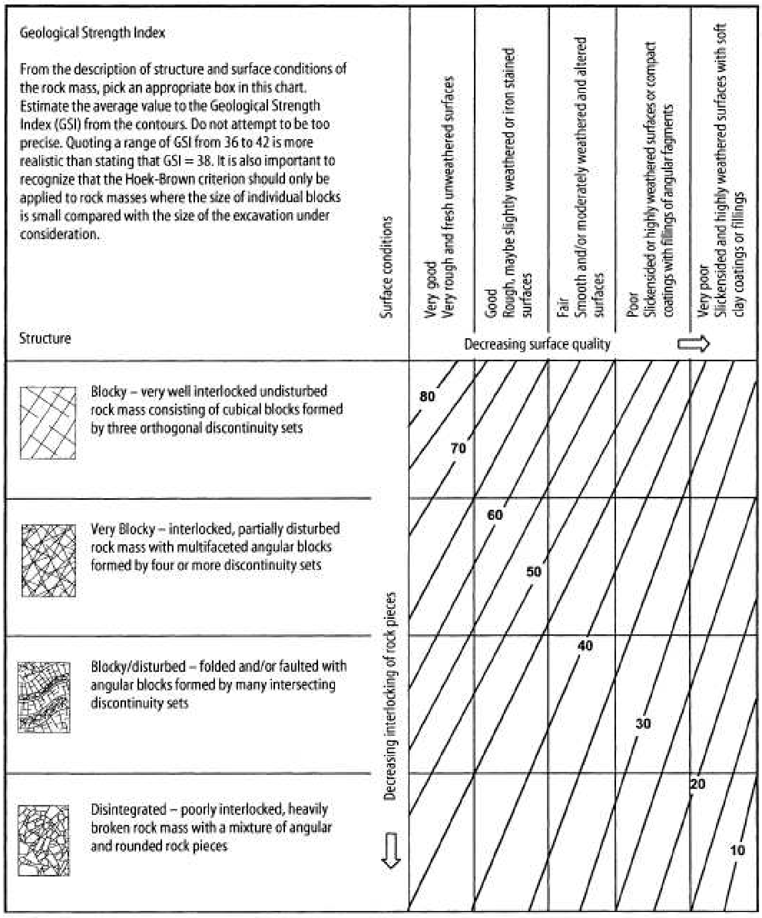
Geological Strength Index

From the description of structure and surface conditions of the rock mass, pick an appropriate box in this chart. Estimate the average value to the Geological Strength Index (GSI) from the contours. Do not attempt to be too precise. Quoting a range of GSI from 36 to 42 is more realistic than stating that GSI = 38. It is also important to recognize that the Hoek-Brown criterion should only be applied to rock masses where the size of individual blocks is small compared with the size of the excavation under consideration.

Figure 24 *GSI classification by (Hoek & Brown, 1997)*

This classification is very simple and broadly applicable in a wide range of geological context, but at the same it isn't a multi-parametric classification so needs caution and a detailed and experienced geomechanical survey to be used and validated.

Many authors suggested advanced version of these classification, update the scheme for larger number of geologic situations (Marinos & Hoek, 2000), or focusing the classification on more quantitatively approach such as the block size and the Joint Condition factor (Cai et al. 2004), or modifying it for classification of rock-mass cores (Borehole GSI, Agliardi et al., 2016).

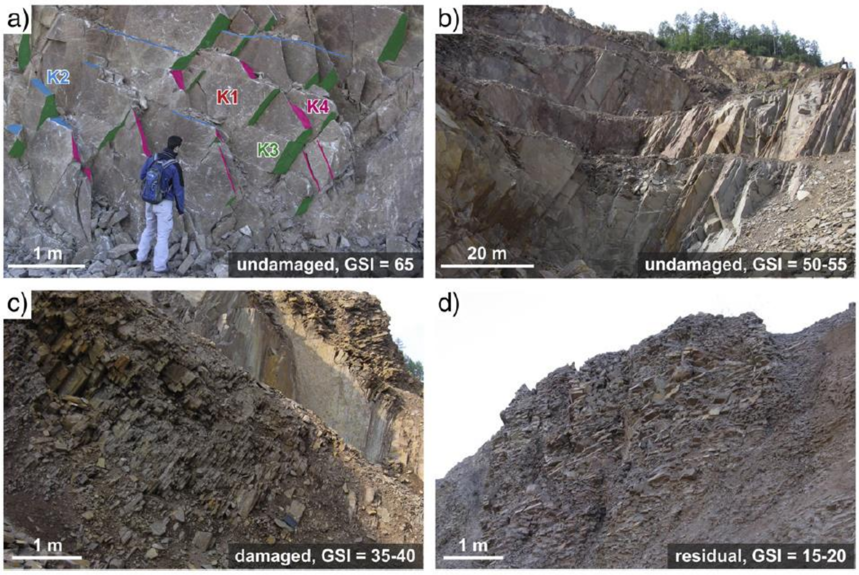

Figure 25 *Examples of GSI estimation on rock-mass outcrop (Agliardi et al., 2013).*

The original GSI classification (**Figure 24**) assumes visual inspection of outcrops and on the type of rock mass structure suggested by its appearance, providing a value with a strong qualitative component and more easily influenced by the subjectivity and degree of experience of the operator.

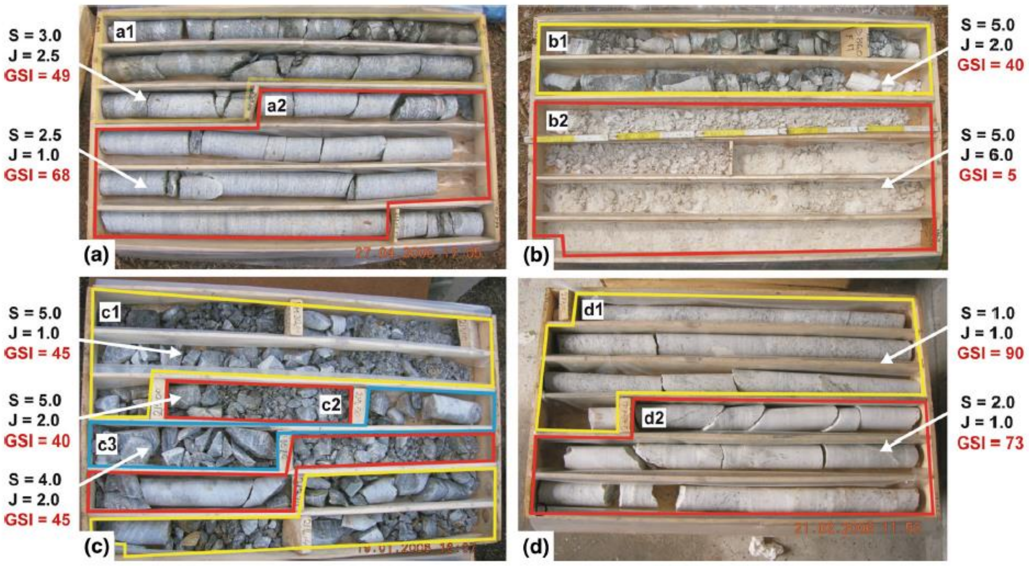

Figure 26 *Evaluation of GSI values on borehole core-logging (Agliardi et al., 2016).*

Marinos & Hoek (2000) propose an expanded table to a greater variety of geologic situations, with particular reference to the lithology characterizing the outcrop and specific applications in extremely weak or complex rock masses (**Figure 27**).

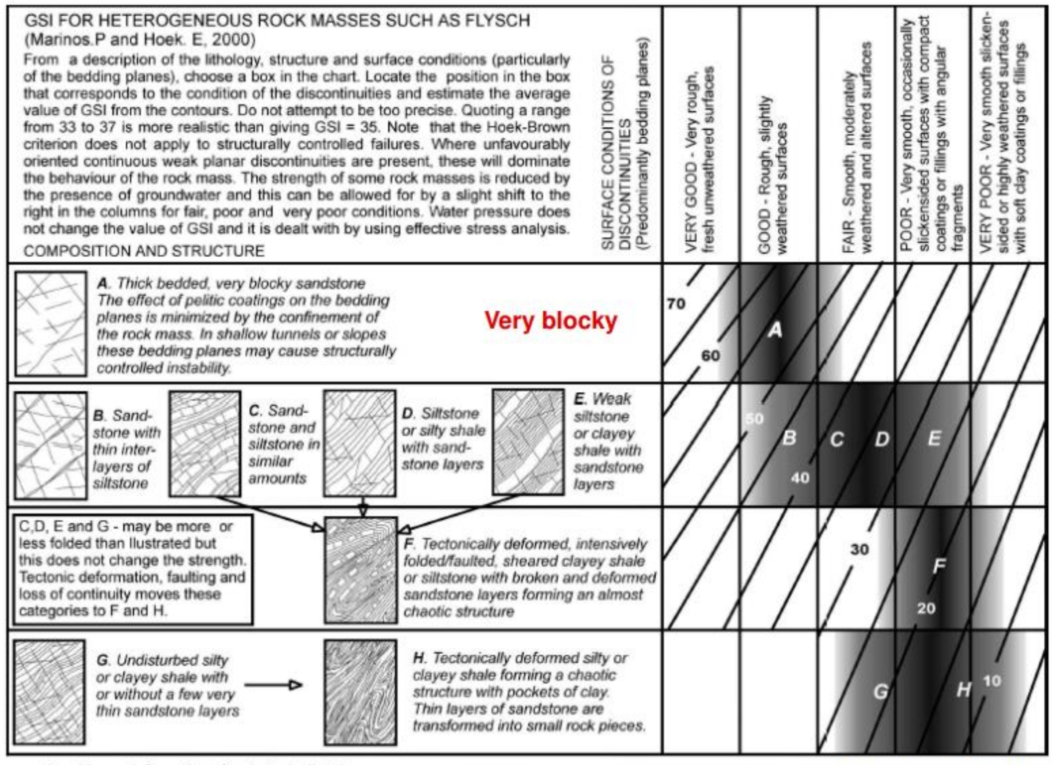

GSI FOR HETEROGENEOUS ROCK MASSES SUCH AS FLYSCH
(Marinos.P and Hoek. E, 2000)

From a description of the lithology, structure and surface conditions (particularly of the bedding planes), choose a box in the chart. Locate the position in the box that corresponds to the condition of the discontinuities and estimate the average value of GSI from the contours. Do not attempt to be too precise. Quoting a range from 33 to 37 is more realistic than giving GSI = 35. Note that the Hoek-Brown criterion does not apply to structurally controlled failures. Where unfavourably oriented continuous weak planar discontinuities are present, these will dominate the behaviour of the rock mass. The strength of some rock masses is reduced by the presence of groundwater and this can be allowed for by a slight shift to the right in the columns for fair, poor and very poor conditions. Water pressure does not change the value of GSI and it is dealt with by using effective stress analysis.

COMPOSITION AND STRUCTURE

SURFACE CONDITIONS OF DISCONTINUITIES (Predominantly bedding planes)

VERY GOOD - Very rough, fresh unweathered surfaces

GOOD - Rough, slightly weathered surfaces

FAIR - Smooth, moderately weathered and altered surfaces

POOR - Very smooth, occasionally slickensided surfaces with compact coatings or fillings with angular fragments

VERY POOR - Very smooth slicken-sided or highly weathered surfaces with soft clay coatings or fillings

A. Thick bedded, very blocky sandstone
The effect of pelitic coatings on the bedding planes is minimized by the confinement of the rock mass. In shallow tunnels or slopes these bedding planes may cause structurally controlled instability.

Very blocky

B. Sandstone with thin inter-layers of siltstone

C. Sandstone and siltstone in similar amounts

D. Siltstone or silty shale with sandstone layers

E. Weak siltstone or clayey shale with sandstone layers

C,D, E and G - may be more or less folded than llustrated but this does not change the strength. Tectonic deformation, faulting and loss of continuity moves these categories to F and H.

F. Tectonically deformed, intensively folded/faulted, sheared clayey shale or siltstone with broken and deformed sandstone layers forming an almost chaotic structure

G. Undisturbed silty or clayey shale with or without a few very thin sandstone layers

H. Tectonically deformed silty or clayey shale forming a chaotic structure with pockets of clay. Thin layers of sandstone are transformed into small rock pieces.

: Means deformation after tectonic disturbance

Marinos e Hoek (2000)

Figure 27 *GSI classification for extended geological settings* (Marinos & Hoek, 2000)

The more quantitative approach proposed by Cai et al. (2004) (**Figure 29**), is based on quantifying the average spacing of the different sets with reference to the volume of the reference block that characterizes the rock mass (Vb). The estimation of the weathering state is integrated through the use of a dimensionless factor, the Joint Condition factor (Jc) defined by the calculation of three parameters descriptive of roughness at different scales and of the alteration state of the surfaces:

$$J_c = \frac{J_w J_s}{J_a}$$

Equation 8

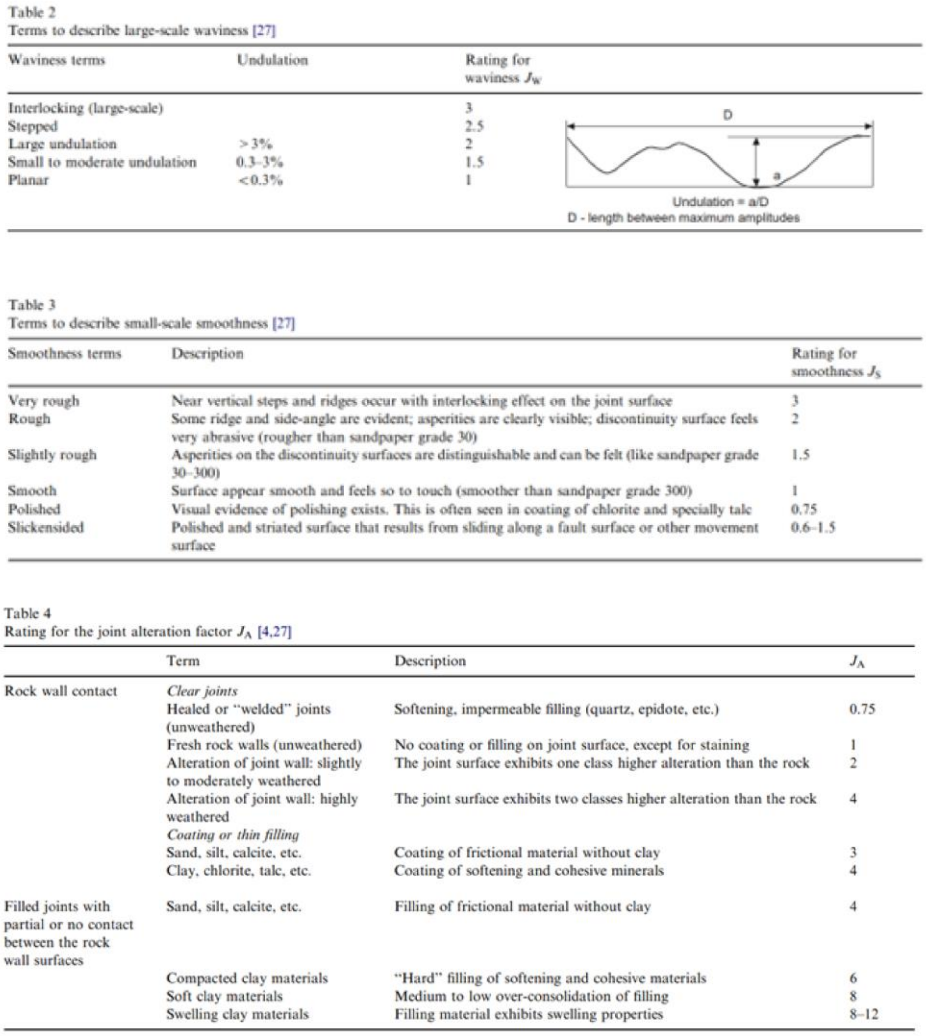

Table 2
Terms to describe large-scale waviness [27]

Waviness terms	Undulation	Rating for waviness J_W
Interlocking (large-scale)		3
Stepped		2.5
Large undulation	> 3%	2
Small to moderate undulation	0.3–3%	1.5
Planar	< 0.3%	1

Table 3
Terms to describe small-scale smoothness [27]

Smoothness terms	Description	Rating for smoothness J_S
Very rough	Near vertical steps and ridges occur with interlocking effect on the joint surface	3
Rough	Some ridge and side-angle are evident; asperities are clearly visible; discontinuity surface feels very abrasive (rougher than sandpaper grade 30)	2
Slightly rough	Asperities on the discontinuity surfaces are distinguishable and can be felt (like sandpaper grade 30–300)	1.5
Smooth	Surface appear smooth and feels so to touch (smoother than sandpaper grade 300)	1
Polished	Visual evidence of polishing exists. This is often seen in coating of chlorite and specially talc	0.75
Slickensided	Polished and striated surface that results from sliding along a fault surface or other movement surface	0.6–1.5

Table 4
Rating for the joint alteration factor J_A [4,27]

	Term	Description	J_A
Rock wall contact	*Clear joints*		
	Healed or "welded" joints (unweathered)	Softening, impermeable filling (quartz, epidote, etc.)	0.75
	Fresh rock walls (unweathered)	No coating or filling on joint surface, except for staining	1
	Alteration of joint wall: slightly to moderately weathered	The joint surface exhibits one class higher alteration than the rock	2
	Alteration of joint wall: highly weathered	The joint surface exhibits two classes higher alteration than the rock	4
	Coating or thin filling		
	Sand, silt, calcite, etc.	Coating of frictional material without clay	3
	Clay, chlorite, talc, etc.	Coating of softening and cohesive minerals	4
Filled joints with partial or no contact between the rock wall surfaces	Sand, silt, calcite, etc.	Filling of frictional material without clay	4
	Compacted clay materials	"Hard" filling of softening and cohesive materials	6
	Soft clay materials	Medium to low over-consolidation of filling	8
	Swelling clay materials	Filling material exhibits swelling properties	8–12

Figure 28 *Tables for Jw, Js and Ja asses fo Jc evaluation* (Cai et al., 2004).

In particular, the descriptive terms of *waviness* at different scales can be derived from the tables in **Figure 28**, as the one concerning the condition of surfaces.

Given its extreme in situ applicability and its strong empirical link to the quantitative aspects of defining the mechanical properties of the rock mass in terms of strength and deformability (**Figure 29**, **Figure 30** Hoek et al., 2002; Hoek & Diederichs, 2006) the GSI turns out to be one of the most recent and widely used classifications for rock mass quality.

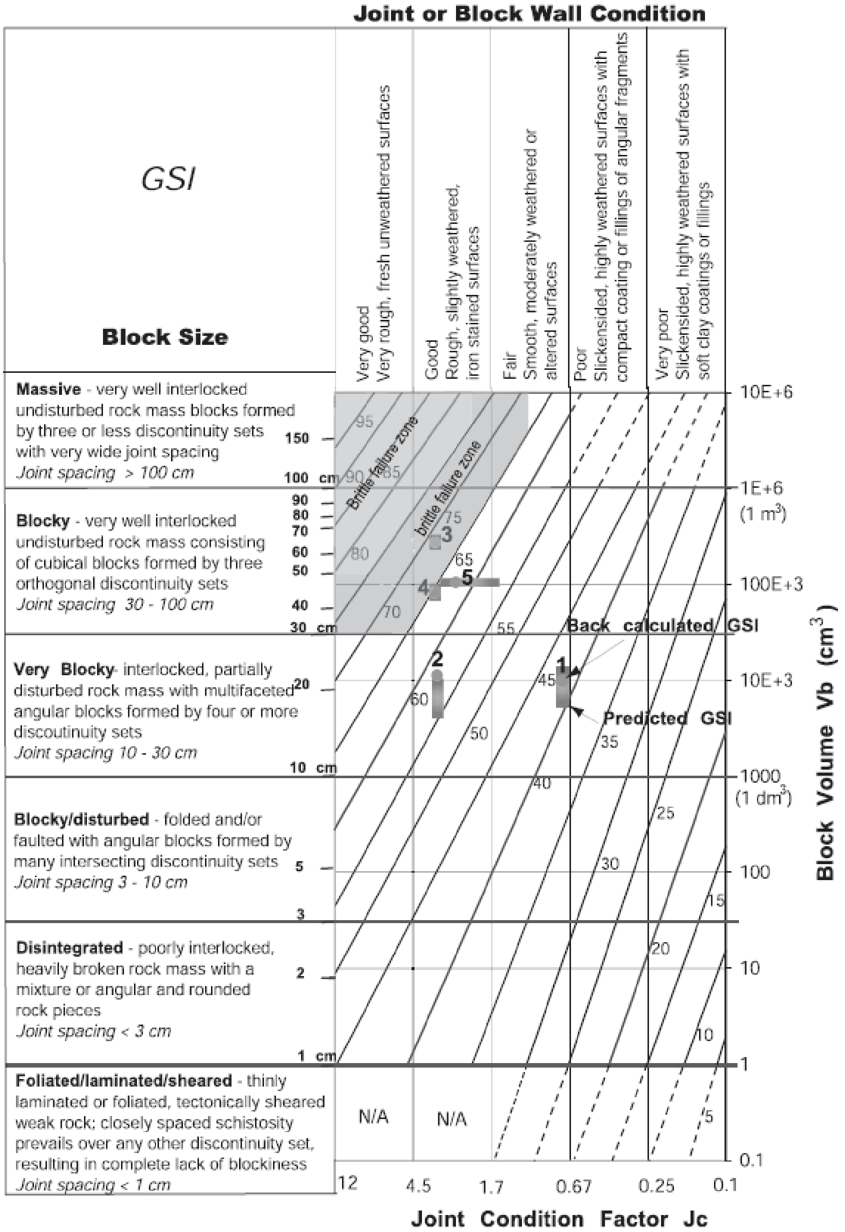

Figure 29 *GSI table in the version of* Cai et al., 2004*, based on quantitative measures (Vb, Jc).*

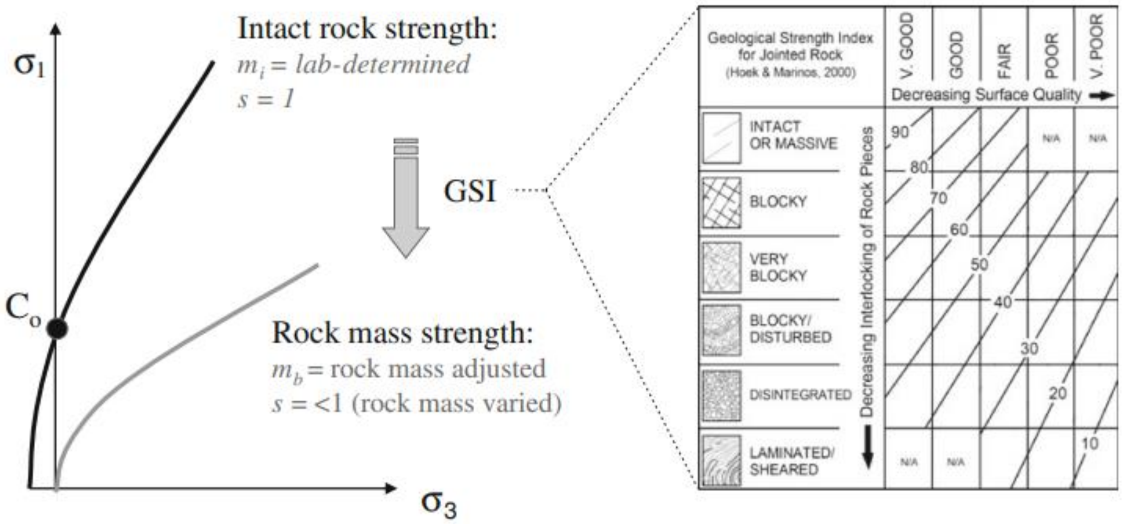

Figure 30 *Influence of GSI on for rock-mass strength (Eberhardt, 2012)*

2.7 Quantification of rock fracturing state: techniques

The study of fracturing of rock volumes can be derived with the support of various technologies, both at the laboratory scale and *in situ*. Among the most effective methods for estimating rock fracturing at the laboratory scale is x-ray microtomography, but it does not present applicable to *in situ* contexts. In recent years, the analysis of Digital outcrop Models (DOMs) obtained through various remote geometric outcrop reconstruction technologies has greatly facilitated the study and characterization of biased fracturing metrics, even at large scales. Innovative approaches using remote contactless methodologies have been used in the recent literature, such as IRT.

2.7.1 X-ray microtomography

X-ray microtomography (Micro CT; Keller, 1998; Montemagno & Pyrak-Nolte, 1999; Landis & Keane, 2010) is an advanced imaging technique that enables the characterization of a rock sample's microstructure in 3D without causing any damage. It achieves high-resolution imaging, with the ability to resolve features at the nanometer scale. The fundamental principle of Micro-CT involves the acquisition of a series of 2D X-ray images as the sample rotates around a single axis. These 2D images are then reconstructed to generate a detailed 3D image, where each voxel represents the X-ray absorption at that specific point within the sample (Landis & Keane, 2010).

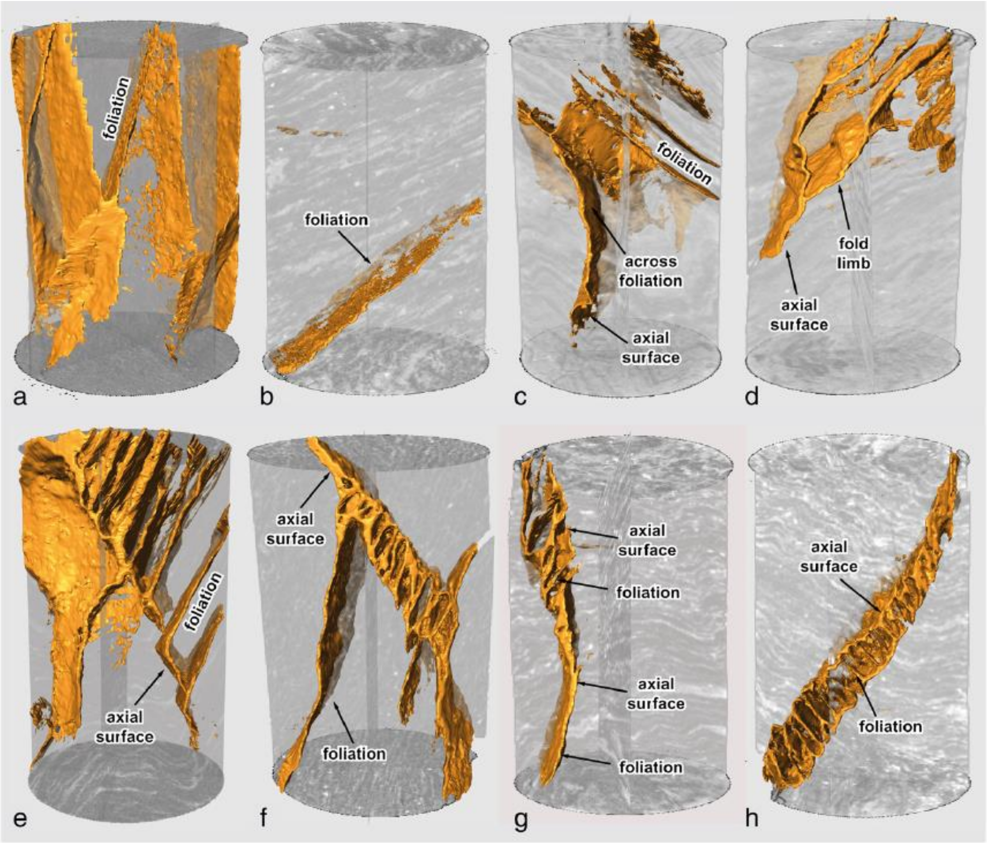

Figure 31 *3D fracturing porosity of cilyndrical rock-samples (gneiss) reconstructed by Micro-CT scanning (Agliardi et al., 2014)*

One of the key advantages of Micro-CT is its ability to correlate X-ray absorption with material density. This correlation allows the internal structure of the sample to be visualized and analyzed. Differences in X-ray absorption can be utilized to identify and distinguish various phases within the sample. In our context, the primary distinction lies between intact rock and voids, as the voids are typically filled with air which make it possible to separate intact rock and 3D network of fracture/pores volumes (**Figure 31**). The technique's resolution is determined by the characteristics of the X-ray beam geometry and the sensor used for image acquisition.

The Micro-CT technique in rock mechanics is applied to the study of the internal structure of samples, for the study of porosity (Montemagno & Pyrak-Nolte, 1999; Pappalardo et al., 2016) and fracturing (Agliardi et al., 2014, 2017; Franzosi et al., 2023a), as it is the only technique that allows the quantitative values of P_{33} and P_{32} and thus the 3D fracture state of a rock volume to be reconstructed without systematic errors, but is strongly limited by the scale of applicability, in fact it can be used only at laboratory scales.

2.7.2 Digital outcrop model (DOM) analysis

The fracture sampling strategies described above have been supported in the last decades by the increased use of remote techniques for the construction of large-scale Digital Outcrop Models (DOM; Bellian et al., 2005; Hodgetts, 2013; Bistacchi et al., 2022) which have increased the amount of data for geometric characterization of the rock-mass and discontinuity sets (Jaboyedoff et al., 2007; Riquelme et al., 2015). This provides useful elements for understanding the 3D structure of the fracture network and the possibility of repeating statistical measurements of fracture metrics on a larger scale. In particular:

- **Terrestrial Laser Scanning (TLS)**: The LIDAR (Light Detection and Ranging) technique is an advanced detection method that uses the emission and detection of laser pulses to measure time of flight, thereby measuring the 3D position of the point target in the space (**Figure 32**). This laser-based measurement system allows the rapid acquisition of detailed point data describing a terrain surface, from both aerial and terrestrial platforms, acquired remotely over distances of up to 2-3 km (Buckley et al., 2008). The main output of the LIDAR technique is a three-dimensional point cloud (Leberl et al., 2010) expressed in 3D coordinates georeferenced which resolution depends on acquiring distance and laser scanner properties (Abellán et al., 2014) reaching up to mm for terrestrial acquisitions (Jaboyedoff & Derron, 2020).

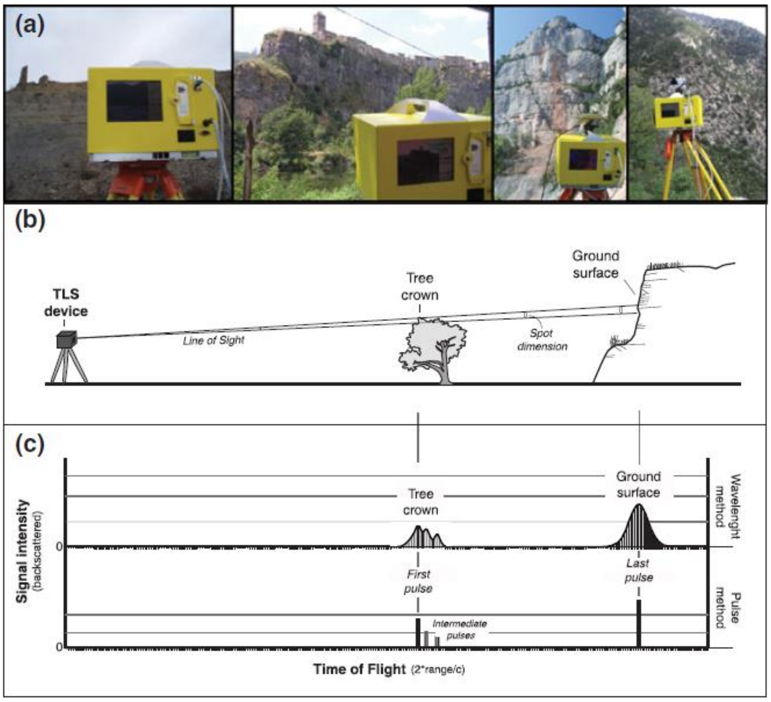

Figure 32 *TLS application for rock-mass geometry reconstruction* (Abellán et al., 2014)

- **Structure from Motion photogrammetry (SfM):** it is an evolution of traditional photogrammetry, a technique that allows to determine the 3D coordinates of points in a reference system through 2D photographic images of the same (**Figure 33**; Agisoft, 2018) taken from different shooting points.
  The SfM represents an evolution as it allows to identify objects invariant to scale and rotation (SIFT algorithm; Markel, 1972), automatically and simultaneously reconstructing both the 3D geometry of the scene and the camera shooting positions, through optical reprojection equations (Agisoft, 2018).
  The high-resolution photos can be taken both from the ground and from aerial supports (Airplanes, Drones; Sanz-Ablanedo et al., 2018, Nesbit & Hugenholtz, 2019), always respecting the guidelines for a correct geometry of shooting points, returning a 3D cloud of the rock outcrop with resolution up to mm and with RGB attribute.

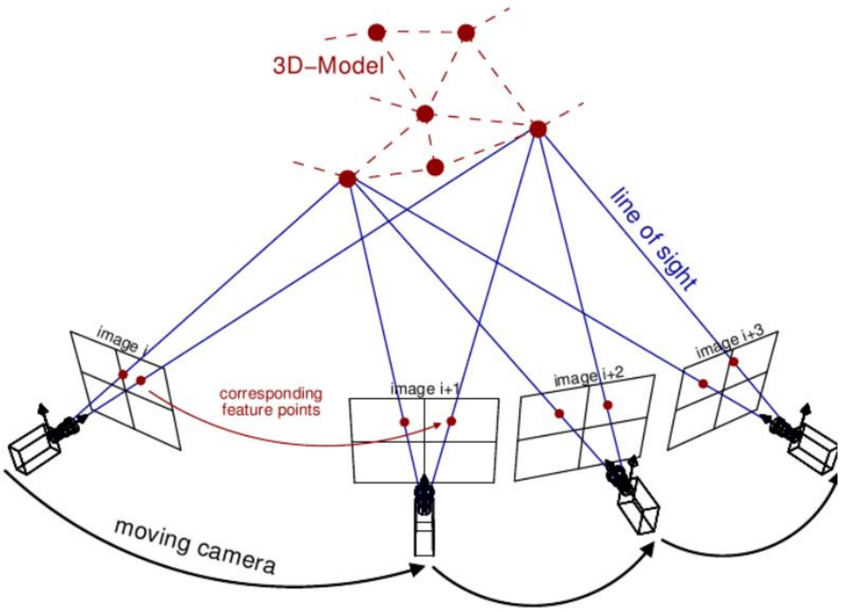

Figure 33 *Scheme about principles of photogrammetry acquisition and reconstruction* (Van Riel, 2016)

The point cloud obtained through LiDAR/SfM represents the surface of the object or environment being scanned.

This information is very useful for constructing detailed and accurate DOMs that enable the characterization of rock mass outcrops by detecting systematically the surfaces and traces of fractures present in outcrops, returning a detailed 3D geometry of outcrop faces (Jaboyedoff et al., 2007; Gigli & Casagli, 2011; Riquelme et al., 2015). DOMs can be used to perform discrete analyses on fractures or used to better perform sampling strategies (e.g linear, areal) in a remote way. These techniques improve the calculation of biased metrics of fracturing (e.g P_{21}) through direct fracture characterization approaches, that requires individual fracture identification and mapping, spacing analysis and the estimation of fracture density (Martinelli et al., 2020). These techniques are usually used to investigate rock-mass scale but can be applied also at smaller scales.

2.7.3 Infrared Thermography (IRT)

The Infrared Thermography (IRT) technique has been widely applied in engineering for non-destructive testing of material defects and fatigue (Clark et al., 2003; Ibarra-Castanedo et al., 2017), its application to geosciences has been mainly focused on mapping and monitoring volcanic, geomorphological and hydrological processes (Moran, 2004;

Spampinato et al., 2011; Mineo et al., 2015; Teza et al., 2015; Frodella et al., 2017; Guerin et al., 2019).

Applications of Infra-Red Thermography (IRT) to rock-mechanics and engineering mainly consisted in the empirical correlation between the response of intact rocks to thermal perturbations depending on different parameters (**Figure 34**) characterized in the laboratory (stress, water saturation and porosity, fracture abundance; Mineo & Pappalardo, 2016, 2019; Cai et al., 2020; Song et al., 2021).

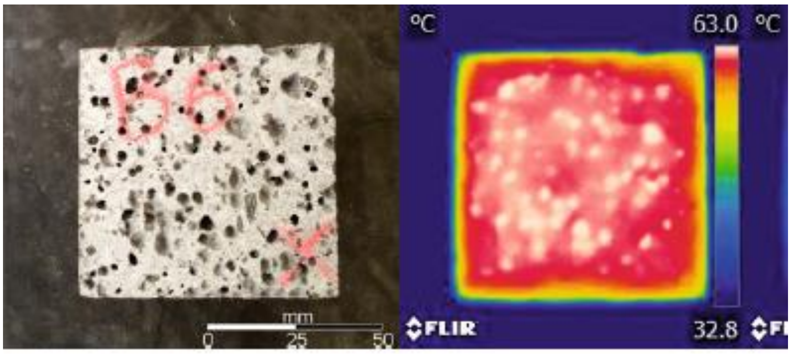

Figure 34 *IRT application in rock porosity assessment (Mineo et al., 2015)*

Some authors applied IRT to the empirical characterization of rock mass quality on the scale of small outcrops (Teza et al., 2012; Pappalardo et al., 2016; Grechi et al., 2021) or to the qualitative characterization (**Figure 35**) of slope instabilities (Baroň et al., 2014; Mineo et al., 2015, 2022; Teza et al., 2015; Frodella et al., 2017; Guerin et al., 2019; Loiotine et al., 2022; Caliò et al., 2023;).

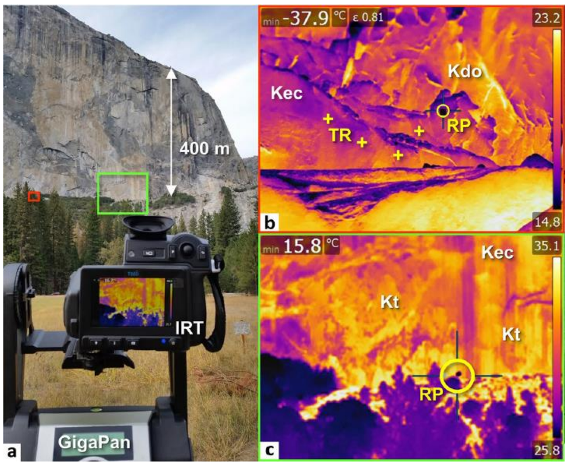

Figure 35 *IRT application in flakes detection on El Capitan cliff (Yosemite valley, CA)* (Guerin et al., 2019)

In particular, pioneering work investigating the effect of fracturing on the thermal response of rock volumes (**Figure 36**) suggests empirical relationships between cooling rate and fracture state or block size (Teza et al., 2012; Pappalardo et al., 2016; Caliò et al., 2023).

In particular, the existing relationship between fracturing and cooling speed has been investigated by some authors using the Cooling Rate Index (CRI; Mineo & Pappalardo, 2016; Pappalardo et al., 2016), which describes the temperature variation in a defined time window during cooling, describing only a part of the curve depending on the boundary conditions. Furthermore, pioneering CRI methodologies proposed so far do not fully exploit the spatially widespread character of thermal imaging which can be particularly useful in systematically mapping the thermal response of a rock mass at larger scales.

While the empirical experimental relationships suggest the correlation between the increase in CRI and variables such as the increase of porosity/fracturing of the rock volume (**Figure 36**) both in the laboratory and in situ, a systematic, physically based and quantitative approach still seems to be lacking across scales.

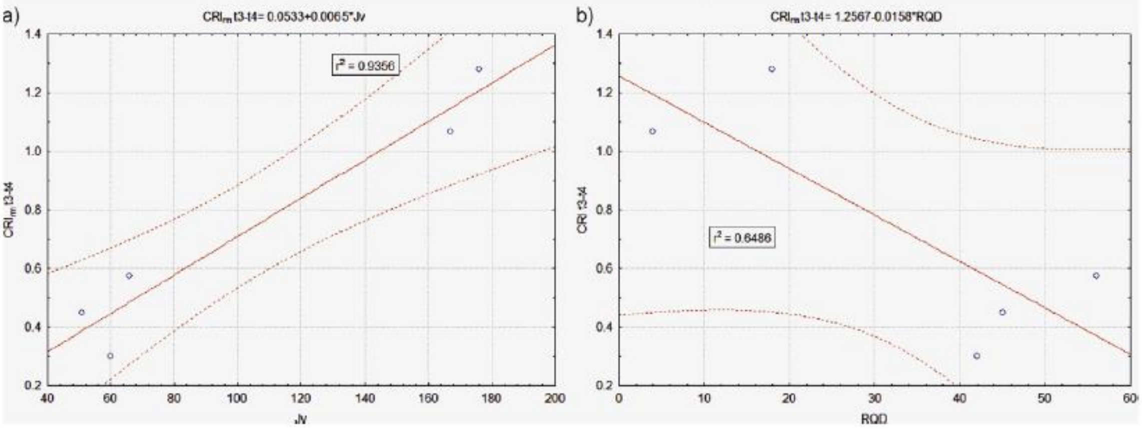

Figure 36 *Relation between rock mass fracture indexes (Jv,RQD) and cooling rate* (Pappalardo et al., 2016)

2.7.4 Applicability and limits of rock fracturing quantification techniques

Fracturing state in rocks can therefore be determined at different scales and with different techniques. In general, we defined how, on a laboratory scale, fracturing can be determined in an unbiased way (P_{33}, P_{32}) through non-invasive 3D imaging tests, while in situ these techniques appear to have a scale limit of practical applicability or resolution, which is the motivation to use direct survey techniques of discontinuities, used both in the field and remotely by digital reconstruction technologies of the natural outcrops. Despite their wide applicability, these techniques offer estimates of fracturing parameters (P_{21}) affected by systematic errors (directional and dimensional biases) and these techniques can lose representativeness in extremely fractured rock masses. Some authors have proposed the use of an innovative remote sensing technique such as IRT for the estimation of the fracturing state of rock masses and the characterization of single fractures, suggesting their link with thermal behavior. Although pioneering, this perspective has often been explored qualitatively, or without exploring physically based approaches without providing actual practical in situ experimental procedures.

3 Conceptualization: thermal response of fractured media

3.1 Research questions

In the present work, we asked whether it is possible to characterize the thermal response of a fractured rock medium (rock samples to rock mass) experimentally in order to indirectly determine its fracturing state. In particular, starting from the empirical experiences in existing literature, we develop the following research questions:

- Is it possible to find a physical link between degree of fracturing and thermal response of the fractured rock put to perturbations (e.g., heating, cooling)?
- Is it possible to meaningfully measure differences in thermal behavior between media characterized by different degrees of fracturing?
- Is it possible to quantify these differences to develop quantitative diagnostic methodologies for fracturing degree assessment?

In order to address the problem, compositional characters that may influence the thermal properties of rocks and those of discontinuities (geometry, aperture, intensity, heterogeneity) that may affect the heat transfer process in a fractured medium in the transient regime were considered within the theoretical framework summarized below.

3.2 Theoretical aspects: conduction, convection, and radiation

The kinetic temperature T_K of a body is proportional to the excitation (i.e velocity) of its particles expressed as kinetic energy by:

$$T_K = \frac{2}{3K} E$$

Equation 9

Where:

T_K is the kinetic temperature *(K)*

K is the Boltzmann constant *(JK^{-1})*

E is kinetic energy of particles *(J)*

The thermal energy stored in a body in the form of heat is related to the temperature change it undergoes, according to;

$$Q = mc_p\Delta T$$

Equation 10

Where:

Q is heat *(J)*

m is body mass *(Kg)*

c_p is the specific heat *($JKg^{-1}K^{-1}$)*

ΔT is temperature variation (*K*)

Heat transfer between solid bodies and their surroundings occur by conduction (diffusion), convection and radiation processes (Bergman et al., 2011).

Heat conduction is the result of direct kinetic energy exchanges among particles within a solid or fluid at rest, depending on the thermal characteristics and size of the object. Such spontaneous heat transfer always occurs following temperature gradients, as described in the second law of thermodynamics.

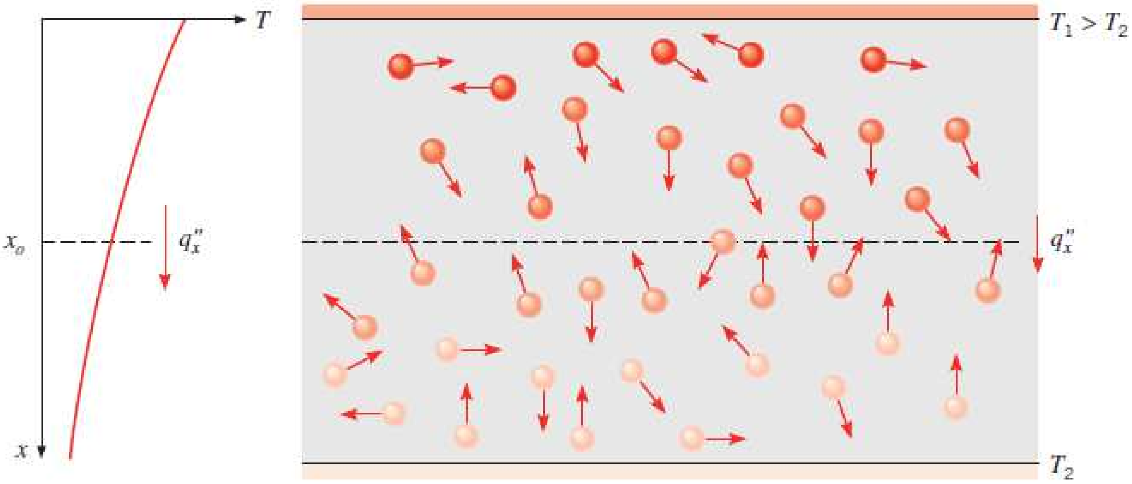

Figure 37 *Heat transfer in a solid material through conduction process* (Bergman et al., 2011).

Heat transfers from warmer to cooler systems with a rate proportional to the temperature difference and the surface area of the body. Within a solid material, in terms of conduction (**Figure 37**) this process so can be expressed as:

$$q = k(T_{hot} - T_{cold})\frac{A}{L}$$

Equation 11

Where:

q is the heat rate (W)

k: thermal conductivity $(Wm^{-1}K^{-1})$

A: heat transport cross section (m^2)

L heat transport distance (m)

T_{hot}: temperature of the hot system (K)

T_{cold}: cold system temperature (K)

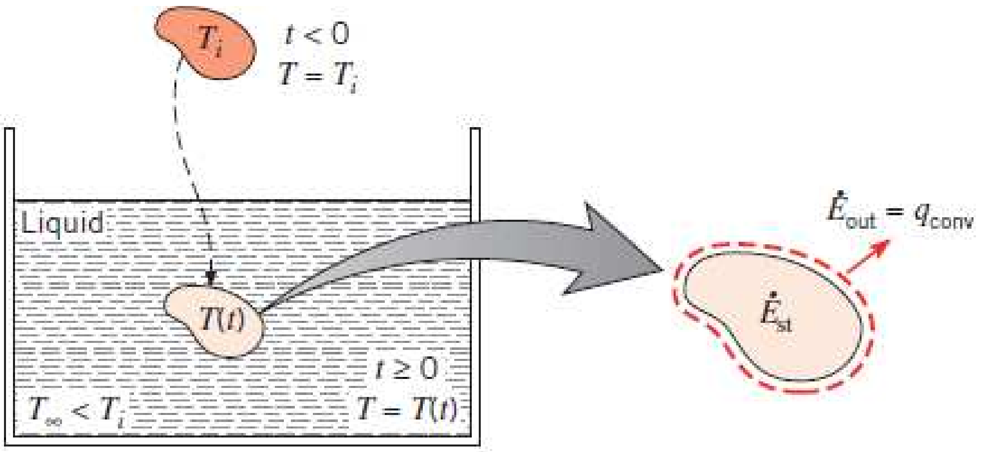

Figure 38 *Volume of a heated material that cools inside a cooler fluid through convection* (Bergman et al., 2011)

When energy is transferred by mass transport, at the interface of a solid material immersed in a fluid at different temperature (e.g air) , the process is instead described by convection (**Figure 38**), according to:

$$q = h(T_{hot} - T_{cold})A$$

Equation 12

Where:

h: convection coefficient $(Wm^{-2}K^{-1})$

A: interface section *(m^2)*

If the temperature is greater than absolute zero, particles start to oscillate, collide, and vibrate. These motions produce a local variation in electron density that generates electromagnetic radiation. According to Planck's law, the spectral radiance emitted by a complete absorbing body (i.e. black body, Vollmer & Möllmann, 2018) at a temperature T can be expressed by the formula:

$$Md\lambda = \frac{2h_b c^2}{\lambda^5 e^{(h_b c/K\lambda T)} - 1} d\lambda$$

Equation 13

Where:

M_λ is spectral radiance emitted by the body *($Wm^{-2}sr^{-1}\mu m^{-1}$)*

T is body temperature *(K)*

λ is the wavelength *(μm)*

h_b is Planck constant *(J·s)*

c is the speed of light *(ms^{-1})*

K is Boltzmann constant *($J\,K^{-1}$)*

3.3 Conduction process

In the presence of a temperature gradient, energy transfer by conduction must then occur in the direction of decreasing temperature. The equation governing heat conduction inside the material is Fourier's Law, which for a one-dimensional problem can be expressed as:

$$q_x'' = -k \cdot \frac{dT}{dx}$$

Equation 14

Where:

q_x'' is the heat transfer flux along the x direction (Wm^{-2})

In general, the direction of heat flow is always normal to the isotherm, that is, to a surface at constant temperature. The equation can be generalized for all directions, thus obtaining:

$$q'' = -k\,\nabla T$$

Equation 15

Where:

$\nabla T = i\frac{\Delta T}{dx} + j\frac{\Delta T}{dy} + k\frac{\Delta T}{dz}$

Thermal conductivity can be obtained by deriving the Fourier equation, assuming one-dimensional flow in the x-direction, we obtain:

$$k = \frac{q''_x}{({}^{dT}/_{dx})}$$

Equation 16

Thermal conductivity is a material-dependent property; in particular, the conductivity of a solid can be up to four orders of magnitude greater than that of a gas.

Thermal properties of a material can be divided into transport properties, for example, thermal conductivity, and thermodynamic properties, which refer to the equilibrium state of a system. Of last cited category we can define Volumetric Heat Capacity, which indicates the ability of a material to store thermal energy, defined as:

$$VHC = \rho \cdot c_p$$

Equation 17

Where:

VHC: volumetric heat capacity $(JK^{-1}m^{-3})$

The ratio of thermal conductivity to volumetric heat capacity determines the thermal diffusivity of a material:

$$\alpha = \frac{k}{\rho c_p}$$

Equation 18

Where:

α: diffusivity *($m^2 s^{-1}$)*

This parameter measures the ability to conduct energy versus the ability to store energy. The equation that governs heat conduction is called the heat diffusion equation and it allows us to obtain the spatial temperature distribution over time of a body:

$$\frac{d}{dx}\left(k\frac{dT}{dx}\right) + \frac{d}{dy}\left(k\frac{dT}{dy}\right) + \frac{d}{dz}\left(k\frac{dT}{dz}\right) = \rho c_p \frac{dT}{dt}$$

Equation 19

The important implication of this result is that, under *steady-state*, one-dimensional conditions with no energy generation, the heat flux is a constant in the direction of transfer.

3.4 Transient conduction: Lumped Capacitance Method (LCM)

While the temporal trend of temperature during heating strongly depends on the thermal forcing (i.e. amount and temporal distribution of heat transferred to the body), the process of *transient* cooling (i.e. temperature decrease occurring when no additional heating is applied) follows a relatively simple exponential trend, described as the "Newton's law of cooling" (Vollmer, 2009; Bergman et al., 2011):

$$T_{surf} = T_\infty + (T_0 - T_\infty)e^{-\theta t}$$

Equation 20

Where:

T_∞: temperature of the environment *(K)*

T_0: temperature of the object at starting of cooling *(K)*

θ: constant that depends on the surface and nature of the object *(s^{-1})*

t: time (s)

A solid body heated by an artificial (e.g furnace) or natural (e.g solar) source tends to balance its thermal state with the surrounding environment by cooling at a rate depending on its thermal properties, chemical composition, geometry, and boundary conditions. In fact, a hot body exposed to a cool airstream will transfer heat by conduction across its interior to the surface, and by convection from its surface to the surrounding fluid. At each point in the body, the temperature will decrease until a steady state is achieved (Bergman et al., 2011).

In this context, transient heat transfer by conduction (i.e diffusion) is characterized by the dimensionless Fourier number (Fo):

$$F_0 = \frac{\alpha t}{L_c^2}$$

Equation 21

Where:

α is thermal diffusivity ($m^2 s^{-1}$)

t is time (s)

L_c is a body characteristic size along direction of heat transfer (m)

While the role of convective heat transfer is controlled by the dimensionless Biot number (**Figure 39**):

$$B_i = \frac{hL_c}{k}$$

Equation 22

Where:

h is convection coefficient ($Wm^{-2}K^{-1}$)

k is thermal conductivity ($Wm^{-1}K^{-1}$)

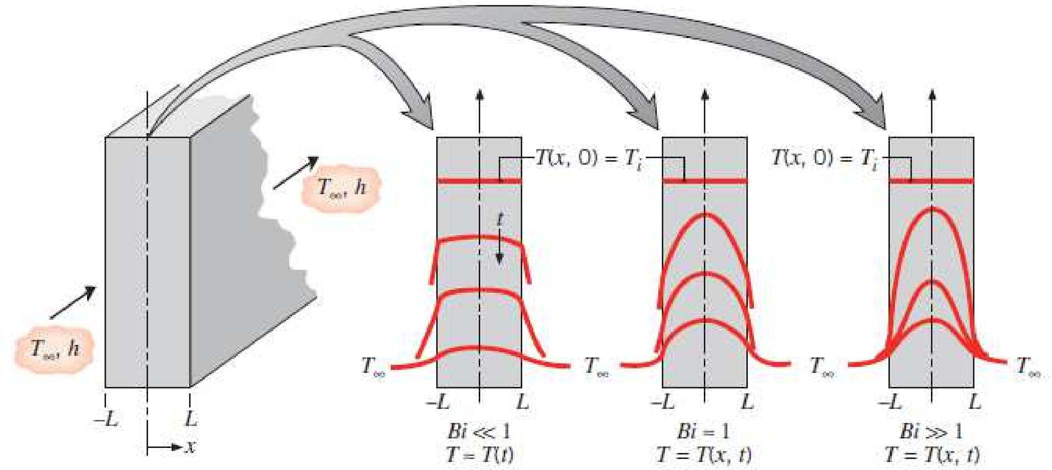

Figure 39 *Variability of Biot number in function of the temperature distribution inside a material during cooling* (Bergman et al., 2011).

When the Biot number is < 0.1 (**Figure 40**), the internal heat flow is much larger than the heat loss from the surface, and temperature gradients within the body can be considered negligible. In this case, the cooling dynamics of a body with initial temperature T_i that cools down to the ambient temperature T_∞ can be described by the simplified "lumped capacitance" equation (Bergman et al., 2011):

$$\frac{T_{(t)} - T_\infty}{T_0 - T_\infty} = e^{-B_iF_0} = e^{-\frac{h\alpha}{kL_c}t}$$

Equation 23

Where:

T_0 is the initial temperature of the body at t=0 (K)

T_s is the temperature of the body at t=t$_s$ (K)

T_∞ is the temperature of the body surroundings (K)

t is time (s)

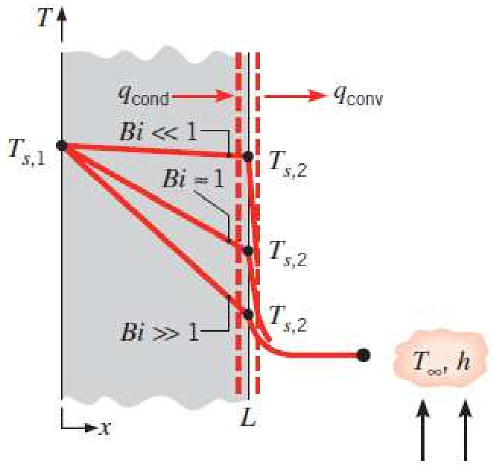

Figure 40 *Conceptual scheme of interaction between conduction and convection processes during transient cooling of a infinite plane wall* (Bergman et al., 2011).

3.5 Research hypothesis

According to the above equations, the cooling rate of a solid body depends on material properties, the nature and flow velocity of the surrounding fluid, and a characteristic length (i.e., size or volume to surface area ratio), with smaller bodies cooling faster.

To apply these concepts to a fractured rock system, we hypothesize that the fracturing state affects two main components of the cooling equation, namely: the characteristic length (L_c), since higher fracture intensity corresponds to smaller elementary rock blocks; the convection coefficient at interfaces between fractured block, especially when fractures are open. Then, for a material with a given composition and size it should be possible to find a relationship between the fracturing state and the cooling rate (**Figure 41**).

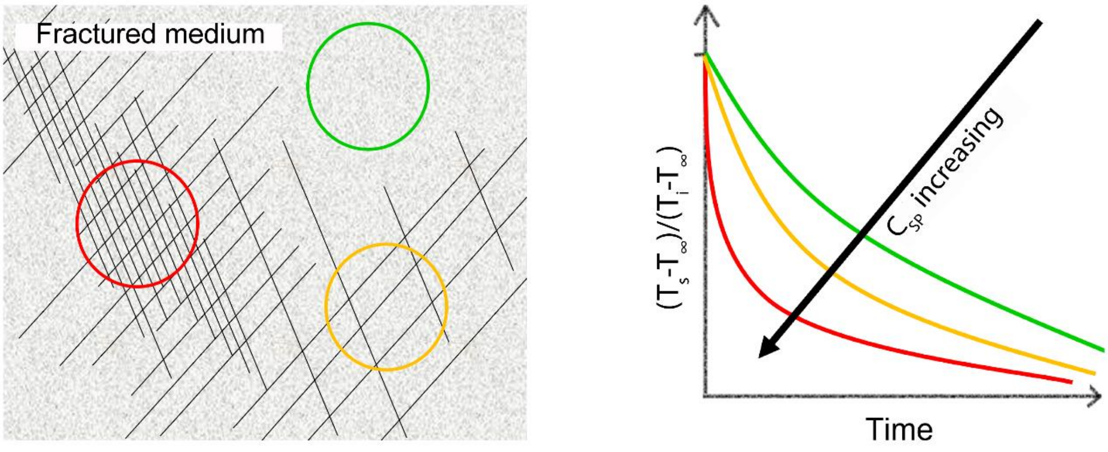

Figure 41 *Conceptual scheme of C_{SP} relationship with rock fracturing state (after Franzosi et al., 2023a).*

Parametrizing the **Equation 23** is possible to define a synthetic descriptor of cooling rate, the Curve Shape Parameter (C_{SP}; Franzosi et al., 2023a):

$$C_{sp} = \frac{h\alpha}{kL_c}$$

Equation 24

Where:

C_{SP} is curve shape parameter (s^{-1} or h^{-1})

The C_{SP} (**Figure 41**) provides a synthetic description of the shape of experimental cooling curves, independent on absolute thermal boundary conditions, yet incorporating thermal properties of the rock material (k,α), the boundary convective condition of the solid-air interface (h), and the representative size of radiant element (i.e. rock blocks / fragments).

3.6 Preliminary experiment: C_{SP} and rock block-size

We conducted a preliminary test using simple gneiss cubes with edges between 3 cm and 7 cm, heating them in an oven (up to 70°C) and then letting them cool down to a constant room temperature (**Figure 42.a**). We monitor their temperature during cooling with an IR-camera (see next section). As we can see from the output obtained, there are clear increases in the C_{SP} values as a function of the cube's volume (**Figure 42.a-c**), the theoretical framework above.

It is important to emphasise that the clarity of the results obtained is related to several factors: a) the controlled heating and cooling conditions; b) the indoor acquisition in a controlled environment; c) the high thermal gradient with respect to the equilibrium condition.

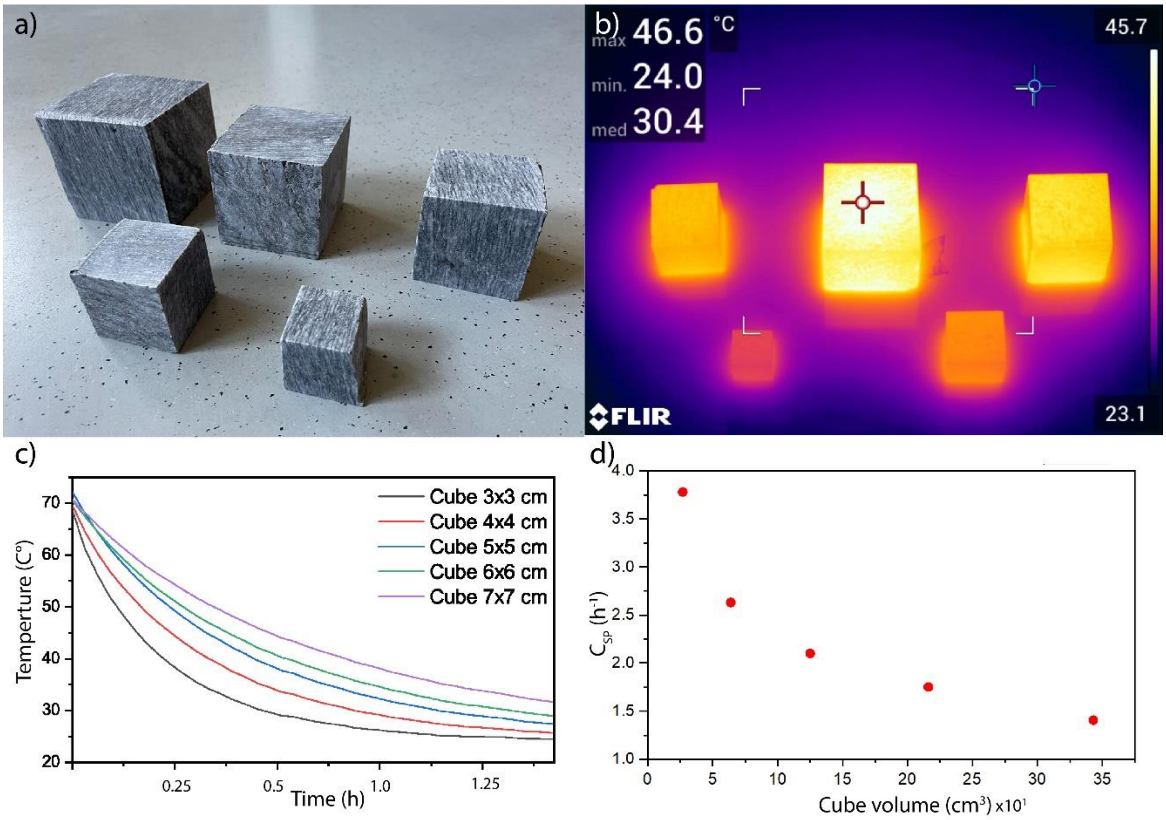

Figure 42 *The experiment show (a) the rock cubes, simulating "rock-blocks" with different size, heated and monitored during cooling through Infra-Red Thermography acquisitions (see after). Cooling histories (c) and their parametrization with* C_{SP} *(d) show clear correlation between thermal response and cube size.*

Furthermore, the observational scale of the experiment accounts a range of small rock volumes, where the ratio of volume to free surface area grows more steeply (Characteristic length, Bergman et al., 2011; Franzosi et al., 2023a) than larger volume ranges such as those encountered at the outcrop scale. The strong signal we detect in the preliminary experiment is very recognisable and emphasized (**Figure 42**) due to all the reasons explained above, certifying the theoretical aspects explored previously and acting as a starting point for the next steps in this work.

The experiment therefore demonstrates that the thermal response of a rock volume is directly related to its size, and that the parameterization of its cooling history allows to discriminate between different rock volumes using a contactless temperature monitoring technique (Infra-Red Thermography). The increasing fracturing in a rock volume isolates ever smaller elementary volumes, is it therefore possible to differentiate the state of fracturing through this approach on a laboratory scale? If yes, is it possible to discriminate the signal of this physical mechanism on a larger scale in natural environments?

3.7 Measurement technique: Infra-Red Thermography

Infra-Red Thermography (IRT) is an innovative technique applied only in recent years for geological research purposes, that represents the only remote sensing technique to provide temperature data of the surface of a body in a contactless and spatially distributed way.

3.7.1 IRT fundamentals

All objects at temperatures above absolute zero emit radiation because of their kinetic energy (Vollmer & Möllmann, 2018) in the electromagnetic spectrum, depending on the temperature and properties of the object. Planck's law (**Equation 13**) in relation to the temperature of a body describes the amount of the radiation emitted by a body at a given temperature in a defined wavelength of the electromagnetic spectrum.

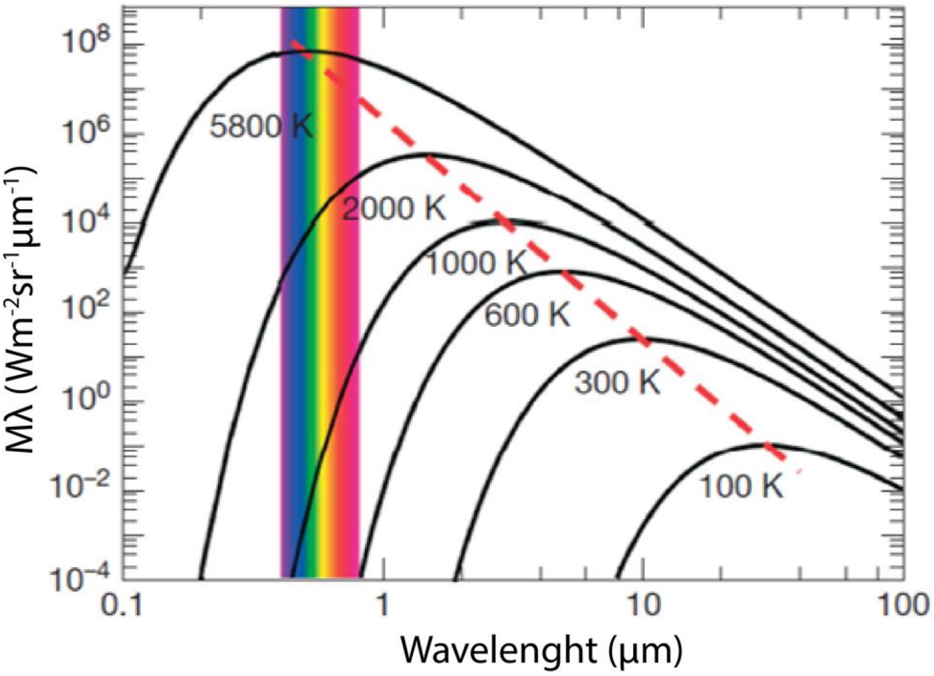

Figure 43 *Plank and Wien law* (Vollmer & Möllmann, 2018)

This equation shows that the intensity of the radiation emitted by a body increases with the frequency of the radiation and decreases with the temperature of the body.

Furthermore, Planck's law states that the radiation emitted by a body has a continuous spectrum, which means that the body emits radiation at all frequencies in the range of the electromagnetic spectrum. Planck's law can then be visualized as in the graph in **Figure 43**, in which we can see that each temperature has an emission peak at a given wavelength (λ_{PEAK}) in the electromagnetic spectrum, which is described by Wien's law:

$$\lambda_{PEAK} = \frac{A}{T}$$

Equation 25

Where:

λ_{PEAK} is the wavelength (*μm)*

A is Wien constant ($\mu m\ K^{-1}$)

T is body temperature (*K*)

Integrating the Plank's law is possible to obtain the total energy emitted by the body in the electromagnetic spectrum ($0 < \lambda < \infty$), as radiant exitance (J) expressed as the Stephan Boltzmann law (**Figure 44**):

$$J = \varepsilon\sigma T^4$$

Equation 26

Where:

J is thermal radiant exitance (Wm^{-2})

T is temperature of the body (*K*)

σ is Stefan-Boltzman constant ($Wm^{-2}\ K^{-4}$)

ε is emissivity of the material (-)

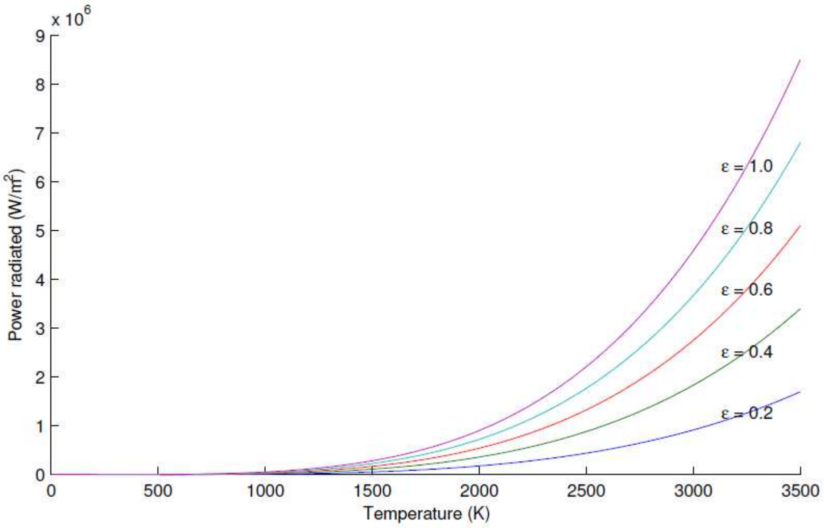

Figure 44 *Boltzman law* (Usamentiaga et al., 2014)

The emissivity ε can be guessed from Kirchhoff’s law, which states that the amount of radiation absorbed by any object is equal to the amount of radiation that is emitted by this object. This is usually written in the form:

$$\varepsilon = \gamma$$

Equation 27

Where:

γ is absorptivity (-)

Emissivity and absorptivity denote the fraction of radiation that is either emitted or absorbed. Energy conservation requires that any radiation (Φ_0) incident on any object must be reflected (Φ_R), transmitted (Φ_T) through the object, or absorbed (Φ_A) within the object:

$$\Phi_0 = \Phi_R + \Phi_T + \Phi_A$$

Equation 28

Considering the fraction of the incident radiation (e.g., in excitance or radiance);

$$1 = R + T + \gamma$$

Equation 29

R is fraction of radiation emitted (-)

T is fraction of radiation transmitted (-)

The simplest examples are opaque solids with T = 0. In this case, emissivity can be defined as:

$$\varepsilon = 1 - R$$

Equation 30

If $\varepsilon = 1$, we talk about *blackbody*. *Blackbodies* are idealizations, and no real object can emit the maximum thermal radiation at a given temperature. The real emission of thermal radiation from any object can, however, be easily computed by multiplying the blackbody radiation by the emissivity ε. In other words: the emissivity of an object is the ratio of the amount of radiation actually emitted from the surface to that emitted by a blackbody at the same temperature (**Figure 45**, Vollmer & Möllmann, 2018):

$$\varepsilon(\lambda, T) = \frac{Real\ body\ Radiance}{Black\ body\ Radiance}$$

Equation 31

We can talk about three classes of emittors:

- Black bodies ($\varepsilon = 1$): absorb all incidence radiation received by the surrounding and emit only the maxim thermal radiation for their temperature.
- Grey bodies ($\varepsilon < 1$): reflect part of the incidence radiation received by the surrounding and emit only a percentage of thermal radiation for their temperature.
- Reflectors (ε~0): reflect all the incidence radiation received by the surrounding.

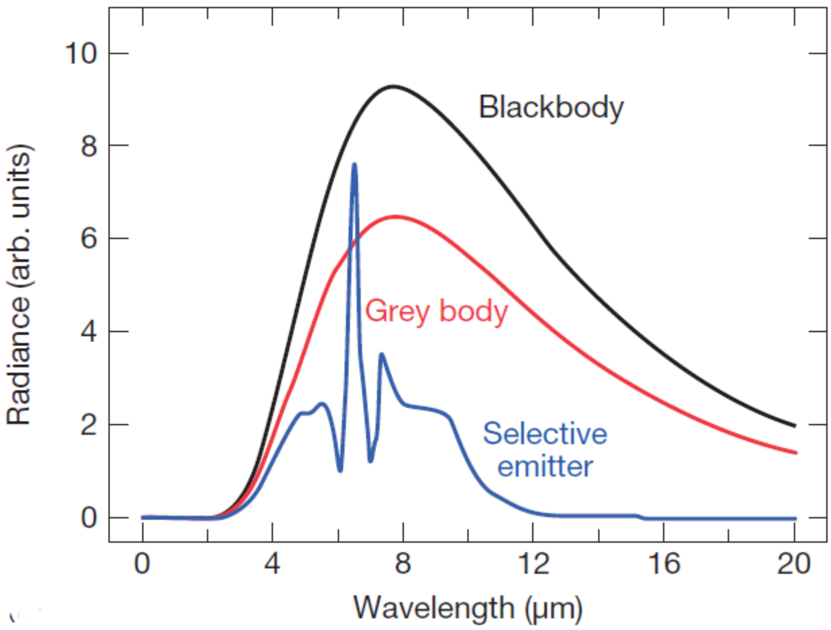

Figure 45 *Differences in radiance in function of bodies's emissivity (Vollmer & Möllmann, 2018)*

According to the Planck's radiation law, it is possible to measure the surface temperature of objects based on their emitted radiation in specific IR wavelength ranges, using a technique called Infrared Thermography (IRT, Shannon et al., 2005; Vollmer & Möllmann, 2018).

Using modern IR thermal cameras so it is possible to measure the Infrared radiation emitted by bodies in the spectral band 7.5-14 µm , that is the spectral band of greatest emission under the typical temperature conditions of the earth's surface (LW cameras, **Figure 43**, **Figure 46**) in a spatial distributed way, producing thermal images (i.e Thermograms).

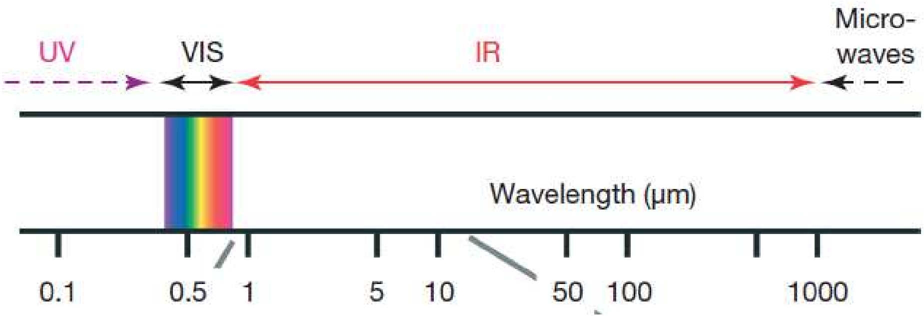

Figure 46 *Complete wavelength spectrum (Vollmer & Möllmann, 2018)*

3.7.2 IRT controls in outdoor environments

Thermal imaging cameras record the radiance of surfaces in the framed scene and convert it to apparent temperature. The raw measurement of the thermal camera is named apparent because it may be different from the kinetic measurement of the framed object; in fact, it needs to be corrected and calibrated for emissivity of the material, and purified of the contributions of the environmental radiation that is reflected from the object itself (**Figure 47**).

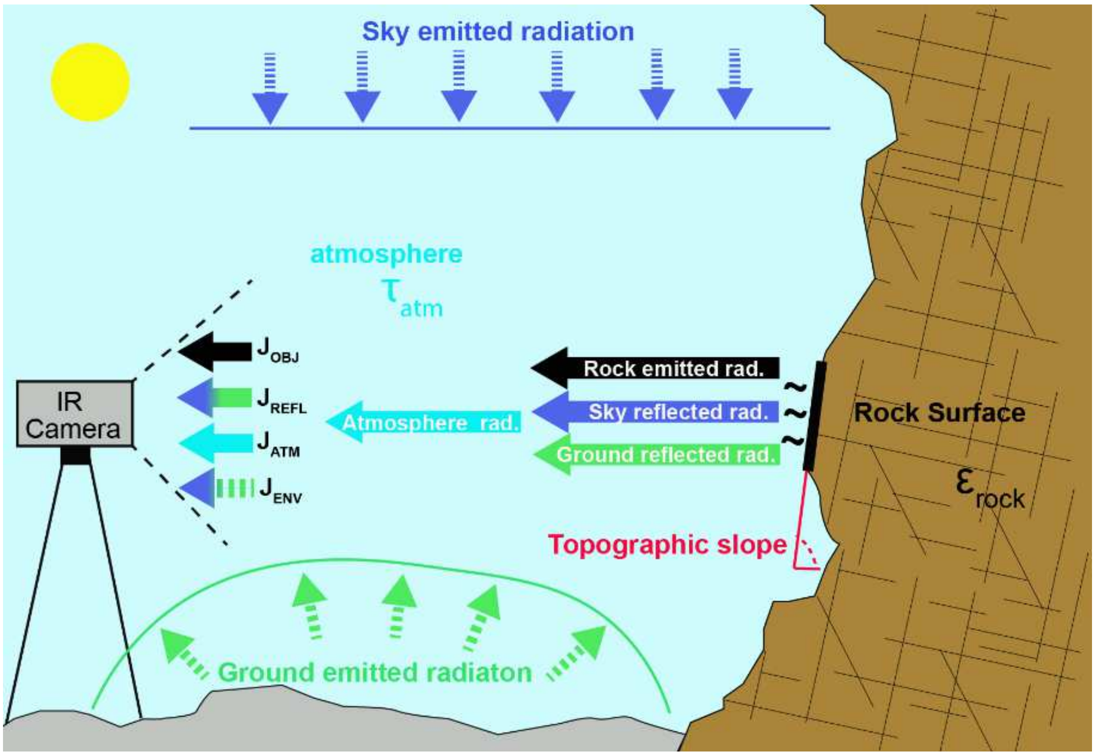

Figure 47 *Contributions of the temperature signal recorded by IRT in an outdoor setting. The rock emitted radiation (black arrow), the reflected Infrared radiation contribution of the sky (blue arrow) and the ground from the surface to the camera (green arrow) and the atmospheric radiation (light-blue arrow). These contributions must be removed to realistic measurements of the surface temperature of rock surface.* (Franzosi, Crippa, et al., 2023)

These contributions, summarized in **Figure 47** include the sources of the radiation that is reflected from the environment back to the sensor (FLIR, 2011; Franzosi et al., 2023b):

- direct solar radiation;
- radiation from the sky;

- radiation from other bodies in the environment besides the object (adjacent objects, ground, atmosphere etc.).

Solar radiations have much shorter wavelengths than those recorded by the thermal camera and then do not contribute directly to this budget. However, solar radiations contribute to heat the target (i.e. rock surface), which then emits thermal radiations in the range of those measured by the camera, the other two sources are usually detected by the camera and needs to be evaluated.

For each body with temperature greater than the thermal zero (0°K/-273°C), the radiation detected by thermal cameras is the sum of different contributions from the surrounding environment, that must be removed to provide real measurements of the surface temperature of target objects (**Figure 47**). Environmental contributions are particularly important when operating in outdoor environments, and the radiation measured by the camera can be resumed as;

$$J_{TOT} = J_{OBJ} + J_{REFL} + J_{ATM}$$

Equation 32

Where:

J_{TOT} is the total amount of radiation measured by IR camera (Wm^{-2})

J_{OBJ} is the radiation emitted by the body’s surface (Wm^{-2})

J_{REFL} is the environmental radiation (i.e sky/ground) reflected by the surface (Wm^{-2})

J_{ATM} is the radiation emitted by the atmosphere (Wm^{-2})

Expressing all these terms as a function of the kinetic temperature, according to FLIR (2011), the kinetic temperature of an object can be derived from the apparent temperature by means of the "measurement formula”, the variables of which account for all of the above contributions, and which will be discussed individually below;

$$T_{OBJ} = \left[\frac{T_{APP}^{4} - (1-\varepsilon)\tau T_{REFL}^{4} - (1-\tau)T_{ATM}^{4}}{\varepsilon\tau}\right]^{1/4}$$

Equation 33

Where:

T_{OBJ} is the target temperature(K)

T_{APP} is the apparent temperature recorded by the thermal camera (K)

T_{REFL} is the reflected temperature emitted by the environment (i.e sky/ground) (K)

T_{ATM} is the air temperature (K)

τ is the transmittance of atmosphere (-)

Emissivity

As anticipated earlier, emissivity is defined as the ability of a body to emit thermal radiation in the wavelength range of interest, and it is fundamental to the calibration of IRT temperatures. The emissivity of an object can be estimated experimentally through laboratory tests using either contact thermometers or targets of known emissivity with the same temperature, obtaining during IRT acquisitions both the measured and apparent temperature and allowing the emissivity parameter to be calculated by inverting **Equation 33**.

Emissivity thus turns out to be an intrinsic property of the material and can be considered constant, although it has been shown that there is also a directional influence of emissivity (Vollmer & Möllmann, 2018) as a function of the angle between the IR camera and the surface normal, which in some cases can be important in assessing the significance of measurements (**Figure 48**).

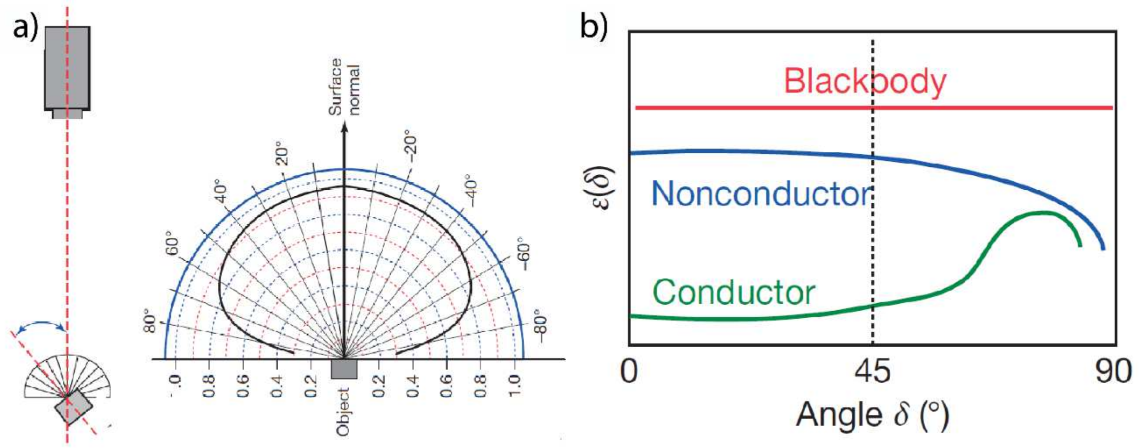

Figure 48 *Values of directional emissivity for different kinds of emitters* (Vollmer & Möllmann, 2018)

There are several standard reference tables for assigning emissivity value (Wolfe & Zissis, 1978; Salisbury & D'Aria, 1992), generally the lowest values are associated with metals that reach very low levels ($\varepsilon < 0.03$). Rocks generally (**Figure 49**) have emissivity above 0.9 (wavelength range 7-14 µm; Salisbury & D'Aria, 1992; Mineo & Pappalardo, 2021) with variability related to the degree of surface processing or alteration of the material.

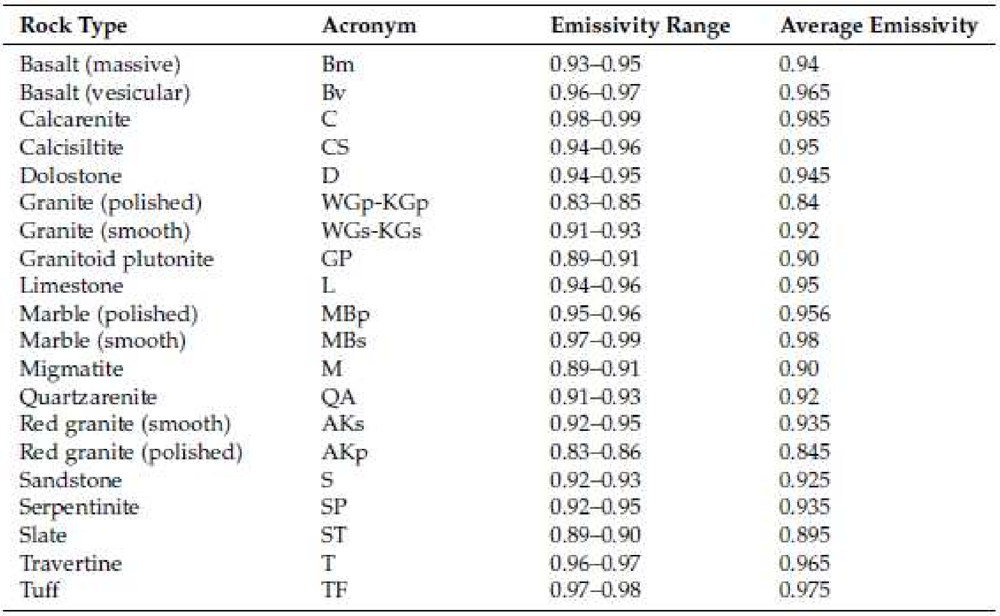

Rock Type	Acronym	Emissivity Range	Average Emissivity
Basalt (massive)	Bm	0.93–0.95	0.94
Basalt (vesicular)	Bv	0.96–0.97	0.965
Calcarenite	C	0.98–0.99	0.985
Calcisiltite	CS	0.94–0.96	0.95
Dolostone	D	0.94–0.95	0.945
Granite (polished)	WGp-KGp	0.83–0.85	0.84
Granite (smooth)	WGs-KGs	0.91–0.93	0.92
Granitoid plutonite	GP	0.89–0.91	0.90
Limestone	L	0.94–0.96	0.95
Marble (polished)	MBp	0.95–0.96	0.956
Marble (smooth)	MBs	0.97–0.99	0.98
Migmatite	M	0.89–0.91	0.90
Quartzarenite	QA	0.91–0.93	0.92
Red granite (smooth)	AKs	0.92–0.95	0.935
Red granite (polished)	AKp	0.83–0.86	0.845
Sandstone	S	0.92–0.93	0.925
Serpentinite	SP	0.92–0.95	0.935
Slate	ST	0.89–0.90	0.895
Travertine	T	0.96–0.97	0.965
Tuff	TF	0.97–0.98	0.975

Figure 49 *Typical emissivity values for different lithologies (Mineo & Pappalardo, 2021)*

Atmospheric transmittance

The Earth's atmosphere is composed of various gas and particles that can interact with Infrared radiation during an acquisition with IRT. These interactions include absorption, scattering and reflection of Infrared radiation. The transmissivity coefficient expresses the ability of the atmosphere to absorb part of the radiation in the path between the target and the IR camera taking into account all these combined effects (Vollmer & Mollmann, 2010).

The atmospheric transmissivity coefficient is usually expressed as a value between 0 and 1, where 0 indicates no transmission (all Infrared radiation is absorbed or scattered) and 1 indicates complete transmission (no attenuation of Infrared radiation). An atmospheric transmissivity value of 1 would indicate that all Infrared radiation passes through the atmosphere without any loss or attenuation.

For a given band of the IR spectrum field, the controlling factors are mainly;

- Air temperature
- Relative humidity of the air
- Distance between camera and target

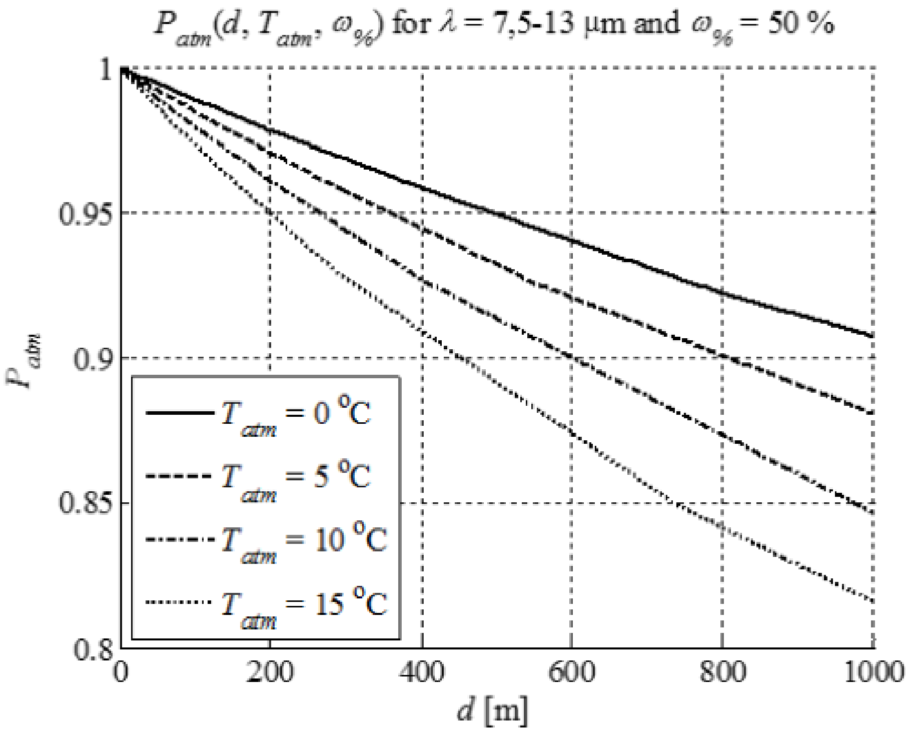

Figure 50 *Transmittance values for different distances and atmospheric conditions* (Minkina & Klecha, 2016)

There are several models that can describe the value of τ as a function of these parameters (Wiecek & De Mey, 2011; Minkina & Klecha, 2016) ; generally, it can be said that increasing temperature, distance, and relative humidity decrease the transmissivity of the environment even if they undergo a modest change in the LW range (7-14 µm) (**Figure 50**) for short acquisition distances and in common temperature ranges.

Reflected temperature

The object whose temperature is to be measured by IRT receives an amount of radiation from the surrounding environment (**Figure 47**) that is partially reflected towards the thermal imaging camera depending on its emissivity; this radiation is referred to as reflected temperature. To assess the reflected temperature in a scene it is generally sufficient to place a panel consisting of a highly reflective material on the target (e.g., aluminum, gold).

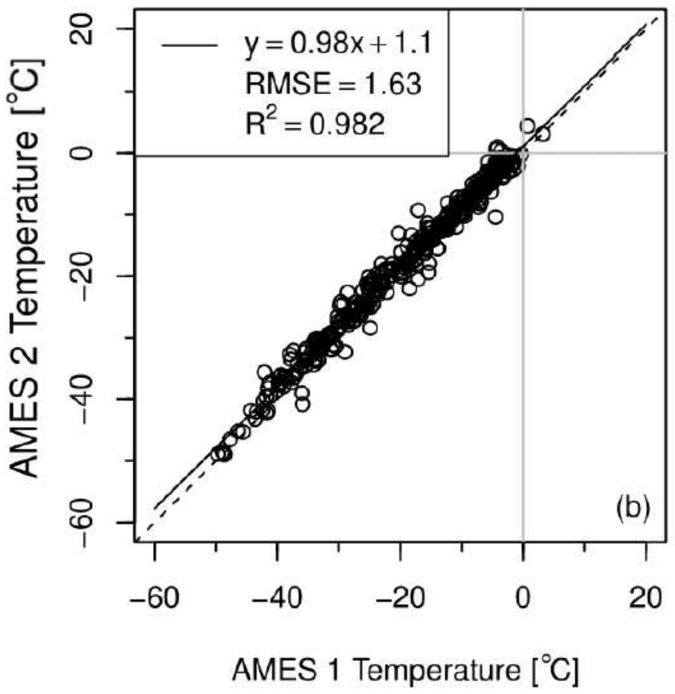

Figure 51 *Measured Sky IR-temperature with Infra-red thermometers for different atmospheric conditions* (Kelsey et al., 2022a)

Reflected temperature in laboratory environments generally tends to assume the value of the ambient temperature (reflects temperatures of objects in equilibrium with the ambient), unless heat or cooling sources are present at a temperature very different from that of the scene. In outdoor conditions, where significant amounts of energy radiated by the sky and surrounding ground are reflected by the target, T_{REFL} is mostly influenced by the radiation contribution of the cold sky, characterized by temperature values until -60°C in clear-days (**Figure 51**).

<u>*Directionality of Sky radiation*</u>

Sky radiation can be considered vertically diffused, but its contribution appears to be stronger in flat topography, resulting in cooler apparent temperature.

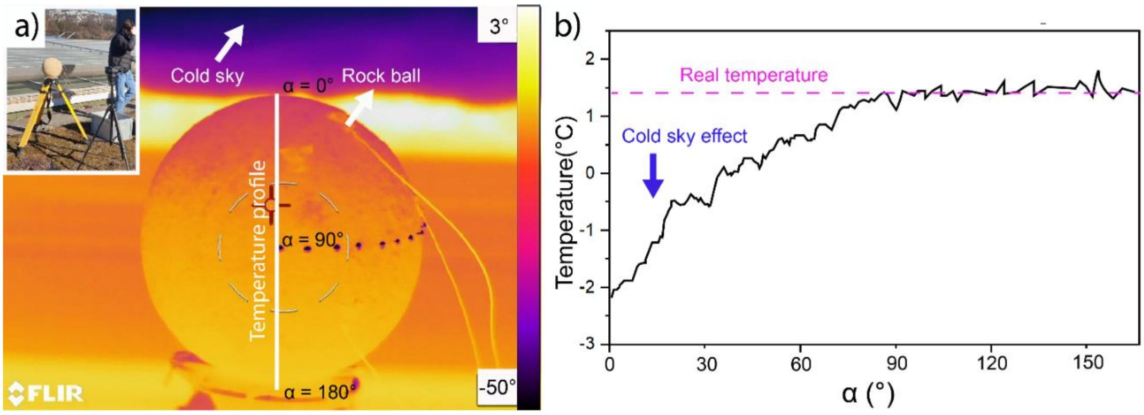

Figure 52 *a) RGB and IR images of the rock-ball exposed to outdoor conditions, b) effect of cold-sky on IR recorded temperature.*

This phenomenon is suggested by different authors (Spampinato et al., 2011; Guerin et al., 2019; Sass et al., n.d.) and simply demonstrated by the test performed with a ball made up of rock (limestone, $\varepsilon > 0.9$) leaved in outdoor during the night, in thermal equilibrium with the air temperature and captured with a LW IR-camera (**Figure 52**).The apparent temperature profile shows the influence of directional sky radiation (up to -60°), and lower measured apparent temperature as a function of the sphere curvature respect with to the zenith angle of the sky as showed in **Figure 52**, with differences up to 3°.

3.7.3 IRT applications in geological context: indoor vs. outdoor

Regarding the application of IRT for the purpose of monitoring the temperature of rock samples or natural rock outcrops, it is important to emphasize the differences that exist between a laboratory-scale and in situ measurement campaign. Observations on the control factors of IRT acquisitions suggest how they affect indoor and outdoor scenes differently.

Indoors, environmental conditions are controlled, so the T_{REFL} can be considered to tend to be homogeneous and the small distances between target and camera often make environmental corrections related to the transmissivity of the environment negligible. Outdoor acquisitions, on the other hand, may be more affected by the above controls, firstly because of the effects of the directionality of sky radiation combined with the complexity of the geometry of natural rock surfaces, and second because of the variability of environmental conditions and the distances that may be greater. In a laboratory context, the survey sample may be monolithological or contain lithological variations known to the operator that can be corrected by assigning different emissivity to the portions of the scene framed. Moving through outdoor measurements, the scale of the survey and the unfamiliarity of a rock outcrop can make this step complicated.

Therefore, it is important for the operator to evaluate all these aspects when approaching an IRT acquisition, and to set the goal of calibrating the thermograms by evaluating which factors are most likely to affect the measurements, how they vary in space and time, and especially whether they can be influential in the descriptions of the phenomena being investigated.

4 Laboratory-scale characterization of rock fracturing state

Starting from the theoretical conceptualization explained in **Chapter 2** and **Chapter 3**, we carried out a laboratory-scale experimental investigation aimed at verifying, under controlled conditions, that: a) the cooling rate of a volume of fractured rock depends on its fracturing state, intact block size and fracture heterogeneity; b) differences between the thermal responses to prescribed thermal perturbations of rocks with different fracturing states can be quantified using Infrared Thermography (IRT); c) significant quantitative relationships between the cooling behavior of fractured rocks and fracturing state can be established. The terms “laboratory scale” refers to the scale at which the fracture state of rock volumes can be quantified by taking into consideration a total characterization of the fracture network in 3D dimensions, estimating unbiased quantitative measurements. From a metric point of view, the usable reference is that of applicability of the techniques used (in our case Micro-CT), which limits the volume measurements to the order of cubic decimetres (i.e 10^{-5} to 10^{-2} m^3).

We used IRT to monitor the cooling behavior of pre-fractured cylindrical samples of crystalline rocks (gneiss and mica schist) with a known fracturing state, both in laboratory and outdoor environments. We interpreted our results within the sound theoretical framework explained in **Chapter 3**, in order to establish quantitative relationships between fracture intensity (and heterogeneity) and the thermal cooling behavior of fractured rocks, with the perspective to develop a physically based method for the contactless characterization of rock fracturing at laboratory scale.

The research summarized in this Chapter has been published in (Franzosi, et al., 2023a).

4.1 Materials

We studied samples made of two rock types, namely: gneiss (G, **Figure 54**) and mica schist (M, **Figure 54**). They are representative of contrasting mineral composition (quartz- vs. phyllosilicate-rich), strength and stiffness, and samples have a bulk rock composition that can be considered representative of upper crustal rocks (Rudnick & Gao, 2003; Agliardi et al., 2017). Both rock types have low intact-rock porosity (<1.5%), mostly related to disconnected microcracks at the boundaries and across quartz and phyllosilicate grains (Paterson & Wong, 2005). The composition, fabric and mechanical properties of the studied rock have been characterized in detailed by Agliardi et al. (2014, 2017). The studied rock samples were pre-fractured in uniaxial compression by Agliardi et al. (2014, 2017), who provided a detailed characterization of their fracture patterns, and show a wide range of fracturing degree, making them ideal for our study.

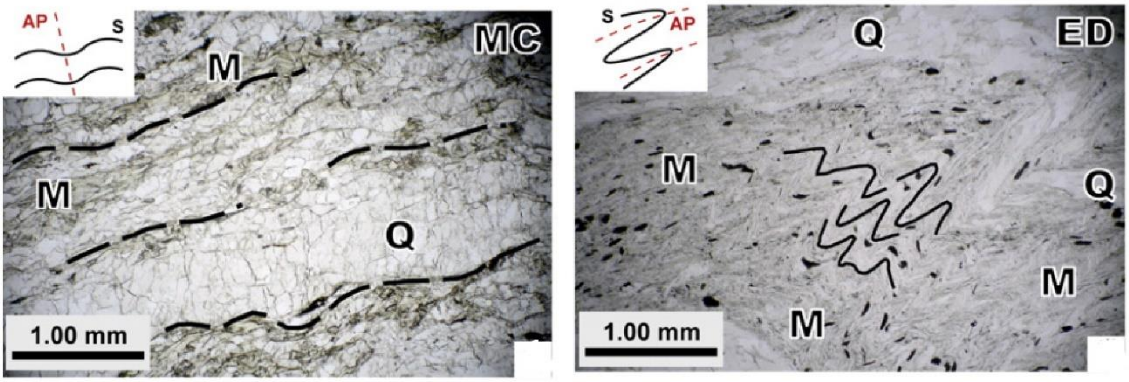

Figure 53 *Discrete foliation in Gneiss samples (left) and decrenulation in Mica schists (Agliardi et al., 2014).*

4.1.1 Gneiss samples (G)

We studied 7 cylindrical samples 78 mm in diameter (**Figure 54**). The rock, belonging to the Monte Canale tectono-metamorphic unit (Austroalpine Bernina nappe, Central Alps, Italy; (Trommsdorff et al., 2005), is an unaltered granodioritic gneiss, made of quartz (30–42 weight percent, wt%), feldspars (35–45 wt%), chlorite (5–13 wt%) and white mica (5–20 wt%) with a total phyllosilicate content less than 20% in weight Agliardi et al. (2014, 2017). The rock has a gneissic to protomylonitic fabric with a well-developed compositional layering made by alternating microlithons of quartz, plagioclase and K-feldspar (Q-domains), 2 to 5 mm thick, and mica-rich cleavage domains (M-domains) up to 1.5 mm thick. Quartz and plagioclase form more than 60–80% of the whole rock volume and occur as sub-equigranular aggregates within Q-domains **(Figure 53**). The main foliation is deformed by tight to gentle harmonic folds inherited from the tectono-metamorphic evolution of the rock, with sub-rounded or rounded hinges and variable wavelength (10 to 40 mm) and amplitude up to 35 mm (Agliardi et al., 2014). In unconfined compression, the studied gneiss exhibits a medium-low strength and an average Modulus Ratio according to the classification by (Deere & Miller, 1966). The rock is weaker than other crustal rocks with similar composition, due to the geometrical and mechanical controls of anisotropies associated to the folded fabric and exhibits a brittle to semi-brittle behavior in shallow crustal stress conditions, with complex failure modes including shear fracturing along foliation or along fold axial planes or the development of cm-scale localized brittle shear zones (Agliardi et al., 2014).

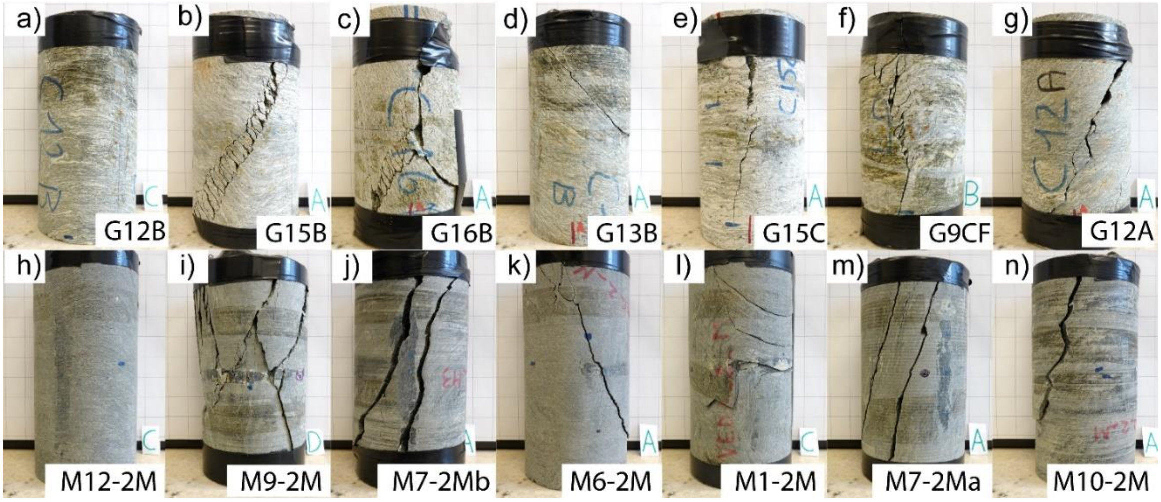

Figure 54 *Studied rock samples of gneiss (a-g; G set) and mica schist (h-n; M set). Both rock types exhibit complex fracture patterns constrained by phyllosilicate content and fabric* (Franzosi, Casiraghi, et al., 2023a).

4.1.2 Mica schist samples (M)

The sample set includes 7 cylindrical samples with a diameter of 83 mm (**Figure 54**). The rock belongs to the Edolo Schist Formation, forming most of the metamorphic basement of the central Southern Alps (Spalla et al., 1999), and it is an unaltered schist made of white mica (38–45 weight percent, wt%), quartz (25–40 w%), plagioclase (10–20 w%) and chlorite (10–15 w%), with minor amounts of garnet and rutile. The high phyllosilicate content (exceeding 50 w%) strongly controls rock fabric, that is characterized by a dominant foliation associated with the greenschist facies assemblages **(Figure 53**). The foliation is mostly continuous at mm-scale, marked by the shape preferred orientation of chlorite and white mica grains, and was formed by decrenulation of pre-existing foliations (Spalla et al., 1999; Agliardi et al., 2014). The foliation is deformed by tight to gentle crenulation folds with sub-angular to rounded hinges with wavelength between 10 and 70 mm and amplitude up to 50 mm (Agliardi et al., 2014). Unconfined compression tests revealed lower and less scattered strength characteristics with respect to the gneiss samples, with low to very low strength and high Modulus Ratio (Deere & Miller, 1966), implying a markedly brittle mechanical behavior (Agliardi et al., 2014). The rock exhibits fabric-controlled failure modes like those observed for gneiss samples but associated to the development of more spaced and long fractures.

4.2 Experimental methods

4.2.1 Fracture network quantification: Micro-CT

The studied samples were pre-fractured by Agliardi et al. (2014) in laboratory unconfined compression tests performed at constant displacement rate using a stiff, servo-controlled loading frame. Brittle failure of both rock types was accompanied by the macroscopic development of shear fractures along the main foliation (planar segments or fold limbs), as well as fractures that cut across the foliation and those that developed parallel to fold axial planes. Fractures formed along foliation or axial planes are generally planar, whereas fractures across foliation have a rough curved or stepped character. More complex failure patterns were also observed, involving the partial or complete development of brittle shear zones exploiting both the foliation and surfaces parallel to fold axial planes (Agliardi et al., 2014).

We used a high-resolution analytical approach, based on X-ray Computed Tomography (see **Chapter 2**), to obtain an unbiased quantification of the fracturing state of the selected rock samples. High-resolution X-Ray CT allows a non-destructive, detailed three-dimensional reconstruction of fracture networks in rock volumes at the laboratory sample scale (Keller, 1998; Montemagno & Pyrak-Nolte, 1999). The samples, pre-fractured in laboratory uniaxial compression tests, were scanned at a resolution of 625 μm using a GE D-600 medical CT scanner (Agliardi et al., 2014). Starting from these image stacks we performed a 3D reconstruction of each sample volume using the software AVIZO^{TM}. In these reconstructions, each voxel is attributed a grayscale value proportional to the local X-ray attenuation, with lowest values corresponding to voids (e.g. open fractures). We identified fracture domains by CT image segmentation using calibrated binary thresholds.

Then, for each sample we selected the fracture domains crossing sample external boundaries (i.e., directly exchanging heat with the outside). Finally, for each sample we quantified fracture surfaces and volumes (**Figure 55**) and, knowing each sample total volume, calculated the corresponding volumetric fracture intensity (P_{32}) and the fracture porosity ($P_{33;}$ **Table 2**) according to the definition of Dershowitz & Herda (1992). These descriptors are quantified by sampling fracture domains in a volume space; thus, they provide an unbiased description of fracture abundance (Mauldon et al., 2001; Rogers et al., 2017).

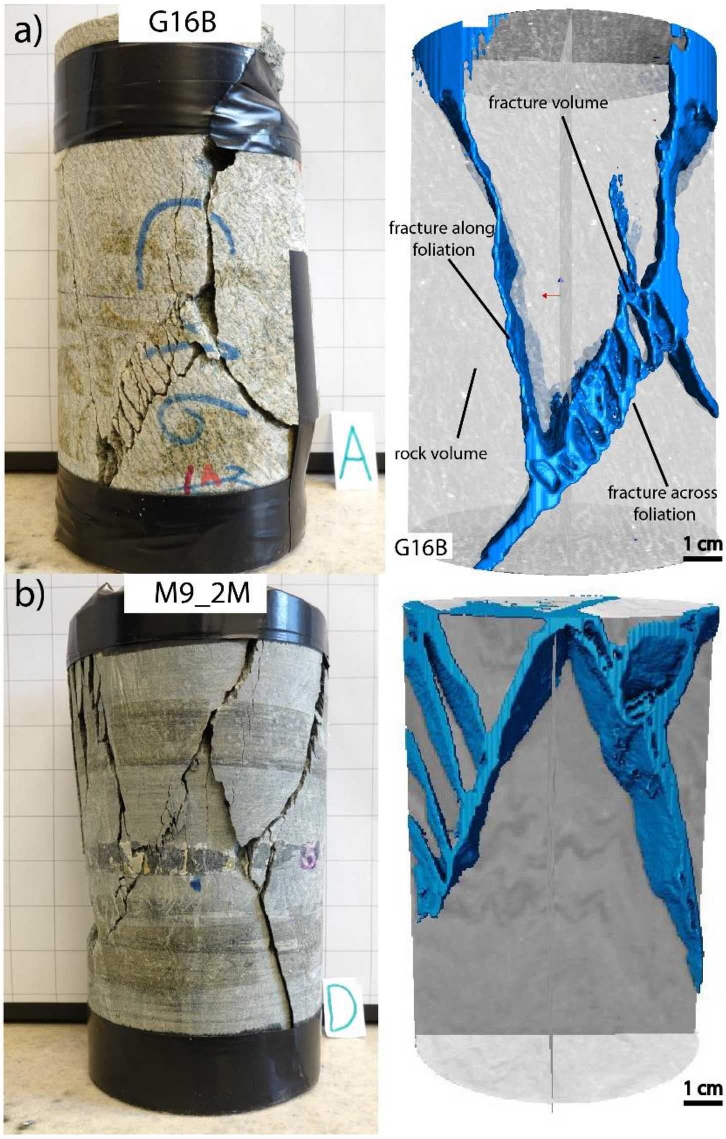

Figure 55 *Example of 3D fracture reconstruction for the sample G16B (Figure 54c) and M9_2M (Figure 54i), performed on the X-Ray CT image stack (voxel size: 625 µm) using Avizo ™ software. Fractures are portrayed as rendered solids. 3D reconstruction allowed an unbiased quantification of fracture abundance descriptors P32 (volumetric fracture intensity) and P33 (fracture porosity). Their values are summarized in Table 2 (after Franzosi et al., 2023a).*

Micro-CT image processing with AVIZO™

CT images were loaded within the software, which organizes them as a vertical package, reconstructing the acquisition geometry into a package of several slices (**Figure 56**).

Through the *Volume Edit* function, it is possible to manually construct a volume ROI that re-cuts the slice packet according to the geometry of interest (**Figure 56**), isolating the portions of the image useful for sample reconstruction (in this case cylindrical).

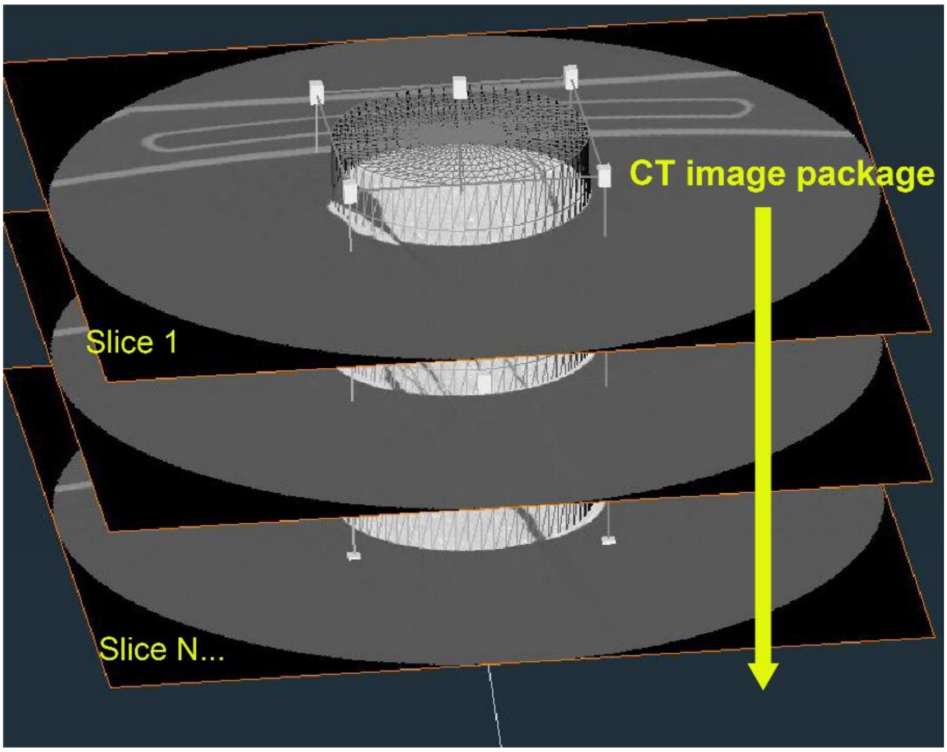

Figure 56 *CT images package visualization on AVIZO ™ with manually constructed ROI volume.*

At this point the *Interactive Tresholding* function of the images can be operated by selecting the most correct attenuation threshold that divides the pixels of each image into rock and void, generating a binarized slice stack (**Figure 57**).

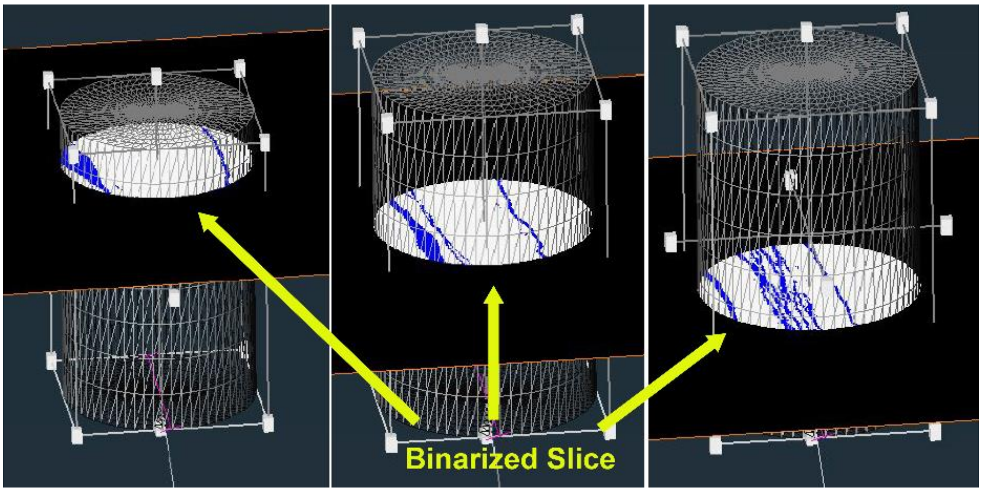

Figure 57 *Visualization of Interactive Thresholding tool, which isolates the voids as blue pixel before binarizing all slices (AVIZO ™)*

Through the *Label Analysis* function, a stacking of the binarized CT images is performed and the 3D geometry of the voids is reconstructed, on which the 3D volume and total area of the fracture network (**Figure 58**) can be automatically evaluated.

Finally, through the *Border Kill* function, all fracturing volumes that do not intersect the edges of the volume ROI, and therefore do not communicate with the outside of the sample, can be identified by selecting them and excluding them from the analysis (**Figure 58**).

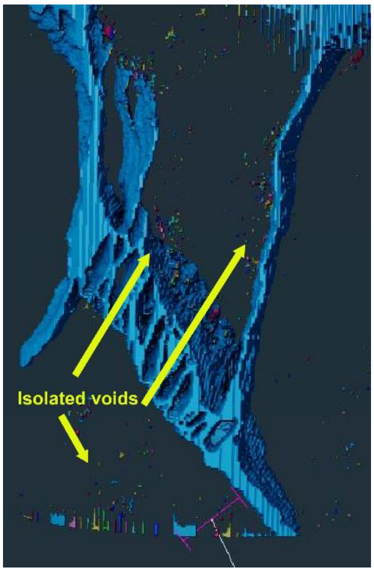

Figure 58 *Visualization of 3D fracture network reconstructed were the voids that are not connected with the eternal boundaries are indicated (AVIZO ™)*

4.2.2 Laboratory cooling experiments

We performed a series of experiments to monitor the thermal response of Gneiss and Mica shist rock samples, characterized by different fracturing states, to forced heating and subsequent cooling, both in a controlled laboratory environment and outdoor, using Infrared Thermography (**Chapter 3**). Laboratory experiments (**Figure 59**) were performed on all the available gneiss (G) and mica schist (M) samples, with the aim to finding relationships between their fracturing states and cooling dynamics under specifically designed controlled conditions. An outdoor experiment (**Figure 59d**) was also carried out on G samples to verify that these relationships can be detected also in uncontrolled environmental conditions, where heating is related to natural solar forcing.

We performed two series of cooling experiments, namely: a) laboratory experiments in controlled environmental conditions under forced heating; b) an additional outdoor experiment in natural conditions, where samples were heated by solar radiation in a diurnal cycle.

For both laboratory and outdoor experiments, we monitored the temperature of samples over time using a FLIR T1020 high-resolution thermal camera (1024 x 768 pixels), characterized by a measurement sensitivity within 0.02 C° and a field of view (FOV) of 28° x 21° (**Figure 59a**). For all the experiments, the camera was mounted on a tripod located 1-2 m from the samples.

To perform cooling experiments in controlled conditions, we prepared an original laboratory setup (**Figure 59a**) hosting up to three well-spaced samples for each experiment, with a high-emissivity neoprene background (emissivity $\varepsilon \sim 1$) to avoid disturbances around the sample due to reflected thermal radiation components. For each experiment, ambient temperature (i.e., the lower temperature boundary condition for cooling) and humidity were kept constant (20°C and 33%, respectively), and monitored by a thermo-hygro data logger. A rough gold panel was placed in the scene to allow the measurement of reflected thermal radiation components (**Figure 59a**). All the gneiss (G) and mica schist (M) samples were heated in a laboratory oven (to ensure a long and smooth cooling curve) until reaching a homogeneous temperature of 80°C, then placed on the set. The heating temperatures of the samples were chosen based on previous experiences on the subject (Mineo & Pappalardo, 2016), to embrace the temperature ranges usually encountered in natural field conditions and emphasize the cooling rates of different samples.

Sample temperature during cooling was monitored by capturing thermograms every 2 minutes in *time-lapse* mode (**Figure 59b**); each indoor tests lasted approximately 1 hour and 45 minutes. For each sample, experiments were repeated with the same initial and boundary conditions to monitor the cooling of samples from four perpendicular directions (**Figure 59c**). This allowed covering the entire sample surface and capturing the effects of fracture heterogeneity on the bulk thermal behavior of studied fractured rocks.

For outdoor experiments we used a similar setup without the neoprene background, to allow samples heating under natural solar forcing over a day (**Figure 59d**). Based on the results of the cooling experiments performed in the laboratory, for outdoor experiments we decided to focus on gneiss samples (G), that showed the clearest signals. Samples were arranged in a N-S trending row, exposed to solar radiation from the early morning until sunset of a cloud-free day of May, and then let cool for 14 hours (**Figure 59d**). In this experiment, thermograms were captured every 15 minutes in *time-lapse*.

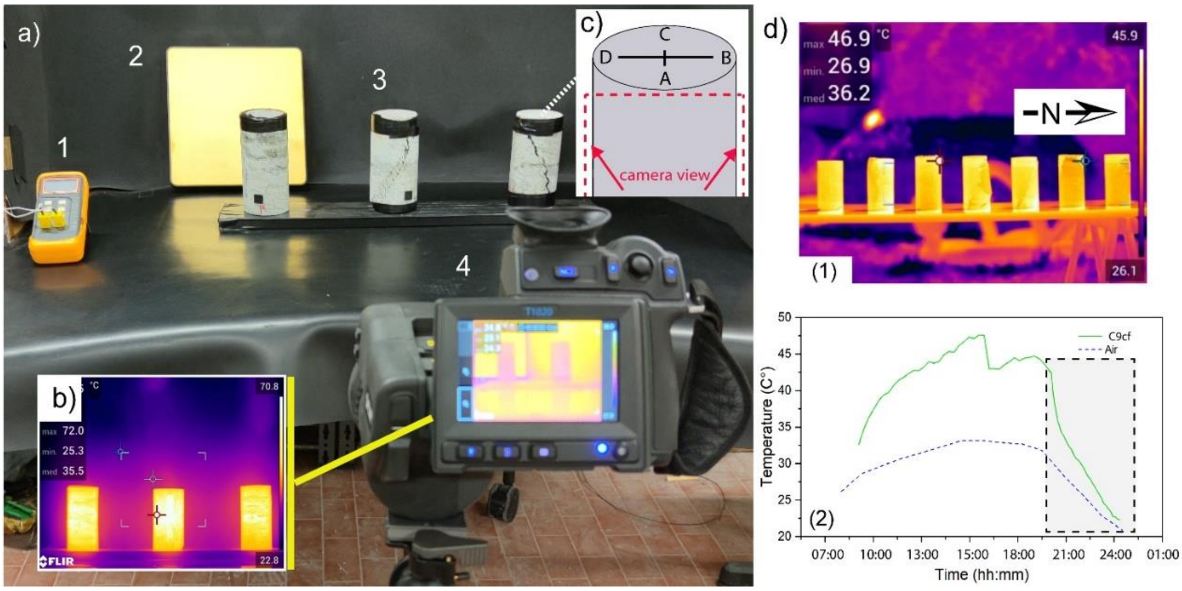

Figure 59 *Cooling experiment setup. a) indoor setup, including a thermo-hygrometer to monitor air conditions (1), a rough gold panel to quantify reflected thermal radiation (2), a neoprene background (3), and a FLIR T1020 high-resolution IRT camera to monitor sample temperature (4). b) example of raw thermal image acquired during cooling experiments, that were repeated looking each sample from four perpendicular viewpoints (c). Outdoor experiments were performed on gneiss samples using a*

similar setup (without neoprene background) under natural solar forcing. Shaded area refers to the cooling stage (d) (Franzosi et al., 2023a)

4.3 Experimental data analysis

4.3.1 Thermal image processing

We imported the acquired thermal images into the software FLIR ResearchIR Max^{TM} and set all the relevant corrections constant for the entire duration of each experiment (i.e., sample-camera distance, air temperature and humidity, reflected temperature, sample rock emissivity). Both the studied rock types, that represent similar mixtures of similar mineral species (chiefly quartz, mica and feldspars) are characterized by high broadband emissivity (ε>0.95) with values scattered over similar ranges (Salisbury & D'Aria, 1992; Mineo & Pappalardo, 2021).

We first inspected the thermal images (**Figure 60**) to check the quality of the acquired data (absence of noise ambient/disturbances, border effects related to the sample shape, etc.). Visual inspection also provided key evidence to support the quantitative interpretation of temperature distributions and temperature time histories, accounting for the influence of individual fractures (**Figure 60**), their aperture (**Figure 60**) and spatial distribution on the overall cooling behavior of each sample.

For each sample, we extracted populations of temperature values from the images of the four considered sectors (**Figure 59**c) using Regions-of-Interest (ROI). ROIs were selected to cover the sample surfaces excluding the external borders, where the signal was affected by edge curvature effects. We evaluated the statistical distributions of temperature in space and time using an original MATLAB^{TM} tool, that is also able to perform a peak analysis using a Kernel distribution fitting, that automatically identify the number of frequency peaks and their maximum separation (MPD, Maximum Peak Distance, i.e., the distance between the highest and the lowest peak) in temperature distributions.

Temperature values extracted for each sample ROI at different time were averaged to obtain cooling curves representative of the bulk sample. We further processed these time histories to compute cooling rates in the form of the Cooling Rate Index (CRI, see **Chapter 2;** Mineo & Pappalardo, 2016). Since computing the CRI for different time intervals may hamper a significant comparison between different samples with non-synchronized cooling histories, we computed the CRI for different temperature intervals through an using original

MATLAB^{TM} script. For example, the code CRI_{6070} corresponds to the CRI (in C°/min) related to the cooling curve portion between 70°C and 60°C.

Finally, we parametrized the lumped capacitance equation (**Equation 12**) on our experimental data, to provide a description of the cooling curves in terms of its exponent, here referred to as Curve Shape Parameter (C_{SP}, **Equation 13**).

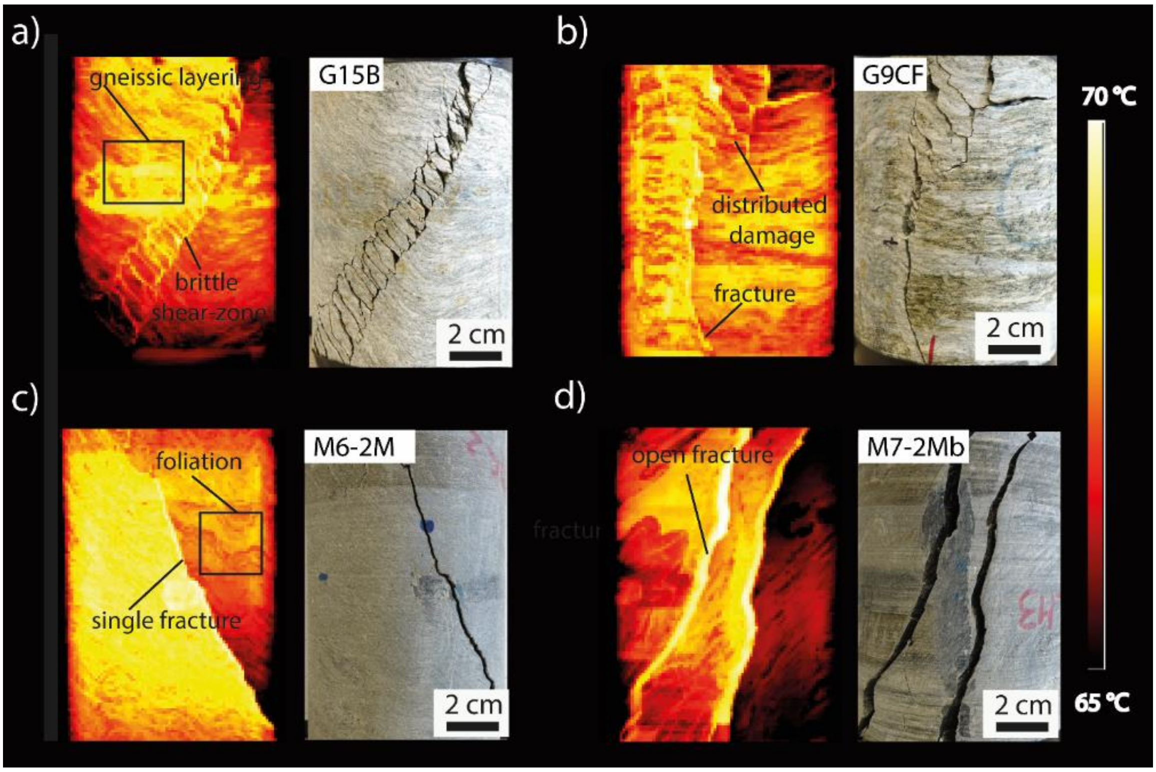

Figure 60 *Thermal images of selected samples in early cooling stages, showing different thermal responses associated to different fabric characteristics (a,b: gneissic layering; c,d: continuous foliation), damage patterns (a: brittle shear zones; b: distributed damage; c,d: discrete fracturing), and fracture opening (Franzosi et al., 2023a)*

4.3.2 Statistical correlation analysis

We investigated possible relationships among cooling dynamics descriptors (i.e., CRI, C_{SP}) and fracture abundance measures (P_{32}, P_{33}) by performing statistical regression analysis of the experimental data. We evaluated the suitability of different regression models (linear and non-linear) by analysing residuals to check for independence of the error terms and absence of process drifts.

We applied non-parametric statistics in terms of Spearman's rank correlation coefficient, ρ (Spearman, 1961; Zar, 2005) to evaluate the occurrence and strength of statistical relationships among variables, independently on data normality and linearity of regression models (Swan & Sandilands, 1995). We also quantified the goodness of fit in terms of adjusted coefficient of determination (R^2) and parametric Pearson's correlation coefficient, r.

4.3.3 3D Finite-Element modelling

Finite element methods are now widely used to solve structural, fluid, and Multiphysics problems numerically (Zienkiewicz, 1975; Kang et al., 1996; Bathe, 2007). Partitioning into finite elements is critical because it allows the partial differential equations that describe the physical behavior of an object or structure to be solved. The "mesh" is the geometry by which the domain is subdivided into smaller elements, such as triangles or squares in 2D or tetrahedrons, pyramids or hexagons in 3D or even hybrid geometric shapes (Ho-Le, 1988).

We investigated the physical processes underlying the observed cooling behavior of selected samples using 3D Finite-Element numerical modeling, to support the interpretation of the empirical relationships between cooling dynamics and rock fracturing state. We ran 3D, continuum-based, non-linear FEM simulations of heat transfer using the code MIDAS GTS-NX^{TM}. We generated solid models with regions with properties typical of air (**Figure 61**; **Table 1**), that mimic the fracture geometry, size and aperture of three real gneiss samples, plus a reference intact gneiss sample. The analysis domains were discretized into FEM 3D meshes consisting of hybrid finite elements with size from 4.6 mm to 2.6 mm depending on the model and related fracture pattern.

Table 1 *Summary of the thermal material properties for 3D FEM modeling.*

		Material		**Air-Rock Interface**	
Parameter	**Symbol**	**Rock**	**Air**	**External boundary**	**Internal fracture**
Thermal conductivity	κ $(Wm^{-1}\ K^{-1})$	3.5	0.025	-	-

Specific heat capacity	C_p $(JKg^{-1} K^{-1})$	820	1000	-	-
Convection coefficent	h $(Wm^{-2} K^{-1})$	-	-	6.6	2.2

Model thermal boundary conditions were set to reproduce the laboratory cooling experiments. Heat transfer simulations were conducted using a transient model accounting for both heat diffusion (in solids) and convection (at solid-fluid interfaces, i.e., at sample boundary and within open fractures) (see **Chapter 3**). Typical literature values of the thermal properties like thermal conductivity k $(Wm^{-1}K^{-1})$ and specific heat capacity C_p $(JKg^{-1}K^{-1})$ were adopted and kept constant for the gneiss material and the air (**Table 1**; Clauser & Huenges, 1995; Barreira & de Freitas, 2007). Different values of the convection coefficient h $(Wm^{-2}K^{-1})$ were applied at the solid-air interface outside the sample and inside fractures (**Table 1**).

We performed numerical simulations in different steps, namely: a) steady-state heating, to make every element of the model reach the same starting temperature of 80°C (**Figure 61c**) reproducing the oven heating in the lab; b) transient-cooling, as a time step analysis to simulate the laboratory cooling phase down to 20°C (room temperature). We extracted model results as mean of nodal values of T on the entire model surface for each solution step with a temporal sampling of 1 minute, then averaged to extract overall simulated sample cooling curves, using the same methodology applied to the characterization of the cooling histories of the samples, record with the IRT camera.

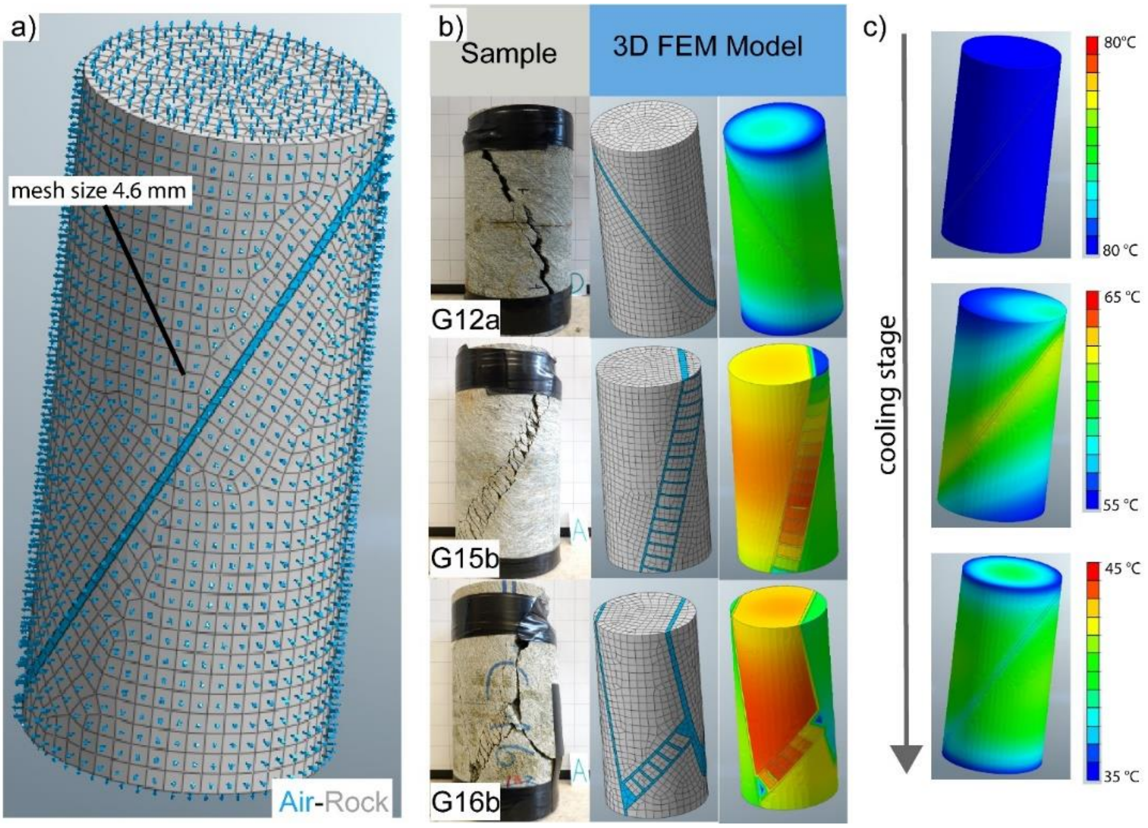

Figure 61 *3D Finite-Element model setup. a) 3D reproduction of fractured rock samples as solid models with fractured regions. The analysis domains were discretized into 3D meshes of hybrid finite elements with size variable between 2.6 and 4.6 mm; b) model geometry for three selected real rock samples and their thermal responses halfway during cooling; c) example of simulated time-dependent evolution of temperature (sample G12a) (Franzosi et al.2023a).*

4.4 Results

4.4.1 Fracture patterns and thermal response

Thermal images, acquired at different cooling stages in laboratory experiments, clearly show the influence of fracture orientation, size, aperture, and intensity, typical of the two rock types, on the overall thermal response monitored by the thermal camera (**Figure 60**).

In fact, the complexity of the folded fabrics resulted in complex brittle failure mechanisms and strongly heterogeneous fracture networks (Agliardi et al., 2014). Moreover, unconfined conditions allowed dilatancy to occur during the laboratory fracturing process, forming fractures up to few millimetres open and leading to the development of significant fracture porosity. In the quartz-rich gneiss samples (**Figure 54 a-g,Figure 60, Figure 62**), failure across foliation or along fold axial planes involved the development of dense networks of microscopic cracks within quartz grain aggregates (Agliardi et al., 2014,2017), resulting in a more complex and distributed fracture damage patterns than in mica schist (**Figure 54 h-n,Figure 61, Figure 63**).

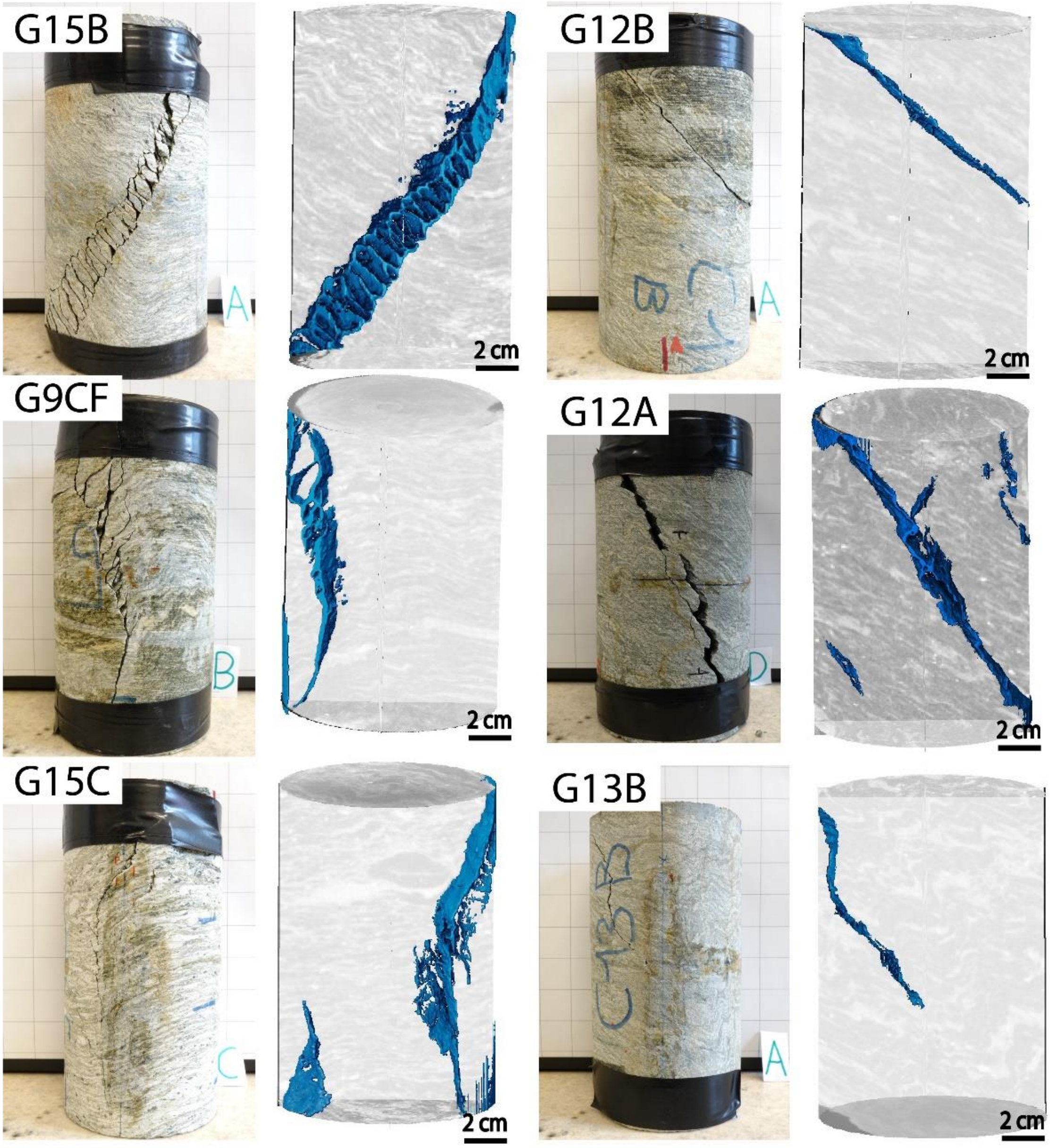

Figure 62 *CT-volume reconstruction for remaining Gneiss samples*

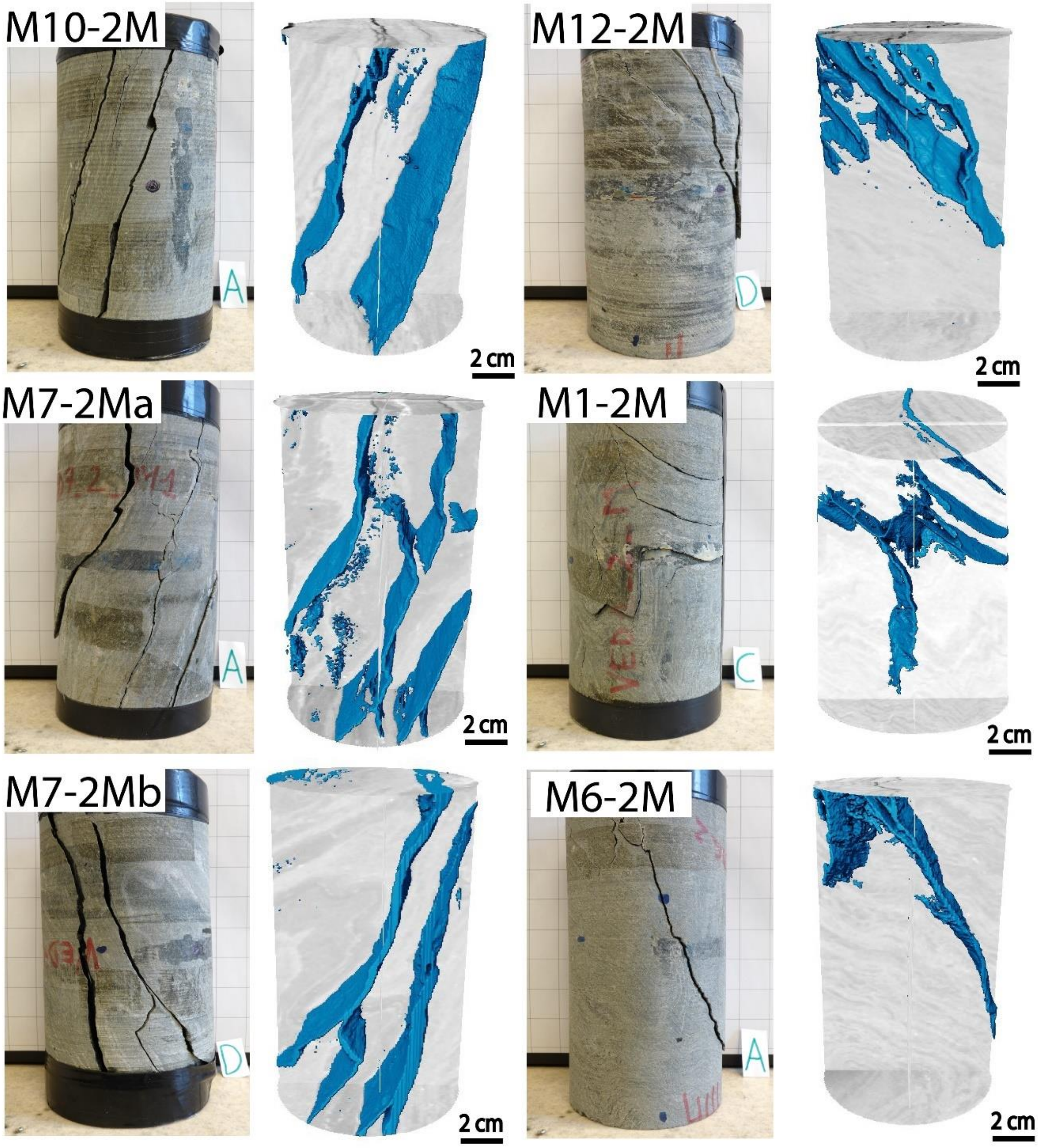

Figure 63 *CT-volume reconstruction for remaining Micaschist samples*

Table 2 *Values of fracture abundance indices (volumetric fracture intensity, P_{32}; fracture porosity, P_{33}) quantified using X-Ray CT for the studies samples.*

Sample	**P33** *(-)*	**P32** *(1/mm)*
G9CF	0.042	0.044
G12A	0.033	0.039
G12B	0.011	0.020
G13B	0.013	0.021
G15C	0.033	0.036
G16B	0.103	0.066
G15B	0.063	0.059
M6-2M	0.034	0.031
M7-2Mb	0.128	0.048
M10-2M	0.052	0.036
M7-2Ma	0.054	0.050
M12-2M	0.036	0.031
M9-2M	0.092	0.052
M1-2	0.033	0.035
M11-2M	0.042	0.025

The complexity of rock fracture patterns is mirrored by clearly different patterns in the thermal behavior of different rock types during cooling (**Figure 60**). Gneiss samples, characterized by heterogenous networks of short fractures along and across foliation and by distributed damage along cm-wide brittle shear zones, show a rather "continuous" thermal behavior (**Figure 60 a,b**). For this rock type we observed the expected good linear correlation between fracture porosity, P_{33}, and the volumetric fracture density, P_{32}

(Dershowitz & Herda, 1992; Rogers et al., 2017), with P_{33} scaling with the abundance of fractures that underwent dilatancy during brittle failure (**Table 2, Figure 64 a**).

On the other hand, mica schist samples are characterized by generally higher fracture porosity associated to spaced, persistent fractures with a wide range of aperture, and show a more "discontinuous" thermal behavior than observed in gneiss samples (**Figure 60 c,d**). In these samples, the linear correlation between P_{32} and P_{33} is weaker (**Table 2**, **Figure 64 b**), suggesting a more variable fracture opening of fractures transecting entire sample volumes. This suggests that adopted fracture abundance measures provide a less effective description of the fracturing state of "blocky" fractured media.

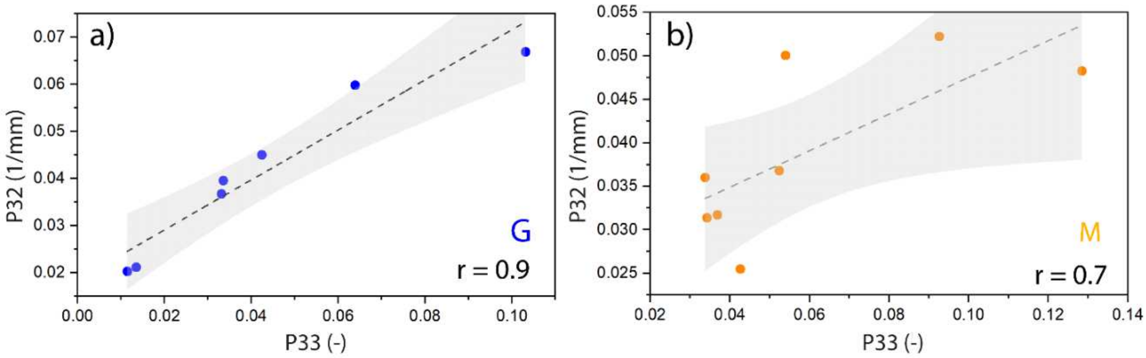

Figure 64 *Correlations between unbiased fracture abundance indices (P32 and P33) for the gneiss (a) and mica schist (b) sample set, also resumed in Table 2. Dashed lines: best fitting linear models. Shaded areas: regression prediction bands (95% probability). r: Pearson correlation coefficient. (Franzosi et al., 2023a).*

4.4.2 Temperature distributions during cooling

Samples characterized by different fracture patterns show different evolutions of their thermal states in different stages of cooling. These are captured by looking at the statistical distributions of temperature values sampled from each pixel in the thermograms ROIs at different times.

As showed in **Figure 65**, at the beginning of the cooling process (i.e. samples just removed from the oven) samples tend to exhibit a unimodal temperature distribution with variance depending on rock fabric (**Figure 65 a,c**). When persistent open fractures filled by air are present, they are always hotter than rock and result in additional peaks with low MPD (mean peak distance; **Figure 65 b,d**). As the cooling process continues, different temperature distributions can be observed. Rock samples characterized by low to moderate fracturing degree and distributed damage patterns tend to keep on behaving as "thermal continua", with unimodal temperature distributions or few peaks with very low MPD (**Figure 65 a,c**). On the opposite, samples with high or heterogeneous fracturing behave as "thermal discontinua", with multimodal temperature distributions characterized by several, well-separated peaks that testify to the occurrence of independent radiant elements (i.e. rock blocks) separated by persistent fractures (**Figure 65 b,d**). On the long term, the overall thermal states of the samples tend to equilibrate with the surrounding environment.

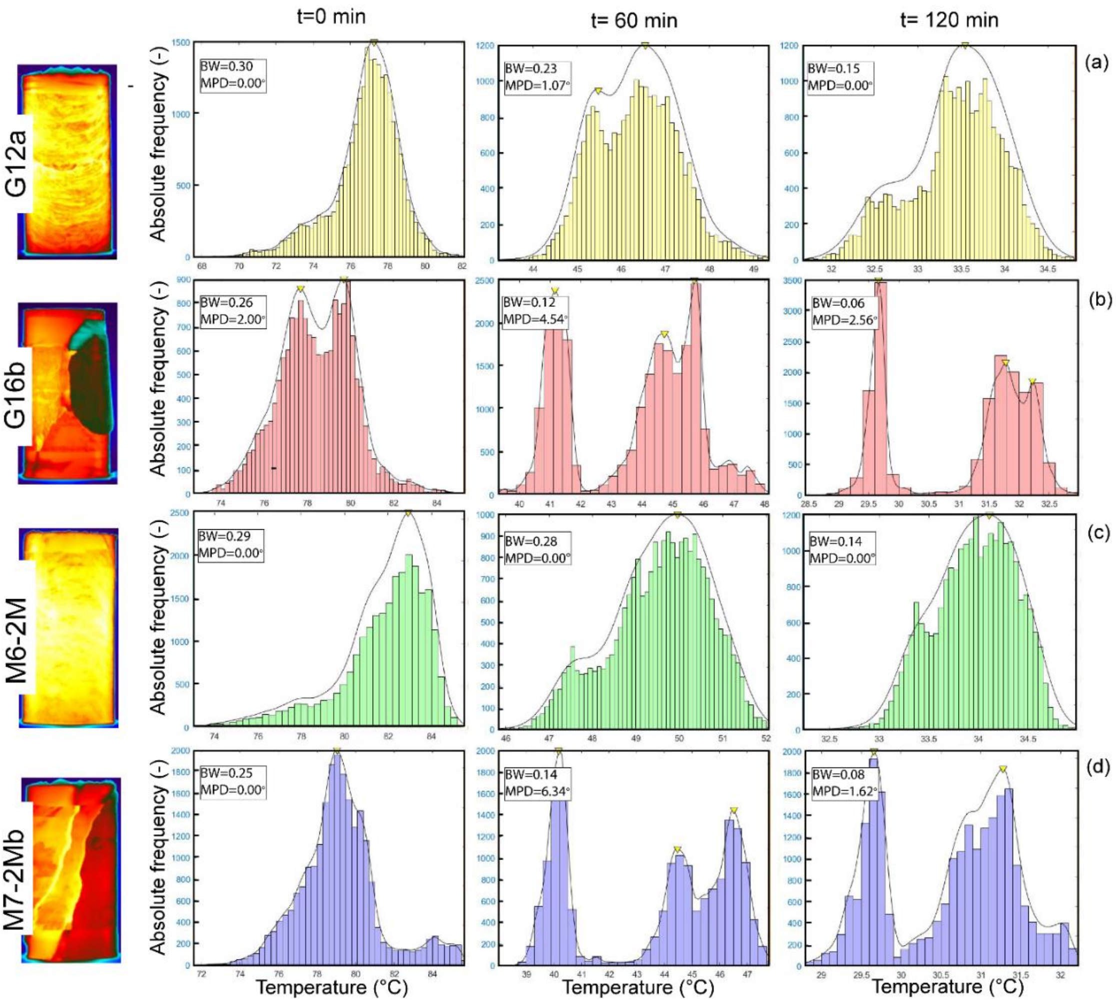

Figure 65 *Temperature distributions in different cooling stages for selected samples. Distributions were approximated using a Kernel density function with a selected bandwidth (BW) to outline frequency peaks (yellow triangles) and calculate their Maximum Peak Distance (MPD) (Franzosi et al., 2023a).*

4.4.3 *Cooling dynamics and its physical controls*

Laboratory cooling experiments show that samples with different fracturing states are characterized by different cooling curves (**Figure 66 a**), that have a negative exponential form according to the Newton’s law of cooling (Vollmer, 2009). In particular, values of the Cooling Rate Index, computed for different temperature intervals (i.e. 70-60°C, 70-50°C, 70-40°C, 70-30°C), always show a significant linear correlation with both fracture porosity, P_{33}, and volumetric fracture intensity, P_{32} (**Figure 66 b,c**; statistics in **Table 3**).

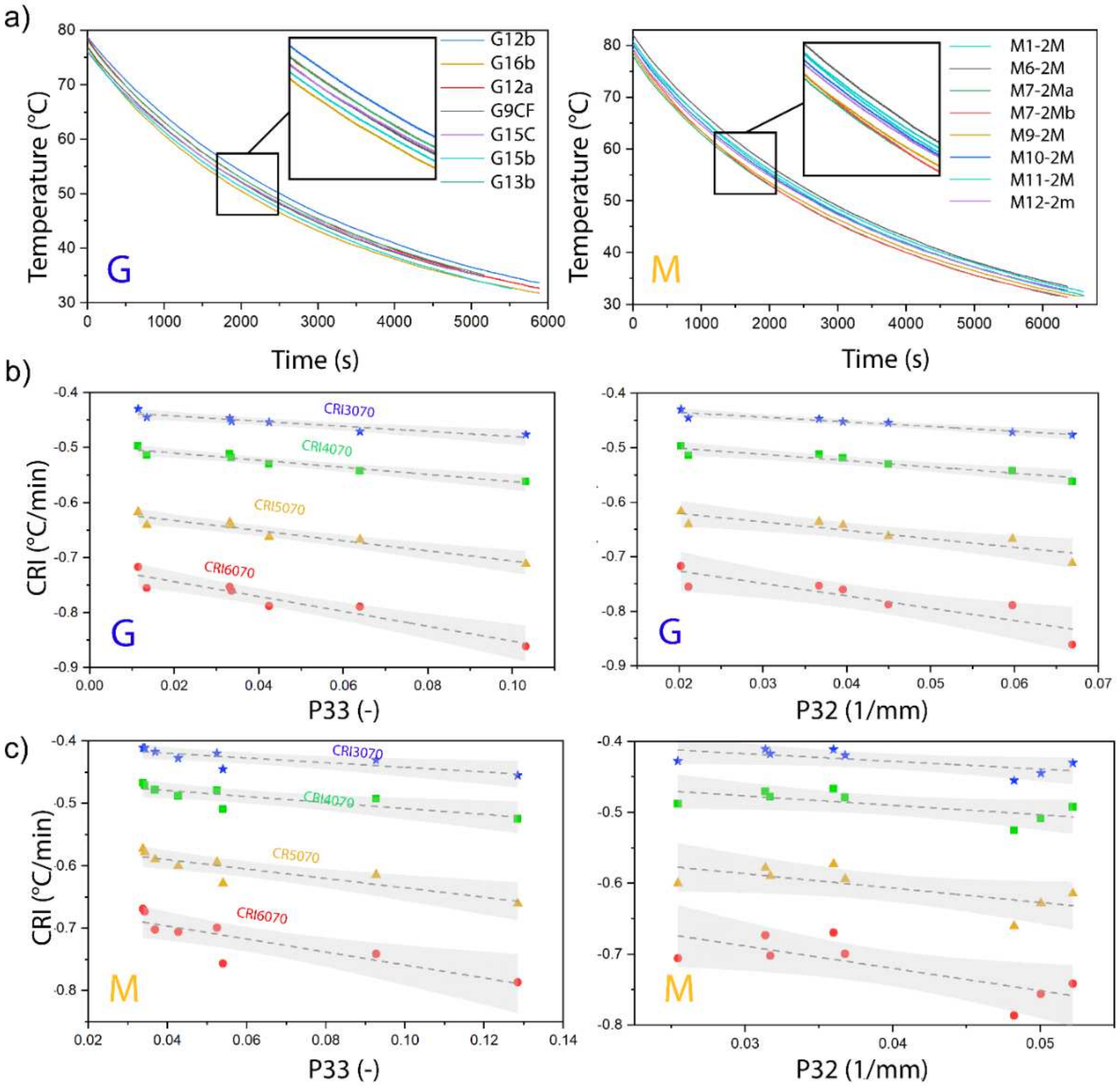

Figure 66 *Relationships between cooling dynamics and fracturing for the studied sample population. (a) Experimental cooling curves for gneiss (G) and mica schists (M) samples; (b-c) empirical correlations between the Cooling Rate Index, quantified for various temperature ranges, and the fracture abundance indices (P33, P32) for gneiss (b) and for mica schists (c). Dashed lines: best fitting linear models (Table 3). Shaded*

areas: regression prediction bands (95% probability) (Franzosi et al., 2023a).

Such correlation, that is stronger in early cooling stages, shows that more fractured rocks cool faster (Mineo & Pappalardo, 2016, 2019; Pappalardo et al., 2016; Mineo et al., 2022). Linear correlations are stronger for gneiss samples than for mica schist (**Table 3**). These results suggest that both P_{33} and P_{32} can be well discriminated at the accuracy level of the Infrared camera during the cooling stage.

Table 3 *Correlation goodness-of-fit statistics for laboratory data in Fig. 8. R^2: coefficient of determination; r: Pearson correlation coefficient (parametric); ρ: Spearman correlation coefficient (non-parametric). G: gneiss samples; M: mica schist samples.*

Variables	Dataset	R^2	r	ρ
(G) CRI-P_{33}	CRI6070	0.91	-0.95	-0.96*
	CRI5070	0.91	-0.95	-0.96*
	CRI4070	0.91	-0.95	-0.96*
	CRI3570	0.86	-0.92	-0.96*
(G) CRI-P_{32}	CRI6070	0.78	-0.88	-0.96*
	CRI5070	0.80	-0.89	-0.96*
	CRI4070	0.88	-0.94	-0.96*
	CRI3570	0.91	-0.95	-0.96*
(M) CRI-P_{33}	CRI6070	0.73	-0.85	-0.90*
	CRI5070	0.77	-0.88	-0.95*
	CRI4070	0.67	-0.81	-0.95*
	CRI3570	0.63	-0.79	-0.92*
(M) CRI-P_{32}	CRI6070	0.58	-0.76	-0.54
	CRI5070	0.48	-0.76	-0.59
	CRI4070	0.44	-0.66	-0.59
	CRI3570	0.45	-0.67	-0.64
(*) Spearman correlation is significant at 0.05				

Observed relationships also emerge in uncontrolled outdoor conditions (**Figure 67**).

In this case, the statistical correlation between the CRI values (computed over the range 40-35°C) is weaker than those obtained in the laboratory, due to the experimental noise related to the small temperature differences and the environmental conditions (i.e. limited solar forcing during Spring, episodic change of the environmental temperature due to cloud passage or air circulation; **Figure 59d**). These factors must be carefully considered when attempting to apply our experimental approach *in situ*, yet experimental results show its potential.

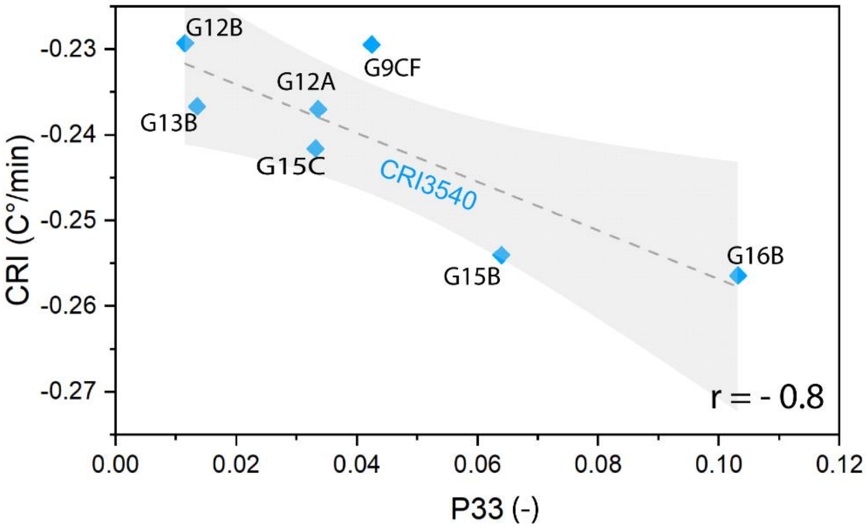

Figure 67 *Correlation between the Cooling Rate Index, computed in the temperature interval 40-35° and the fracture porosity (P33) of gneiss samples during outdoor cooling experiment. Dashed lines: best fitting linear model. Shaded areas: regression prediction bands (95% probability); r: Pearson correlation coefficient. (Franzosi et al., 2023a).*

The results of 3D FEM simulations performed for selected samples (**Figure 61**), processed to compute the same CRI descriptors used in laboratory experiments, provide interesting insights in the physical factors that control the cooling of fractured media. **Figure 68** clearly shows that numerical modelling results reproduce very well the experimental ones, within the prediction intervals of statistical regression. This match has been obtained using constant thermal properties for the solid rock material (**Table 1**), while the parameter controlling convective heat transfer at solid-air interfaces (i.e. external sample boundaries and open fracture surfaces) have been tuned by calibration (**Table 1**). In fact, while the realistic reconstruction of the geometry of radiant elements (i.e., sample structure) was enough to guarantee a correct simulation of diffusive heat transfer, the convective parameter needed to be adapted to the different persistence and aperture of fractures in different samples.

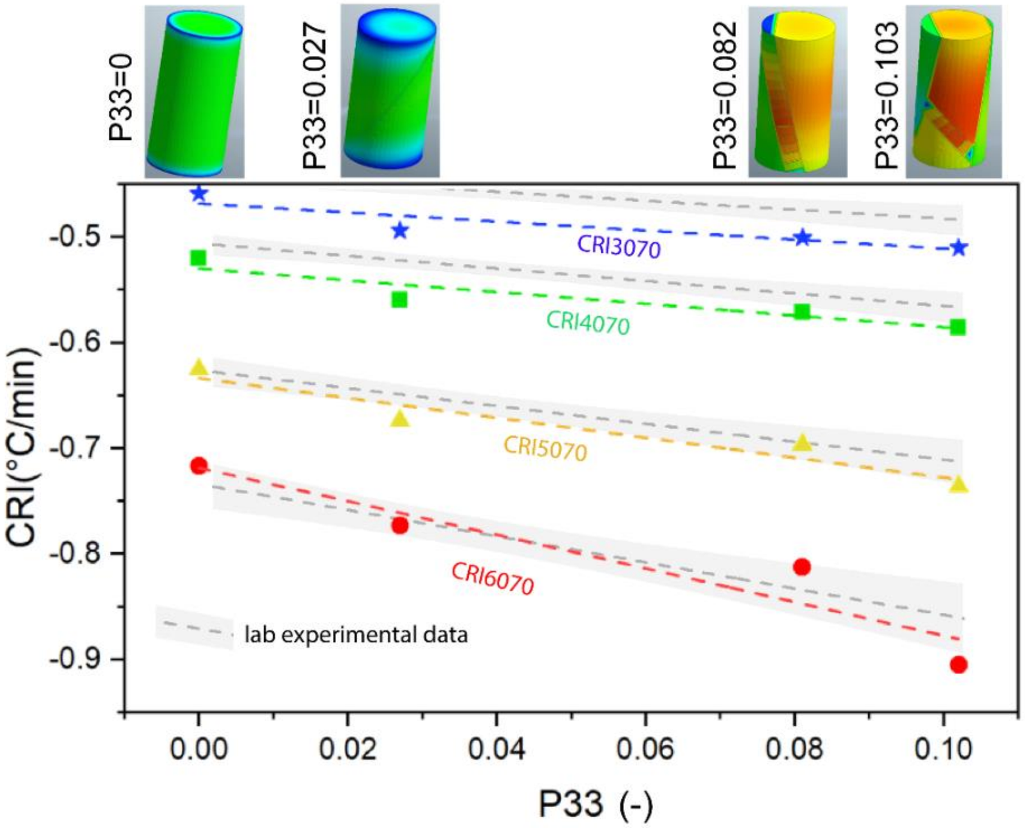

Figure 68 *Correlations between the Cooling Rate Index (various temperature ranges), and fracture porosity (P33), quantified starting from the results of 3D finite-element models, and comparison with corresponding experimental results. Coloured dots: numerical results. Coloured dashed lines: best fitting linear models for numerical results. Grey dashed lines: best fitting linear models for experimental results. Shaded areas: regression prediction bands (95% probability) for experimental data (Fig. 8b, Tables 3) (Franzosi et al., 2023a).*

4.4.4 Synthetic description of cooling dynamics: Curve Shape Parameter (C_{SP})

As showed in **Figure 66**, the values of CRI depend on the considered stage of the cooling process, as well as on the initial and ambient temperatures (Mineo & Pappalardo, 2016, 2019; Mineo et al., 2022). To isolate the control of fracturing state on the cooling behavior of fractured samples, we expressed their temperature histories in normalized form, according to LCM (**Chapter 3**, **Figure 69 a**). Normalized curves point out the difference among the cooling paths of samples with different fracturing states, independently on the absolute values of initial and ambient temperatures. This allows a sound comparison between the behaviors of different samples (or samples heated to different temperatures) in the same experimental environment, that only depends on thermal material properties and the representative size of the radiant elements forming the samples, according to the lumped capacitance equation (**Equation 12**).

We parametrized the lumped capacitance model on normalized experimental data by non-linear regression and obtained the values of the Curve Shape Parameter (C_{SP}, **Chapter 3;** Franzosi et al. 2023a) best representing the cooling dynamics of each sample. The C_{SP} provides a unique, scalar descriptor of the shape of cooling curves and shows a good linear correlation with the unbiased fracture abundance measures (**Figure 69** b; **Table 4**). Also in this case, the correlation is weaker when samples with a strongly discontinuum thermal behavior are included in the analysis, as in the case of mica schist samples.

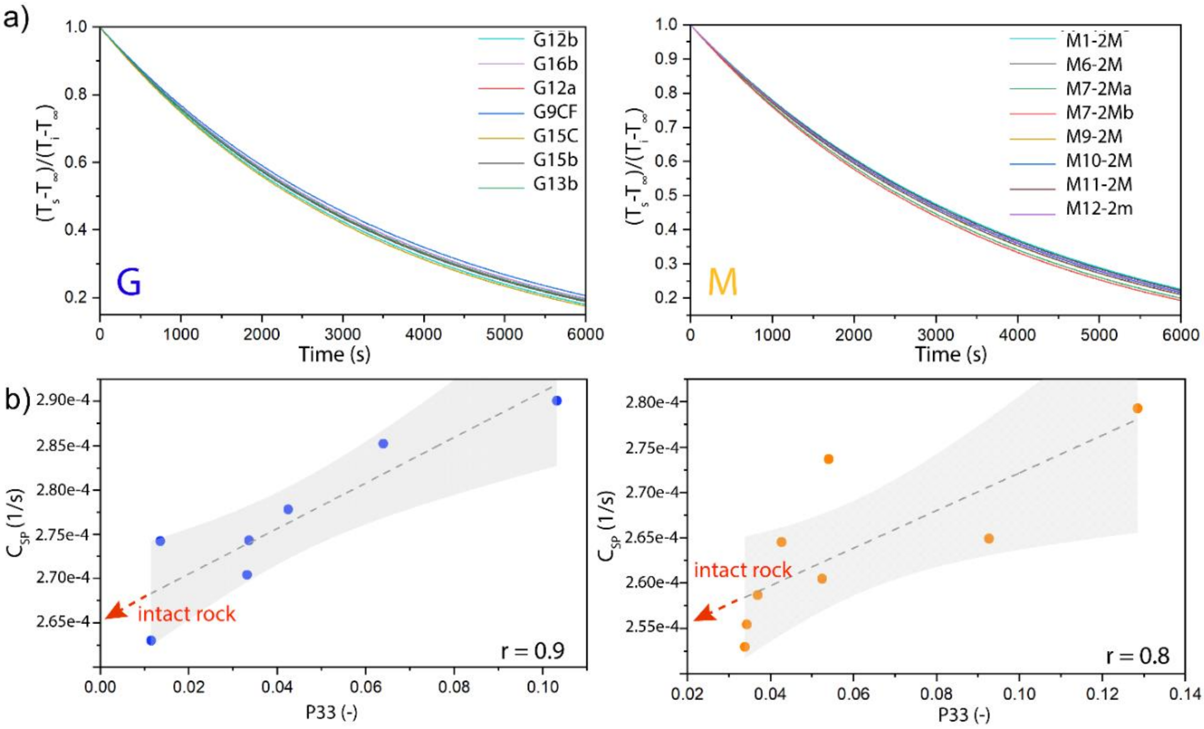

Figure 69 *Synthetic description of cooling dynamics. (a) Cooling curves with temperature normalized to ambient temperature for gneiss (G) and micascists (M) sample. (b) Correlations between the Curve Shape Parameter (CSP) and fracture abundance indices (P33, P32). See text for*

explanation. Dashed lines: best fitting linear model (Table 4). Shaded areas: regression prediction bands (95% probability); r: Pearson correlation coefficient. Red arrow: CSP intercept values (i.e., intact rock) (Franzosi et al., 2023a).

In general, the C_{SP} shows a consistent positive linear correlation with the degree of fracturing (**Figure 69 b** and **Figure 70 a**), in agreement with our hypothesis (**Chapter 3**). For both the gneiss and mica schist sample sets, we extrapolated the absolute values of C_{SP} for intact rock ($C_{SP(int)}$), (i.e. the intercept of regression curve; **Figure 69 b**) and used them to normalize the C_{SP} vs P_{33} and C_{SP} vs P_{32} regression curves (**Figure 70 b**). This representation of the relationships between C_{SP} and the fracture abundance measures seems independent on rock type and solely related to the fracturing state.

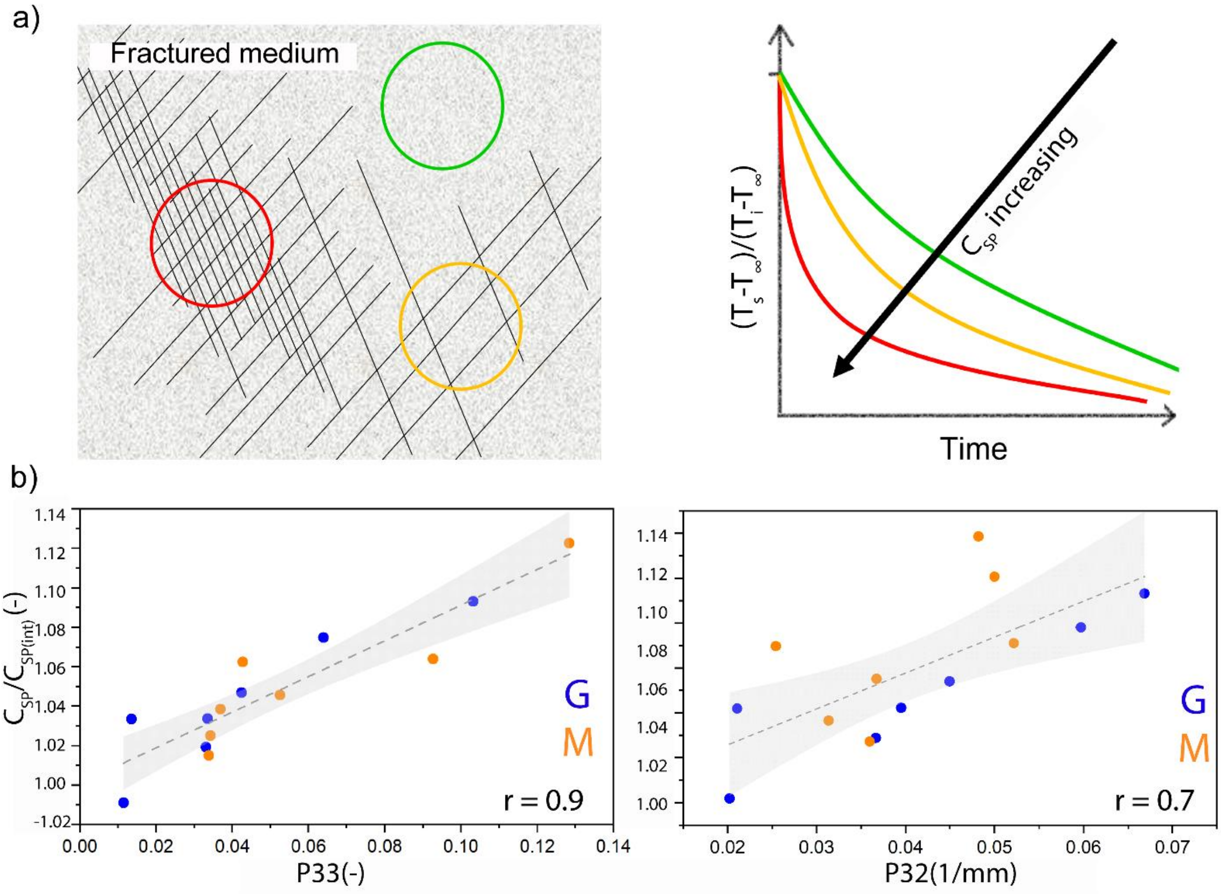

Figure 70 *Synthetic relationships between cooling dynamics and fracturing. (a) conceptual explanation, in a predictive perspective; (b) correlation between the normalized CSP and the fracture abundance indices (P33, P32) for entire studies sample population (i.e., both G and M). Dashed lines: best fitting linear model. Shaded areas: regression*

prediction bands (95% probability); r: Pearson correlation coefficient. (Franzosi et al., 2023a).

Table 4 *Goodness-of-fit statistics for the correlations between C_{SP} and rock fracture porosity (Fig. 11). R^2: coefficient of determination; r: Pearson correlation coefficient (parametric); ρ: Spearman correlation coefficient (non-parametric). G: gneiss samples; M: mica schist samples.*

Set	Variables	R^2	r	ρ
G	C_{SP} -P_{33}	0.82	0.90	0.96*
M	C_{SP} -P_{33}	0.61	0.78	0.95*
(*) Spearman correlation is significant at 0.05				

4.5 Discussion of laboratory-scale investigation results

A reliable assessment of the fracturing state of rocks and rock masses is key to quantify their hydro-mechanical properties and to track the processes that control the evolution of brittle rock damage at crustal levels, in natural and engineering contexts. However, this remains a difficult task, due to the intrinsically scale-dependent and heterogeneous nature of fracture networks (Dershowitz & Herda, 1992; Neuman, 2005; De Dreuzy et al., 2012) and to a variety of statistical biases (e.g. orientation, size) that affect fracture sampling (Priest & Hudson, 1976; Baecher, 1983; Mauldon et al., 2001).

The statistical sampling of discontinuities, based on field or remote mapping techniques (Priest & Hudson, 1976; ISRM, 1978; Sturzenegger & Stead, 2009), remains a fundamental approach to the characterization of fracture networks, yet its results are affected to great extent by scale, orientation and sampling biases (Rohrbaugh Jr et al., 2002). Non-destructive imaging techniques like X-ray computed tomography allow an effective characterization of the geometry and abundance of fractures in a small-scale three-dimensional space (Keller, 1998; Agliardi et al., 2014, 2017) but it has limited applicability *in situ*. On the other hand, field geophysical techniques applied to the assessment of rock mass quality (Barton, 2007; King, 2009; Dorn et al., 2012; Agliardi et al., 2016) usually lack the resolution required for a detailed characterization of rock fracturing state.

Infrared Thermography (IRT) applications started appearing in the fields of geoscience and geoengineering in the last 15 years, but the development of quantitative approaches to predict the physical properties of rocks by characterizing their thermal behavior are few and mostly limited to the assessment of density and porosity (Mineo & Pappalardo, 2016, 2019; Mineo et al., 2022). Our experimental investigation showed quantitatively that the cooling behavior of low-porosity (e.g. crystalline) rocks consistently depends on rock composition and fracturing state (i.e. fracture intensity, fracture porosity and their heterogeneity), and that modern thermal cameras offer both spatial resolution and measurement accuracy suitable to detect the different thermal responses of samples characterized by different degree of fracturing.

Our experimental investigation showed that the ambivalent "continuum vs discontinuum" nature of fractured rocks, that represents the major challenge when attempting a sound characterization of their hydro-mechanical behaviour (Hoek & Brown, 1997; Hoek & Diederichs, 2006; Rutqvist et al., 2015) also applies to their thermal behavior.

Recognizing thermal "continua" and "discontinua" according to the scale of observation is the first major step toward a proper interpretation of IRT experimental data and a solid characterization of their degree of fracture and fracture heterogeneity. (**Figure 65**, **Figure 60**). In fact, fracture abundance measures (Dershowitz & Herda, 1992) like volumetric fracture intensity (P_{32}) and fracture porosity (P_{33}) provide different information for practical use, depending on whether we consider "continuum" fractured rocks, with distributed damage, homogeneous strength, deformability, and permeability, or "discontinuum" materials, whose hydro-mechanical behavior is controlled by individual, persistent fractures.

Our results confirmed that simple, empirical linear correlations hold between different descriptors of cooling dynamics, as the already suggested Cooling Rate Index (Mineo & Pappalardo, 2016, 2019), and fracture abundance measures. These correlations can be established across different stages of cooling and consistently apply to sample populations characterized by different composition and fracture heterogeneity (**Figure 66**). Outdoor cooling experiments suggest that observed relationship between cooling dynamics and fracturing state can be detected by IRT also in natural conditions (i.e., solar forcing and free air circulation), despite the higher experimental noise related to small temperature differences, weather, and atmospheric effects.

Our 3D finite-element simulations of heat transfer, reproducing the observed cooling behaviors, allowed to support the experimental results and investigate the underlying physical processes and controls (**Figure 68**). Model results suggest that, consistently with the theory, the cooling process in a fractured medium is mainly controlled by the geometry and typical size of individual radiant elements (i.e., rock blocks forming the samples), dominating heat diffusion, and by the aperture of major (persistent) fractures, that influence the convective component of heat transfer. According to the models, the latter has a major influence on the bulk thermal response of fractured samples and may be the responsible of the higher temperatures of open fractures in early cooling stages.

Since the observed experimental cooling behavior strongly depends on the absolute thermal boundary conditions (initial and ambient temperatures) and by rock composition (lithology), it is generally difficult to use empirical descriptor like the Cooling Rate Index to describe rock fracturing in a practical predictive perspective, although it shows a clear correlation with rock porosity or geomechanical quality related to fracturing by previous works (Mineo & Pappalardo, 2016, 2019; Mineo et al., 2022). In this work, we overcome this limitation by parametrizing a theoretical description like the lumped capacitance model (Bergman et al., 2011) on normalized experimental data provided a synthetic scalar descriptor of the shape of cooling curves, i.e. the Curve Shape Parameter (C_{SP}). The C_{SP}, intrinsically referred to a continuous, homogeneous description of the fractured medium at the scale of consideration, is linearly correlated with unbiased fracture abundance measures (**Figure 69**) and independent on rock type (**Figure 70**). Such linear correlation, that requires some experimental quantification of fracture abundance to be established, is statistically strong (and thus suitable for prediction) when the C_{SP} values are normalized with respect to reference “intact-rock” ones.

Our results, although not directly applicable to *in situ* fractured rock masses due to different fracture network characteristics on sample and outcrop scales, lay the foundations to upscale our methodology to field conditions. This would require accounting for the radiative characteristics of natural environments, the limitations of the technique and the scale effects typical of fractured rock-mass, to achieve a contactless evaluation of fractured rock mass conditions for practical applications, e.g. block size distribution evaluation, rock mass quality designation, hydro-mechanical characterization for geological and engineering application.

5 Rock-mass characterization of rock fracturing state at slope scale

In this chapter we summarize our attempt to upscale the approach by Franzosi et al. (2023a) (**Chapter 4**) to the in situ scale of an engineered slope, in order to develop a practical contactless method to quantify and map the quality of fractured rock masses using Infrared thermography. The terms "in situ scale" refers to the scale at which the fractured rock-volume addresses the transition towards the concept of rock-mass, in which the mechanical properties of the intact rock, the attributes of the fractures and the geometry of the fracture network are integrated into the definition of a medium physical which can be assumed as continuous equivalent. The order of magnitude is therefore of the order of cubic metres (i.e 10^0 to 10^2 m^3), and clearly refers to the scales of investigation of natural outcrops belonging to homogeneous domains. By applying this survey scale to different outcrops and domains for example in a rocky slope, this can be considered as a transition to a scale representative of the entire slope (i.e. slope scale).

Such an upscaling exercise must face several practical issues, potentially hampering the required sensitivity of the IRT technique, the quality of detected signals, and the predictive capability of the analysis approach.

Main upscaling issues include:

a) difficult quantification of rock mass fracturing, due to orientation and size biases and to rock mass heterogeneity (**Chapter 2**).

b) characteristics of thermal radiation in natural environments and their effects on IRT measurements (**Chapter 3**) depending on absolute temperature regime and daily excursions, effects of solar forcing, sky radiation patterns, atmospheric effects, ground reflections, topographic controls (Spampinato et al., 2011, Minkina & Klecha, 2016; Kelsey et al., 2022; Flir Corporation, n.d.).

In this perspective, we choose the Mt. Gorsa porphyry quarry (Val di Cembra, Trentino, Italy) as a field laboratory. The area is characterized by a single rock type, but an extremely heterogeneous distribution of rock mass fracturing, due to structurally controlled slope instability mechanisms studied in detail by Agliardi et al. (2013). These characteristics, alongside with accessibility lack of vegetation cover and long-term accessibility make the quarry an ideal test site to carry out an experimental study deployed in the following steps:

a) UAV-based 3D reconstruction of the quarry topography;

b) field characterization of rock mass quality at selected outcrops;

c) time-lapse IRT measurements aimed at reconstructing the response (heating-cooling) of a significant part of the quarry face to solar thermal forcing;

d) development of a targeted methodology to correct IRT measurements for environmental effects;

e) *in situ* application of the method of Franzosi et al. (2023a) and statistical correlation analysis aimed at finding relationship between the Curve Shape Parameter and rock mass quality.

The research summarized in this chapter has been published in Franzosi et al. (2023b).

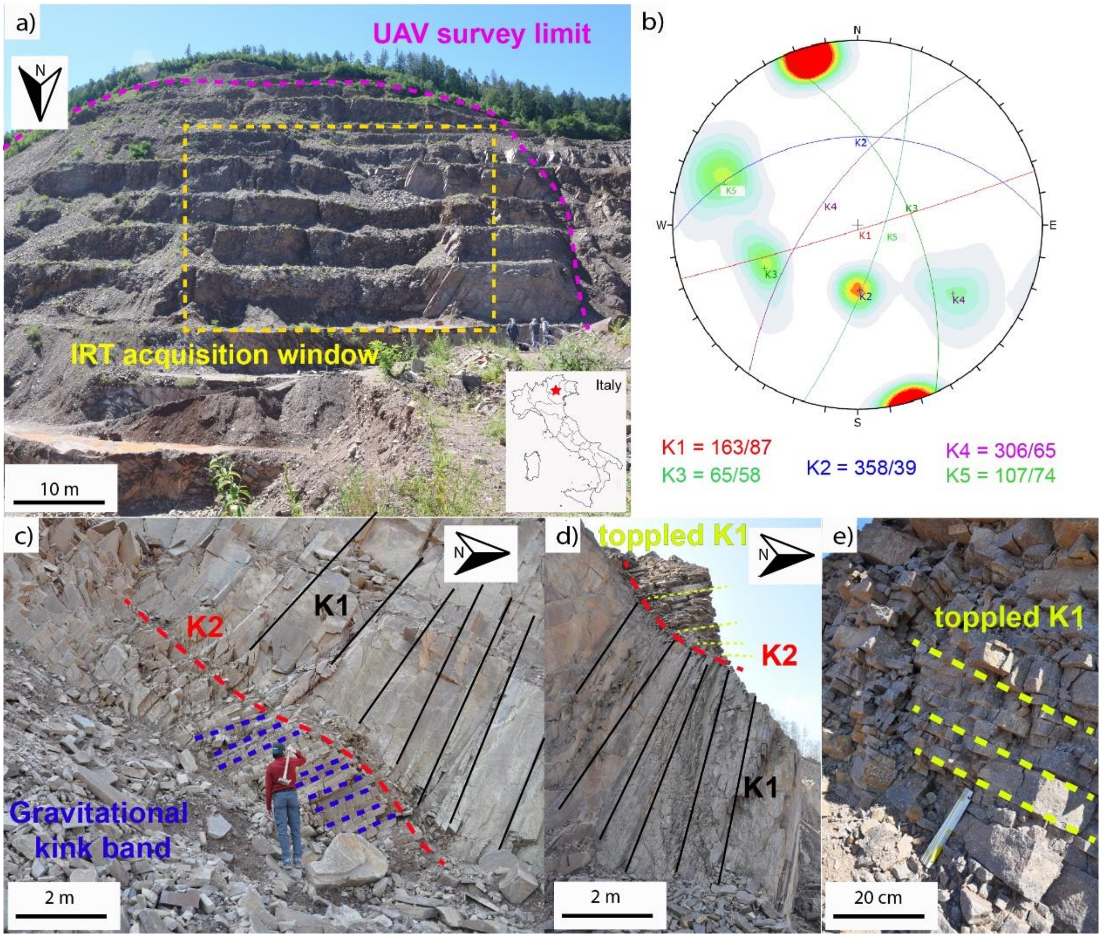

Figure 71. *Mt. Gorsa quarry settings. (a) front view of the quarry face, with the IRT acquisition window (yellow-dashed line) and UAV survey (purple-dashed line) are outlined. (b) Stereoplot representative of the rock mass structure described by (Agliardi et al., 2013). (c-d) field examples of fracturing mechanisms related to the gravitational reactivation of inherited fracture sets, namely: flexural toppling of K1*

joints, block toppling on K2 basal planes and planar sliding along K2 fractures, (e) resulting fracture damage (Franzosi et al., 2023b).

5.1 Field laboratory: Mt. Gorsa quarry

The Mt. Gorsa quarry is in the lower Cembra Valley (Trentino, Northern Italy) few kilometres north-east of Trento (**Figure 71**.a). The quarry, the morphology of which has changed significantly in the last decades, is characterized by N-facing, 250 m high benched slope, with an average slope of 35° and benches up to 10-15 meters.

Outcropping rocks belong to a huge volcano-sedimentary succession of the Southern Alps (Athesian Volcanic Group, AG; Rottura et al., 1998) widespread between Trentino and South Tyrol area. It consists of a suite of Permian calc-alkaline volcanic and subvolcanic rocks with interlayered discontinuous continental deposits, with maximum thickness locally exceeding 2000 m. The AG unconformably overlies pre- Permian metamorphic and locally a clastic sedimentary cover. The AG filled Early Permian fault-bounded depressions, reflecting a post-Varisican transtensional setting. During Neogene, the stress regime changed to N–S compression, causing the complete tectonic inversion of inherited structures as compressive structures and the deformation of the AG sequences. These are cut by steep, NW-SE trending dextral strike slip faults and NE–SW trending oblique-slip inverse sinistral faults. In this structural context, rock masses have a complex and strongly anisotropic structure, due to the occurrence of a typical pervasive jointing, characterized by cm to dm-scale spacing and extremely high persistence (Agliardi et al., 2013).

In the study area, rock belong to the Ora Formation (ISPRA, 2009), made of red to grey rhyolitic ignimbrites with an homogeneous porphyritic texture (35-40% of quartz + sanidine + plagioclase + biotite; Agliardi et al., 2013) and rare lithic fragments. Although this rock type is mostly unaltered, stiff and very strong (UCS>150 MPa), at Mt. Gorsa rock mass have a complex and strongly anisotropic structure (**Figure 71**.c-e) (Agliardi et al., 2013) related to five major discontinuity sets (**Figure 71**.b), namely:

a) K1: closely-spaced (average spacing: 5-15 cm), fully persistent joints, steeply dipping to SSE with a low orientation variability, responsible of a remarkable rock mass anisotropy;

b) K2: persistent fractures dipping 35–40° to the N, nearly parallel to slope topography and characterized by spacings in the range 0.5-2 m (outcrop scale) and up to 30 m (slope scale). Major K2 structures are associated to cataclastic bands up to 2 m thick;

c) K3: persistent fractures dipping 60° to the ENE, associated to thick gouge materials up to 1 m thick;

d) K4 and K5: NE-trending fractures steeply dipping to NW (K4) or SE (K5), ranging in spacing from some decimetres to over 10 m.

The spatially-variable characteristics of fracture intensity and persistence, and their geometrical relationships with the engineered slope, favoured the onset of structurally controlled slope instability mechanisms on different scales, i.e. from bench to the overall slope scales (Agliardi et al., 2013). These mechanisms include flexural toppling of K1 joints, block toppling on K2 basal planes and planar sliding along K2 (**Figure 71**.b-e), as well as the progressive failure across "rock mass bridges" forming kink bands (**Figure 71** b-e) and cataclastic shear bands connecting the tips of major non persistent K2 fractures. These mechanisms lead to the development of highly damaged slope domains bounded by K3 and K4 structures, and to a general decay of rock mass strength leading to a transition to a continuum-like fractured medium (Wyllie & Mah, 2004) that underwent major slope instability events in 2003, 2011 (Agliardi et al., 2013) and 2017.

These complex and widespread failure mechanisms affect the entire quarry face, but evolve differently in different sectors, thus resulting in an extremely heterogeneous pattern of rock mass fracture intensity and damage (**Figure 71**.c-e), that has been quantifies by Agliardi et al. (2013) in terms of Geological Strength Index (GSI, Hoek et al., 1998; Cai et al., 2004; Hoek & Brown, 2019).

5.2 Materials and Methods

3.1. 3D slope geometry: UAV photogrammetry

We reconstructed a detailed 3D geometry of the N-facing quarry face with a high spatial resolution, using UAV-based photogrammetry. Using a DJI Mavic Pro 2 drone, we performed a photogrammetric strip survey (**Figure 72**.a) over a plan area of about 0.15 km^2, looking the slope with an inclined optical axis (about 55°) to maximize the optical coverage of the benched slope from 600 to 900 m a.s.l. (**Figure 72**.a). We acquired 607 high-resolution RGB images (5472x3648 pixels) with an Hasseblad L1D-20c and geo-referenced using the drone onboard GNSS.

We processed the image dataset through Structure-from-Motion (SfM) photogrammetry (**Chapter 2**; Westoby et al., 2012; Wilkinson et al., 2016; Francioni et al., 2019) using the software Agisoft Metashape^{TM}, and obtained a 3D point cloud with an average ground resolution of 2.5 cm/pixel. The point cloud has native RGB attributes, allowing reconstructing the quarry front as a Digital Outcrop Models (**Chapter 2**, **Figure 72**.a) suitable for geological and geomechanical mapping. We clipped the point to the area of interest of **Figure 72** and filtered the dataset to improve the homogeneity of the nominal point spacing (about 3 cm). Finally, we computed point normal using kernel of 0.05 m, to obtain a quantitative characterization of local outcrop aspect, slope, and morphology.

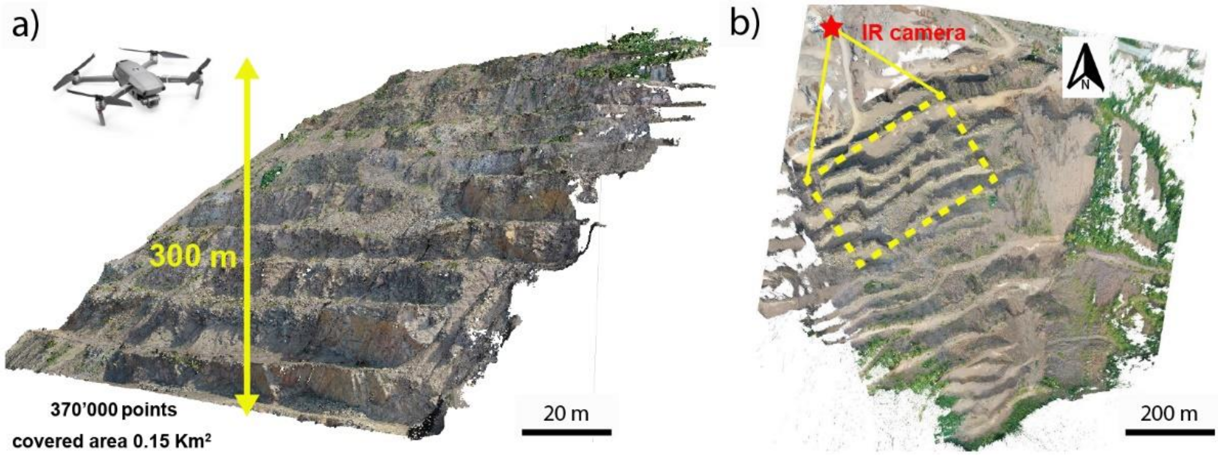

Figure 72 *3D slope geometry. (a) oblique view from NW of the slope point cloud, reconstructed by SfM using the photos acquired with DJI Mavic Pro 2. In the studied quarry sector (b) The IR-camera (red star) was placed at the base of the slope, above 200 m from the first bench (Franzosi et al., 2023b).*

5.2.1 Rock mass quality: field characterization

Among the different rating schemes available to describe rock mass quality, we selected the Geological strength Index (GSI; Hoek & Brown, 1997; Marinos & Hoek, 2000) in the modified version proposed by Cai et al. (2004). This quantitatively relates the GSI to discontinuity spacing and block size without losing the typical versatility of the GSI, that can be applied to an extremely wide range of rock types, heterogeneity and damage conditions (Marinos & Hoek, 2000) using a widely-used, mono parametric approach, intrinsically independent on water content.

This quality index satisfies some requirements to be correlated with the thermal response detected by IRT:

a) depends on few parameters and primarily on fracture intensity;

b) can be quantified for the full range of rock mass quality;

c) can be easily mapped in a spatially-distributed way.

We carried out rock mass and discontinuity surveys at 9 outcrops, safely accessible through quarry benches at different elevation (**Figure 73**.**a**). These outcrops are representative of slope sectors affected in different way by the structurally-controlled instability processes reported by Agliardi et al. (2013) and thus characterized by different rock mass damage states (**Figure 73.a**). At each outcrop, we performed standard window-sampling discontinuity surveys (ISRM, 1978) in order to frame each considered rock mass domain within the slope-scale structural setting and constrain the orientation, spacing, persistence, weathering conditions and intensity of inherited fractures as well as the characteristics of fractures related to damage induced by gravitational processes (**Figure 73.b-d**). Based on these observations, we provided GSI estimates, representative of the entire outcrop, quantified in ranges of 5, which in our experience provide the highest accuracy consistently achievable by trained experts (Agliardi et al., 2013).

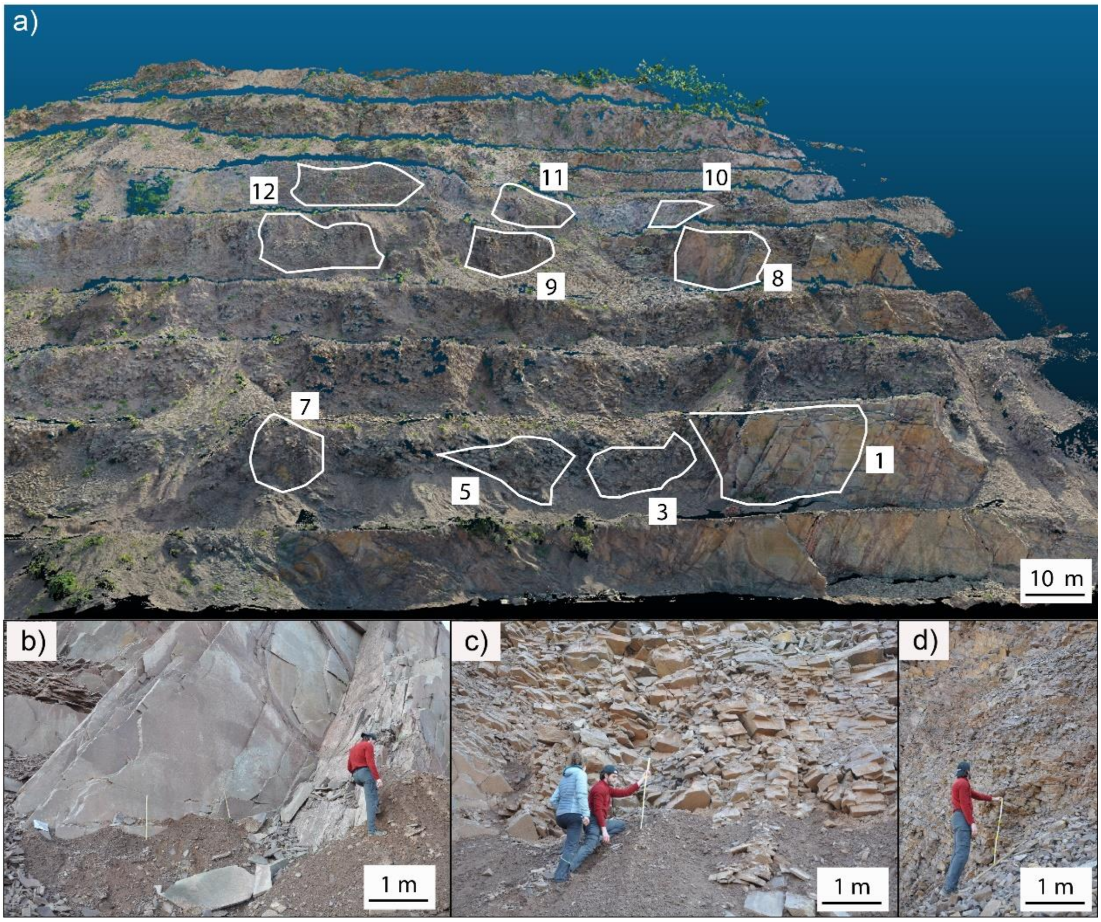

Figure 73 *Rock mass quality. (a) the 9 accessible outcrops on which we carried out in situ rock-mass surveys and quality designation using GSI. The outcrops are located on 3 different quarry benches and distributed over the IRT survey window (Fig1a), showing a significant variability in damage state (b, c, d) and block-size distribution. A clear transition from "discontinuous" to "equivalent continuous" rock masses can be observed at outcrops characterized by low (b) to very high (d) fracturing (Franzosi et al., 2023b).*

5.2.2 Rock mass thermal behavior: Infrared thermography

To explore the relationships between the response of rock masses to thermal perturbations, occurring in a natural environment subjected to solar forcing with sky and local ground radiative effects, and their geomechanical quality, we set up a campaign of IRT surveys and specifically-design field experiments.

IRT time-lapse survey

We carried out a IRT monitoring campaign investigating the area covered by the UAV survey and the characterized rock-mass outcrops (**Figure 72** b, **Figure 74**.a) starting from the last daily heating phase catching the complete cooling behavior of quarry face from sunset (stop of heating forcing) to sunrise (**Figure 74**.e) on 5th April 2022. The FLIR camera station was about 200 m to 250 m (depending on topography) from the N-facing quarry front (**Figure 72**.b) and cover a window of 74 x 56 m (**Figure 72**.b, **Figure 74**.a) with a ground resolution about 7 cm/px. Surveys were carried out with a FLIR™ T1020 high-resolution LW- thermal camera (1024 x 768 pixels, operating in the 7-14 µm band of the IR spectrum), characterized by a measurement sensitivity within 0.02 C° and a field of view (FOV) of 28° x 21°, in time-lapse mode (20 minutes). We acquired 57 thermograms from 2:00 pm to 8:00 am, while air temperature registered with a Omega™ OM-91 usb-logger (**Figure 74**.b-e). Relative Humidity (RH) changed between 60% and 70% during acquisitions period and sky covering was absent during this time.

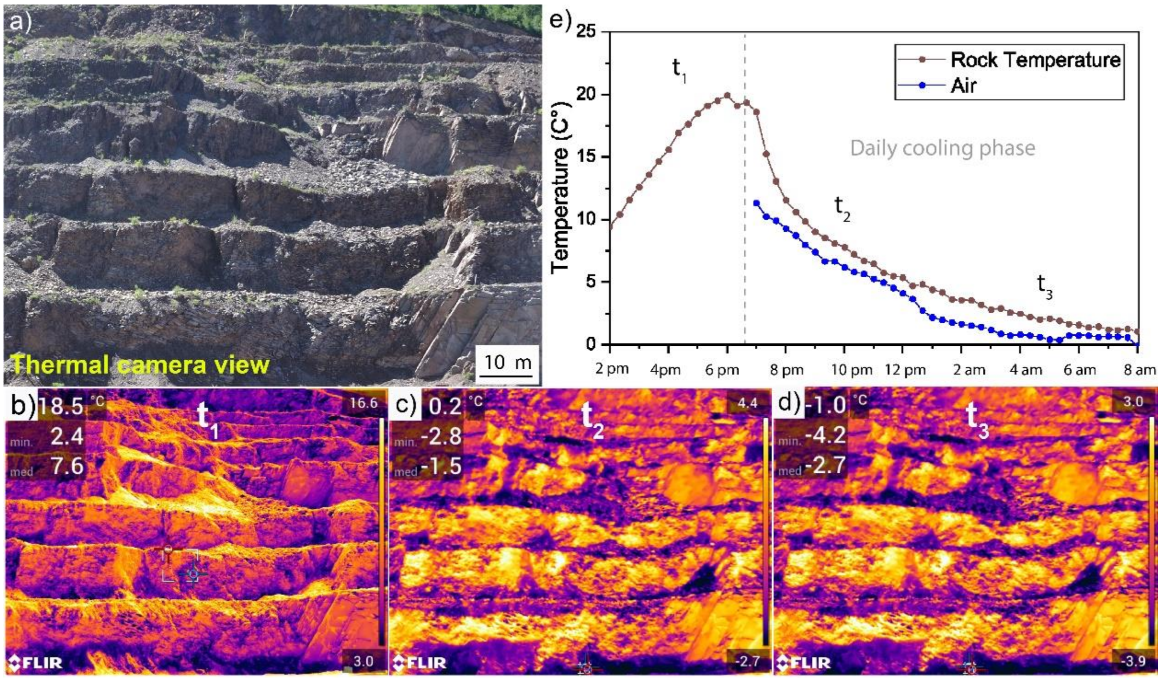

Figure 74 *IRT survey at Mt. Gorsa quarry on 5th April 2022 (a) RGB picture of the IRT acquisition window (Figure 71a). The high resolution thermograms (b-c-d-) recorded showed generally clear signal (e) and meaning of stable sky condition (no cloud cover) during all the experiment (brown cooling curve extract on outcrop 7. Rock temperature generally reach the maximum temperature due to the solar forcing of 20°C and the minimum above 2°C), starting the cooling phase just after the sunset (e) (Franzosi et al., 2023b).*

IRT correction workflow

We set up an innovative workflow to correct the acquired thermograms accounting for the diverse contributions typical of outdoor IRT measurements, outlined in **Chapter 3**. The workflow includes;

- standard characterization of rock emissivity;
- experimental modelling of the dependence of the sky-radiation component of reflected temperature on topography;
- implementation of a semi-automatic tool for the correction of acquired thermograms accounting for the local rock type and topographic conditions (**Chapter 3**, **Figure 47**).

We estimated the thermal emissivity of the porphyry rock forming the Mt. Gorsa slope by calibrating its IRT signal with reference to the one of a near- blackbody material at same temperature, following the approach of Mineo & Pappalardo (2021). We heated an unaltered sample of Mt. Gorsa porphyry, collected during fieldwork (**Figure 75**.a) in a laboratory oven up to ~70° degrees, covering a part of the surface with a black PVC tape with known emissivity (**ε**=0.97) as showed in **Figure 75**.a. After 24-hour heating, allowing a uniform temperature to be attained, we immediately acquired a thermal image of the sample (**Figure 75**.b). We quantified the reflected radiation component T_{REFL} using a gold panel. Since laboratory measurements were carried out from an acquisition distance of 1 m, atmosphere effects were negligible (Mineo & Pappalardo, 2021). Using the software Research IR-Max™ we measured the average temperatures of the black tape (T_{TAPE}) and the rock material (T_{ROCK}) within circular areas, to avoid sample edge effects. Finally, we set the emissivity of the black tape to 0.97 and tuned the rock emissivity until reaching the same recorded temperature (T_{TAPE}=T_{ROCK}=68.3 C°; **Figure 75**.b) to estimate rock emissivity (ε_{rock}=0.95), fully consistent with values reported in the literature for rocks with similar composition (Fiorucci et al., 2018; Mineo & Pappalardo, 2021; Sass et al., n.d.).

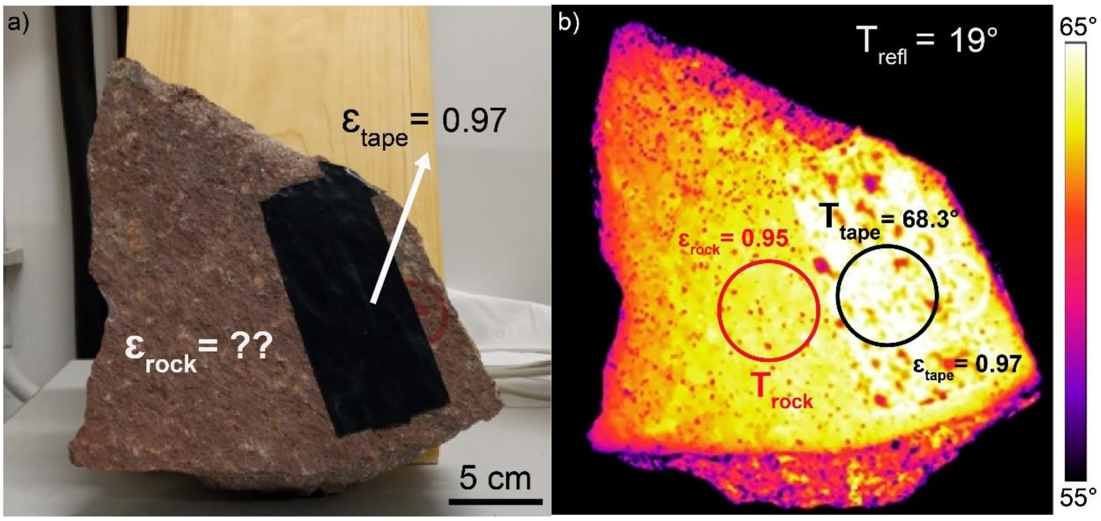

Figure 75 *Experimental setup to test the emissivity of the porphyry rock forming the Mt. Gorsa (a). Rock emissivity was tuned by fitting the temperature recorded in the red circle (T_{ROCK}) to the one recorded in the black one (T_{TAPE}) with emissivity set to 0.97 (PVC tape) (Franzosi et al., 2023b).*

To investigate and incorporate possible effects of topography on the sky-radiation contribution (**Figure 47**) of the reflected temperature component (Sass et al., n.d.), we designed and carried out *ad hoc* field experiments (**Figure 76**). We wrapped a plastic sphere (diameter: 1m) in rough aluminium foil, working as an almost perfect Infrared reflector (emissivity, ε=0.03). We located the sphere outdoor in an open space to have full sky visibility and to avoid ground reflection contributions (**Figure 76.a**). During the day with environmental conditions like those encountered at Mt. Gorsa (season, temperature range, cloud-free sky), we placed the thermal camera 2 m apart from the sphere looking horizontally in the equatorial plane of the sphere (**Figure 76**.a-c), and captured thermograms at different times during the day (**Figure 76**c). Using the software Research IR-Max™, we extracted temperature values along a vertical profile aligned with the maximum diameter of the sphere, corresponding to an arc of circumference connecting the two poles from zenith (0°) to nadir (180°; **Figure 76**.a-c).

As the Sky IR radiation is vertical (**Chapter 3**) we can consider the local sphere surface inclination as representing the topographic slope (α=0: horizontal topography). For each experiment, we consistently observed similar non-linear temperature trends from the upper to the lower pole (**Figure 76**), a clear effect of the reflection by different radiative contributions (**Chapter 3, Figure 47**). In the lower hemisphere (α > 90) we recorded rather constant temperature values consistent with ground temperature (green-shaded area on graph in **Figure 76**.b-c), while in the upper hemisphere temperature tend to reach lowest values above with sky IR temperature (Kelsey et al., 2022) (-55°C <T_{REFL}< -60°C, **Figure 76.b-c**). It is clear from the experimental evidence how the sky-radiation contribution increases moving from the equatorial plane (α=90°) toward the upper hemisphere pole (α=0°) reaching the minimum value for T_{REFL}=T_{SKY}. It is important to emphasize how (**Figure 76**.b-c) that for 0°< α < 30° dip we observe also a zone of relative increasing of the T_{REFL} (yellow-shaded area on graph in **Figure 76.b-c**) due to an emissivity *bias* related not topographic slope but with the specular radiation of the aluminium sphere, would not affect more lambertian materials (i.e rocks, **Chapter 3**; Howell, 2018; Vollmer & Möllmann, 2018; Rafael et al., 2019;).

Temperature recorded by the thermal camera during this experiment thus show a strong dependence of the T_{REFL} value on the alpha value (i.e., topographic slope), which is in agreement with the phenomenon observed experimentally by (Sass et al., n.d.).

We fitted experimental temperature values collected in all experiments in the α range between 30°-90°, avoiding the bias (**Figure 76.b**) using an exponential growth function (**Figure 76.d**). We propose a site-specific Sky-Dip Reflection Model (SDRM; **Figure 76**.d) that relates the recorded reflected temperature component with the local inclination of a surface exposed to the sky:

$$SDRM \ = T_{REFL} = \ 0{,}07e^{(\alpha/_{13})} + \ T_{SKY}$$

Equation 34

Where:

SDRM is the Sky-Dip Reflection Model

T_{SKY} is the sky temperature (°C)

T_{REFL} is the defined in **Chapter 3** (and converted in °C)

α local sphere surface inclination (i.e. topographic slope) (°)

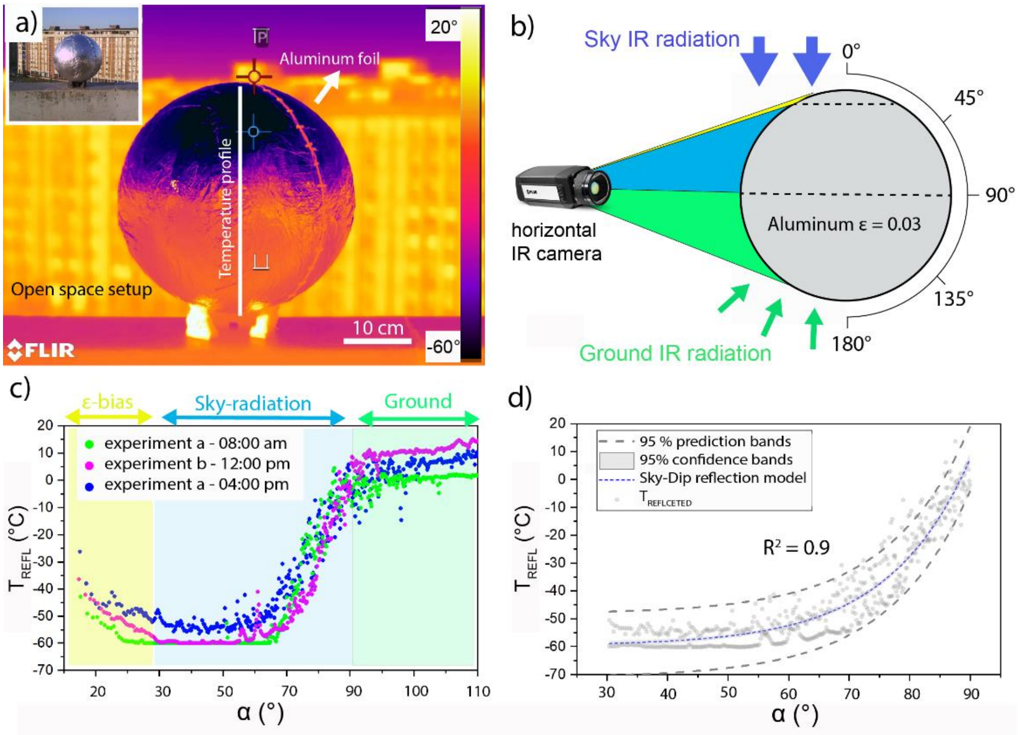

Figure 76 *Experimental characterization of the sky radiation reflected temperature contribution. The conceptual scheme in (b) explains what is observed experimentally from the vertical profiles in (c), where the different contributions and effects (yellow-blue-green panel) that the angle of view of the sky and ground radiation have in the different tilt ranges of a surface are separated. The sector (d) between 90° and 30° inclination turns out to be the most affected, according to the empirical experimental relationship fitted and defined as Sky-Dip Reflection Model (SDRM, Equation 34) (Franzosi et al., 2023b).*

For surfaces with $\alpha > 90°$ the T_{REFL} can be considered equal to the one assumed for α=90, based on the experimental evidence in the lower hemisphere of the ball (**Figure 76**.c).

Model application requires associating a value of local topographic slope to every pixel in thermograms (**Figure 74.b-e**). We used the high-resolution 3D point cloud representation of the quarry (**Figure 72**) to derive local values of slope dip via point normal calculations in Cloud Compare ™ (http://cloudcompare.org/).

We manually geo-referenced in Agisoft Metashape ™ the RGB image of the scene acquired by the thermal camera during IRT acquisitions, to estimate its internal orientation parameters omega (ω), phi (ϕ) and kappa (κ) i.e. the internal orientation parameter of the camera (Agisoft, 2018) (**Figure 77.a**) and UTM coordinates of FLIR camera position, defining camera system orientation (**Figure 77.a**). We were able to calculate the rotation matrix (R) of geographic coordinates to the camera coordinates as:

$$R = \begin{bmatrix} \cos(\kappa)\cos(\phi) & -\sin(\kappa)\cos(\phi) & \sin(\phi) \\ \cos(\kappa)\sin(\omega)\sin(\phi) + \sin(\kappa)\cos(\omega) & \cos(\kappa)\cos(\omega) - \sin(\kappa)\sin(\omega)\sin(\phi) & -\sin(\omega)\cos(\phi) \\ \sin(\kappa)\sin(\omega) - \cos(\kappa)\cos(\omega)\sin(\phi) & \sin(\kappa)\cos(\omega)\sin(\phi) + \cos(\kappa)\sin(\omega) & \cos(\omega)\cos(\phi) \end{bmatrix}$$

Equation 35

Where:

omega (ω), phi (ϕ) and kappa (κ) are the camera rotation angles (°)

R is the rotation matrix

At this point, known the camera center C_0 coordinates, we were able to transform the point cloud from UTM to camera system (**Figure 77**.a) using the "*apply transformation*" tool within Cloud Compare ™ according to the following transformation:

$$C = R^T(P - C_0)$$

Equation 36

Where:

P is a generic point in geographic coordinates (X_pY_p Z_p)

C is the P point in camera coordinates (X_c Y_c Z_c)

C0 is the camera position (X_c= 0 Y_c= 0 Z_c= 0)

R is the rotation matrix

Using a MATLAB ™ script we were able to project the C point on focal plane image (**Figure 77**.a) using a reprojection model without distortion (Agisoft LLC 2023):

$$\begin{matrix} X_{pi} \\ Y_{pi} \end{matrix} = \begin{matrix} fX_c/Z_c \\ fY_c/Z_c \end{matrix}$$

Equation 37

Where:

X_{pi} and Y_{pi} are the coordinate of the point C on thermal image.

f is the focal of thermal camera.

In this way we obtained a series of X_{pi}, Y_{pi} with associated value of dip angle, creating a raster that we meshed the value with at the resolution of the thermal image, obtaining a new raster representing the map of dip on the thermogram (**Figure 77**.b). Using our experimentally-derived SDRM (**Equation 34**) this raster was then converted in a map of estimated reflected temperature with the same resolution of IRT dataset (**Figure 77**.c;) to correct acquired thermograms (**Figure 77**.c; **Figure 74**.b-d). Map ground pixel presents an estimate dimension range between 0.005 to $0.01 m^2$ in function of the distance between the different benches and the IR camera.

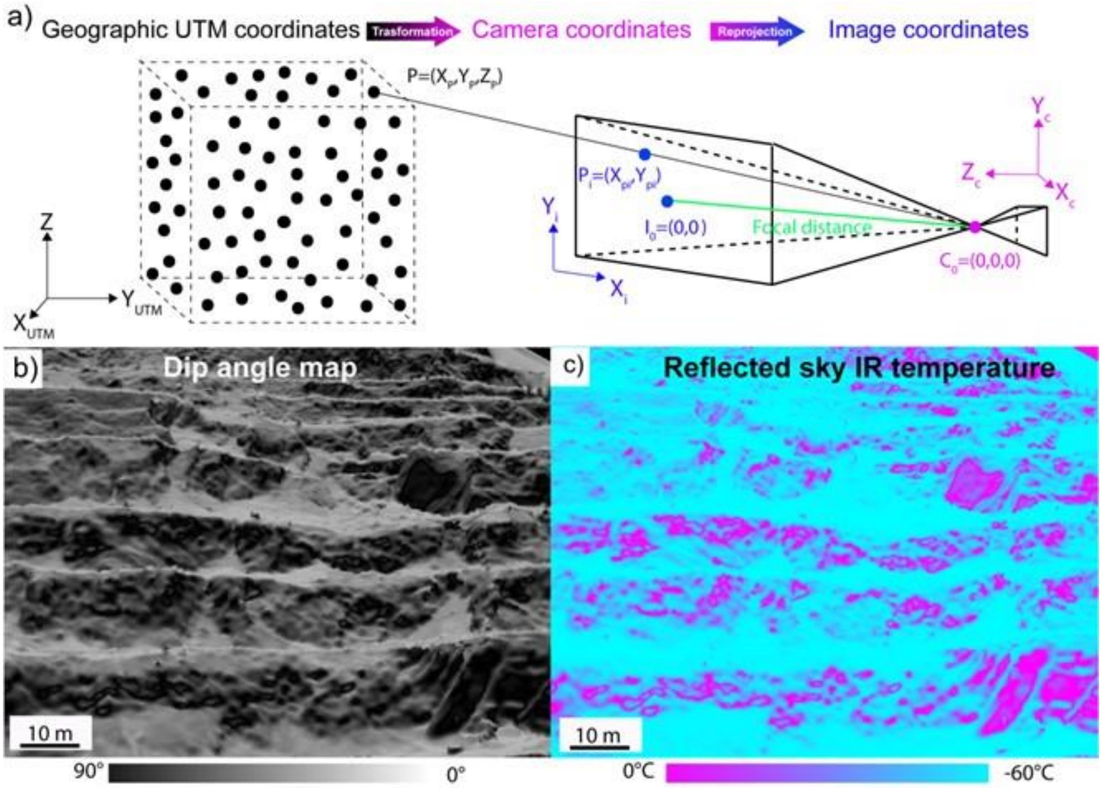

Figure 77 *The scheme proposed in (a) shows the workflow to reproject the points of the 3D cloud to onto the focal plane of the thermograms (Figure 74.b-d), generating a slope map (b) for each pixel that corresponds to the IRT window of the measurements on the quarry slope (Figure 71.a). Through the use of the SDRM (Equation 34), from this it*

was possible to generate (c) a map of the reflected IR temperature at each point (Franzosi et al., 2023b).

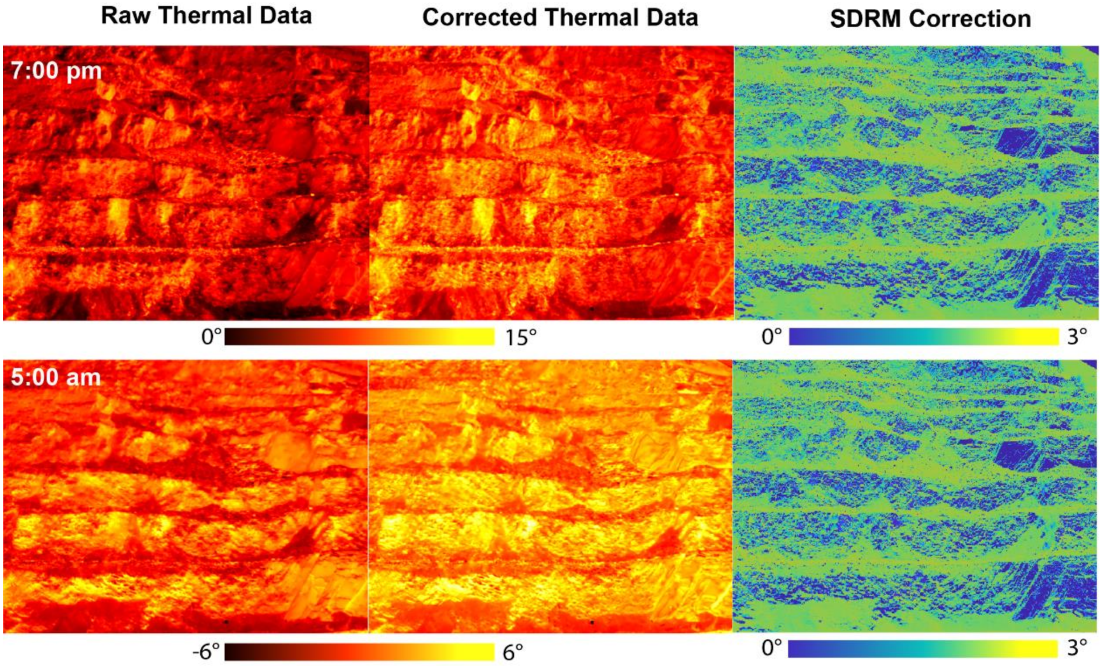

Figure 78 *Examples of the application of the correction (Equation 34) to thermograms acquired at different times during the IRT measurement campaign (Figure 74). As expected from the experimental evidence (Figure 76), the difference between the raw and corrected temperature data increases the more the inclination of the in-square surface tends to low values (horizontal), with correction peaks of up to 3°C, which can be important in the ranges analysed by our analyses (Figure 74.e) (Franzosi et al., 2023b).*

.

After this process we obtained (1) a correct emissivity for the porphyry ε_{ROCK} (keeping it constant during further calculations) and (2) the T_{REFL} for each pixel of the raw thermal image. With $\tau = 0.94$ representative of our environment during the acquisition (Minkina & Klecha, 2016), the "measurement formula" (**Chapter 3**) is applied in order to estimate the corrected temperature T_{OBJ} from the raw temperature T_{APP} (**Figure 78**).

As we can see from **Figure 78** the main effect of the correction is to reduce the "cold sky" IR reflected temperature and so increase up to 3°C the temperature on the most horizontally faces of the outcrops, while temperature of vertical faces remains stable, according with the temperature deviation range recorded on rock samples in outdoor experiments by (Sass et al., n.d.).

5.2.3 *Rock mass cooling dynamics: Curve Shape Parameter*

We upscaled to *in situ* condition the approach proposed by (Franzosi, Casiraghi, et al., 2023) (**Chapter 3**) to characterize the fracturing state of rocks by modelling experimental cooling curves reconstructed from IRT measurements. In **Chapter 4** we found that fractured rocks subjected to forced heating cool faster than intact ones.

The C_{SP} provides a synthetic description of the shape of experimental cooling curves and was obtain by fitting the linear part of the cooling curve. C_{SP} incorporating thermal properties of the rock material, the boundary convective condition of the solid-air interface, and most importantly the representative size of radiant element (i.e. rock blocks) of rock mass portion, correlated with fracture abundance (Franzosi et al.2023a).

The method is based on laboratory cooling experiments performed in indoor controlled conditions (forced heating, constant and steady thermal boundary conditions) that are usually not satisfied *in situ*. Moreover, the multi-scale and heterogeneous nature of *in situ* fractured rock masses and the rock volumes involved by the investigation potentially affect the ability of the IRT to detect cooling behaviors related to different rock mass quality.

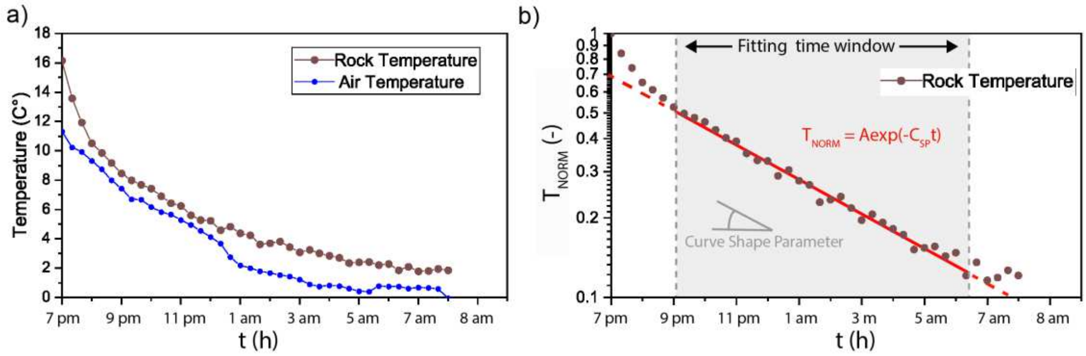

Figure 79 *(a) Example of a rock cooling curve (brown dotted line) extracted at the quarry face extracted from the series of acquired thermograms, and related measurements of ambient temperature (blue dotted line) reaching the asymptote overnight; (b) by normalizing the temperature values and plotting them on a logarithmic scale, it is possible to observe the time window (grey-dashed panel) in which the distribution takes on a negative exponential trend (red line) that can synthetically describe the cooling history of the rock-mass sector considered using* C_{SP} *(Franzosi et al., 2023b).*

From the corrected thermogram stack (**Figure 78**) , for each pixel we extracted temperature time series that capture the heating under solar forcing of different parts of the scene and the subsequent cooling (**Figure 74**.e). For each pixel, we extracted the cooling curves related to the time between 7:00 pm (after sunset) until 7:30 am (just after sunrise) (**Figure 79**.a).

To apply the methodology of Franzosi et al. (2023a) in field conditions given the non-constant environmental temperature during the night, we assume that the rock mass made of different domains with different fracturing states, continuously tend to reach a continuously changing asymptotic value, eventually represented by the lowest air temperature reached overnight (**Figure 79.a**). Normalizing all values of rock cooling curves by this temperature (Bergman et al., 2011; **Figure 79**.b) we can define a time window (**Figure 79.b**) in which the cooling curves of rock-mas can be fitted using Lumped Capacitance approach as a negative exponential law (Bergman et al., 2011; Franzosi et al., 2023; **Figure 79.b**), assuming the CSP as integral description of the rock-mass cooling path.

Then we implemented an original MATLAB™ tool that automatically corrects the thermogram stack and extrapolates the CSP value for each pixel of thermogram cooling series, returning only for pixels at which the correlation coefficient R^2 exceeds a certain user-defined threshold (e.g R^2 > 0.85) in order to exclude the points that do not respect the assumed empirical cooling behavior reducing sources of error.

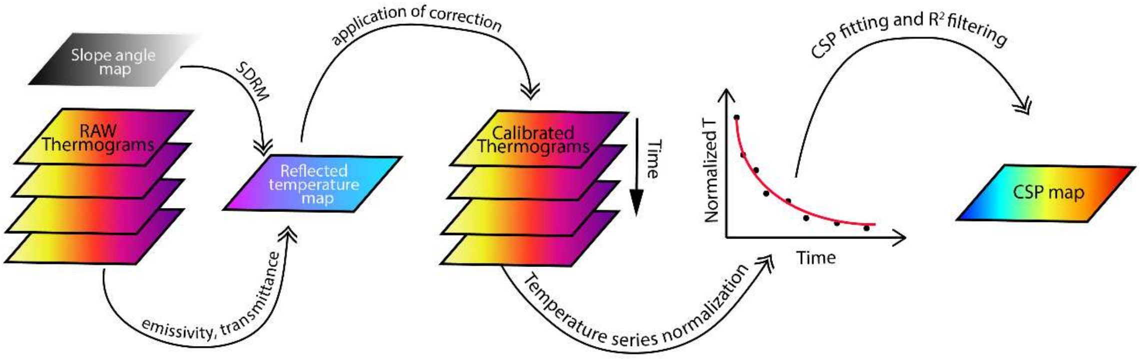

Figure 80 *Progressive steps of the CSP MATLAB tool.*

The CSP MATLAB tool, allows starting from the thermogram series (.RJPEG) and arrive at the production of a CSP map automatically, through several steps (**Figure 80**).

The inputs are mainly two:

- .CSV of the thermograms: it is important to export the frames of the cooling acquisitions (**Figure 74** b-d) as .csv files in the same folder where the script is saved.

To do this it is possible to load the sequence on the IR-max program (keep emissivity and transmissivity equal to 1).

- .TIFF of the slope map **(Figure 77b)**: the obtained slope map must have the same resolution, extent and reference system of thermograms.

In the first part of the script all calibration variables (**Chapter3**) all settled, which will be saved as inputs for subsequent steps.

The first step creates the reflected temperature map (**Figure 77c)** that is useful for correction and calibration of the data, starting with the previously loaded slope map and using the empirical reference equation (e.g SDRM, **Equation 34).** The output will then be a matrix of the same size as the thermograms saved in the folder.

The cooling .csv are loaded in temporal order and converted from apparent temperature to kinetic temperature one by one according to the calibration formula (Chapter 3) . The output is then a multidimensional matrix each level is a matrix representing a calibrated thermogram, ordered by acquisition time (**Figure 80)**.

Each pixel is then normalized along each of its time columns according to the ambient asymptote temperature defined by the operator. Next, exponential fitting and calculation of the C_{SP} for each pixel (filtered according to selected R^2) is performed and mapped to a matrix that has the same dimensions as a thermogram.

The output of the CSP map (**Figure 85**) can be exported to various formats (.TIFF, .JPG, .TXT, .CSV...) depending on the subsequent analysis.

Introducing the script in this context becomes essential because we are dealing with a complex analysis of spatially distributed data. In our previous laboratory work, our primary focus was on obtaining averaged responses from relatively small and well-defined samples. However, the current situation presents us with a vast dataset characterized by an unknown and variable distribution. Consequently, the development of a tool to address these challenges has become an important development.

The script conducts a pixel-by-pixel analysis, representing a fundamentally different approach from the sample-based methodology used in the laboratory. This contrast arises from the absence of *a priori* knowledge regarding the size and extent of the "radiant object" we aim to map in this context. To achieve a detailed and comprehensive representation, we employ the C_{SP} calculation at the individual pixel level, followed by the subsequent averaging of results across various scales. This method allows for a more precise evaluation of the radiant object within a context characterized by uncertain dimensions and distribution.

This processing allows us to obtain C_{SP} maps on the entire surveyed quarry face, encompassing an investigated area exceeding 80000 m^2 in a spatially distributed way. C_{SP} maps have been obtained by processing the thermogram stack at the original spatial resolution, with an estimated resolution of the ground pixel of 0.005 to 0.01m^2 and then smoothed using circular moving windows with areas of 0.005, 0.5, and 2 m^2; respectively, in order to test the scale dependency of the results and identify the spatial scaled that allow capturing the "equivalent continuum" thermal response of rock masses with different quality (Franzosi, Casiraghi, et al., 2023) (**Figure 81**).

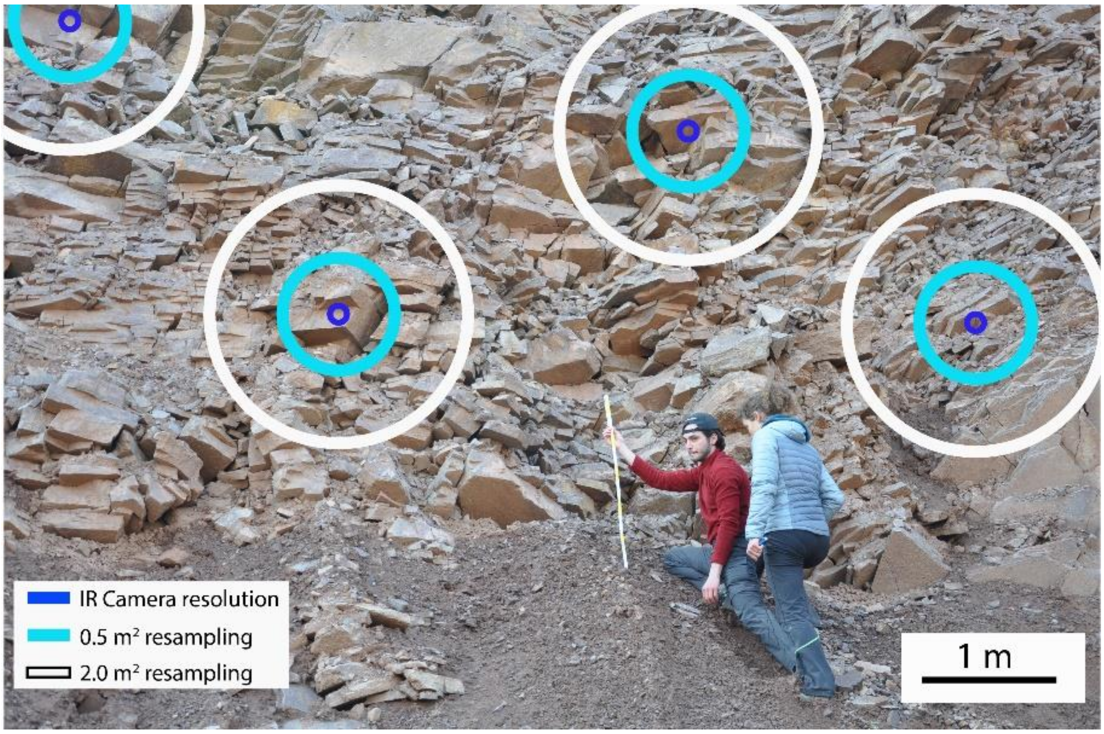

Figure 81 *The CSP maps were spatially smoothed from the original resolution (IR camera resolution, blue circle), toward higher resolutions (blue circle, white circle); the homogenization of the data would return a signal more representative of the behaviour of the average distribution of blocks in a domain, rather than of individuals, also reducing the experimental noise associated with the 3D morphology of the slope (Franzosi et al., 2023b).*

5.2.4 Contactless distributed mapping of rock mass quality: C_{SP}-GSI relationship

In **Chapter 4** we found a laboratory-derived quantitative correlation between the C_{SP} and unbiased fracturing measures like the volumetric fracture intensity (P_{32}) and the rock porosity related to interconnected fractures open to the external boundary (P_{33}). In the upscaling phase, since obtaining these unbiased measures is usually unfeasible in *in situ* surface investigations in this work, we made an attempt to correlate the obtained spatially distributed values of C_{SP} with our field estimates of the Geological Strength Index (GSI).

We extracted C_{SP} value populations within outcrop areas characterized in terms of GSI (**Figure 73**), using circular sampling windows with radius of about 25% of the height of the related quarry benches, making them comparable in terms of ground surface covered (**Figure 82**). From each C_{SP} map obtained by smoothing (**Figure 81**) we extracted C_{SP} values, plotted them against the corresponding GSI range (**Figure 73**) and filtered out values outside the interquartile range (IQR) (Turkey, 1977; Whaley III, 2005).

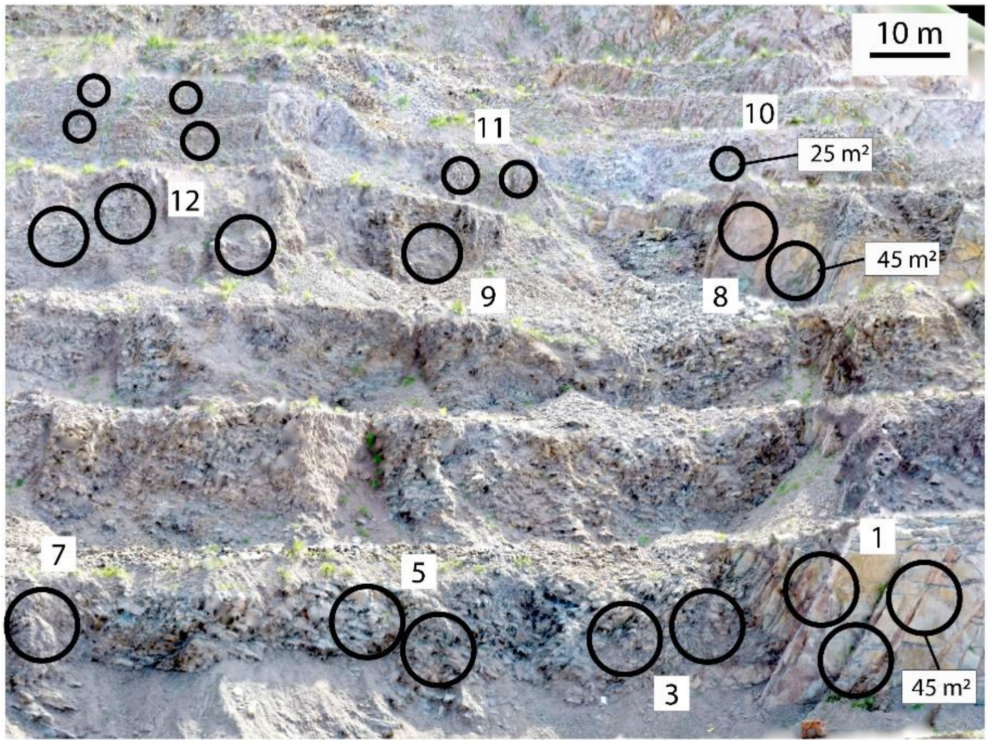

Figure 82 *The C_{SP} value for the sampled outcrops (Fig3.a) was conducted using an approach that considers the representative size of a domain understood as a circular area with a diameter equal d ½ of the height of the 3 main steps, generating windows (black circles) that are comparable for shape and real surfaces (Franzosi et al., 2023b).*

The 25th and 75th quantiles provide a measure of data variability, in order to reduce the impact of outliers and anomalous values on the search for correlations between C_{SP} and GSI. To search for such correlation, we needed a fitting model that was representative of the transition of the physical-mechanical characteristics of the rock mass with respect to its structure. Previous studies (Hoek & Diederichs, 2006; Agliardi et al., 2016) showed that for very high (GSI > 60) or very low (GSI < 30) GSI values, the mechanical properties of the rock mass tend to exhibit asymptotic behaviors corresponding to the "continuum" properties of intact rock (high GSI) or disintegrated rock masses (low GSI), respectively. A nonlinear fitting model well suited to describe this kind of behavior is represented by a sigmoidal function (e.g. Boltzmann).

5.3 Results

5.3.1 Rock mass quality: characteristics and distribution

In situ discontinuity surveys and rock mass assessment confirmed the strong rock mass heterogeneity reported by Agliardi et al. (2013), resulting in sharp changes of rock mass quality across rock domains with volume of tens to thousands of cubic meters, separated by narrow structural features of transition zones related to structurally controlled slope instability processes (**Figure 71**.c-d, **Figure 72**.b, **Figure 73**.b-d). This peculiar geo-structural setting provides us a variety of mono-lithologic outcrops with different rock mass quality in a limited study area that can be captured in one IRT scene (**Figure 74**) representing the typical structure of an open-pit mine. Selected outcrops correspond to sections of the 10 to 16 m high quarry vertical benches with different accessibility (**Figure 73**, **Figure 77**.b), bordered at the foot by small debris talus with lower inclination (**Figure 77**.b).

Our direct estimates of Geological Strength Index (**Figure 83**), that depend on rock mass structure, fracture density (and typical block volume) and weathering of observed rock masses and discontinuity surfaces (Cai et al., 2004), revealed outcrops characterized by extremely variable rock mass quality (**Figure 84**, **Figure 73**), with GSI ranging between 25 and 65. The plot in **Figure 83** shows that the values of GSI mostly depend on the fracturing states, with typical fracture spacing ranging between 2 and 80 cm, and much less on surface weathering condition.

In fact, while we observe a rather homogeneous and superficial weathering state across outcrops, rock fracturing is characterized by sharp variations (**Figure 71**.c-d, **Figure 72**.b, **Figure 73**.b-d), from rather intact and heterogeneous rock masses (Vb from 0.1 m^3 to some m^3; **69**.b, **Figure 83**) to highly and homogeneously fractured rock masses with Vb as low as 10 cm^3 (**Figure 71**.d, **Figure 73**.d, **Figure 83**). The variability (**Figure 83**) of GSI estimated is typically higher in low-medium quality rock masses (35<GSI<50) and lower in high and very poor-quality rock masses.

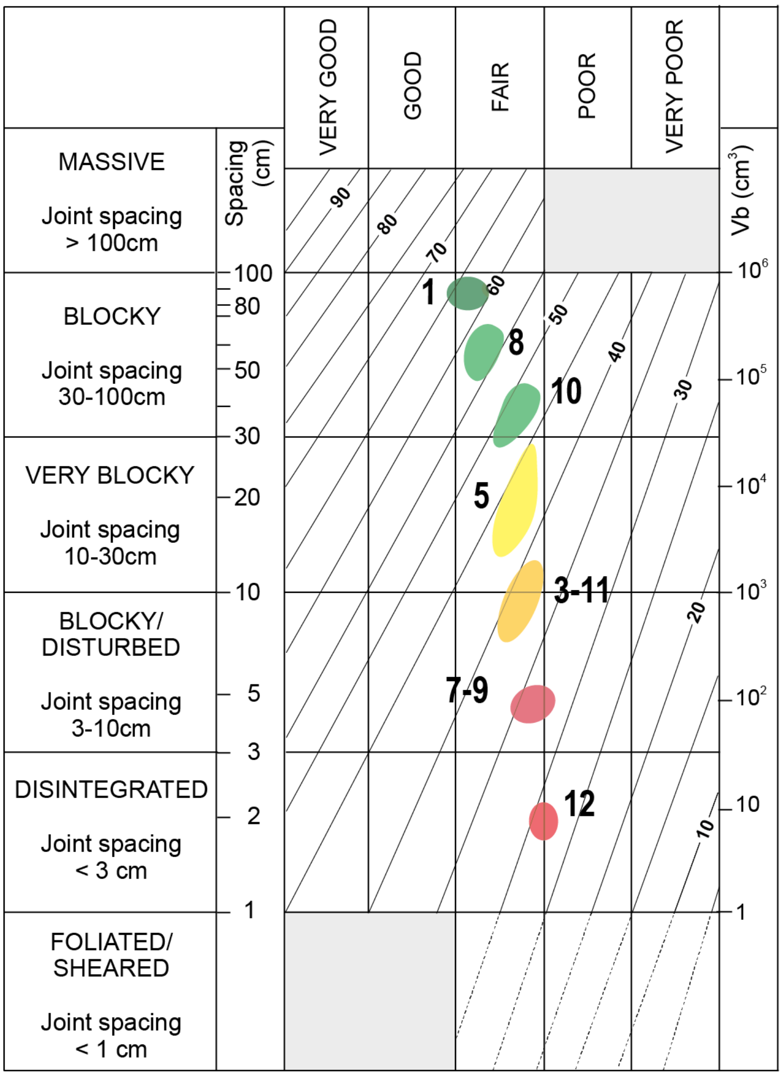

Figure 83 *Abacus of GSI according to the version by* (Cai et al., 2004) *and the values assigned to outcrops numbered according to Figure 73, that show clearly the wide range of rock-mass quality along the slope. The variability of block size increases in the portions of the rock mass characterized by intermediate GSI values (3-11-5) while it diminishes for very high or very low values; the degree of alteration remains homogeneous for the observed outcrops classifying in the "fair" range (Franzosi et al., 2023b).*

Figure 84 *Field photos taking during geo-mechanical surveys, for all the analyzed outcrops.*

5.3.2 Rock mass cooling dynamics

Rock-mass cooling histories (**Figure 74**), captured at each pixel of acquired thermal images, were corrected and characterized in terms of C_{SP} all over the IRT scene (**Figure 79**, **Figure 85**). The obtained maps of C_{SP} provided a continuous, spatially distributed description of the cooling behavior of rock masses forming the studied sector of the Mt. Gorsa quarry face. The analysis provided a clear illustration of the heterogeneous of spatial variability of the cooling dynamics across sectors characterized by different fracturing states and rock mass quality (**Figure 85**). Debris-covered areas are easily segmented (C_{SP} values above 0.3 h^{-1}, **Figure 85**) from rock-mass outcrops, while outcrops with different fracturing degrees and related progressive or sharp transitions and clearly captured by the spatial patterns of C_{SP}.

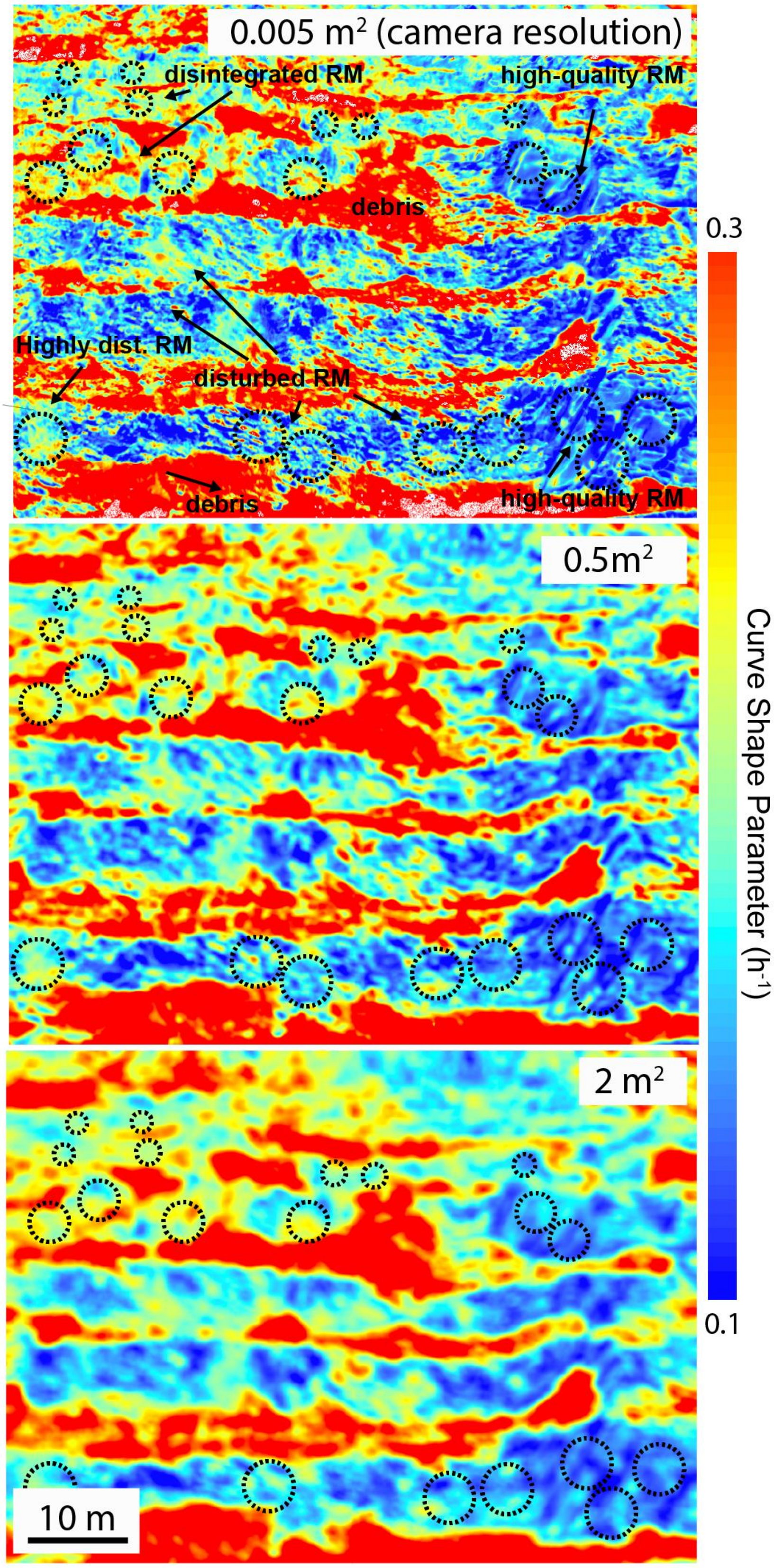

Figure 85 *C_{SP} maps calculated with MATLAB™ and smoothed (Figure 81) at different resolutions. Mapping the C_{SP} allow to evaluate his value for each outcrop analysed (Figure 82) and establish correlations with the GSI values. C_{SP} values that fall outside the statistical reliability range set*

for the regression (R^2 > 0.85) are few and are only associated with covered-debris areas, where the measurement error may increase. Dashed circles correspond to sampling area in Figure 82 (Franzosi et al., 2023b).

The obtained C_{SP} map shows a general decrease in rock quality moving from the lower-right to the upper-left corner of the scene (**Figure 85**, **Figure 86**.a), that corresponds to a slope sector heavily damaged by active rock slope deformation processes, in agreement with the results obtained by Agliardi et al. (2013). Smoothing processes allow to homogenize the signal all over the map, showing the average thermal response of the group, rather than of the individual block (**Figure 81**, **Figure 85**).

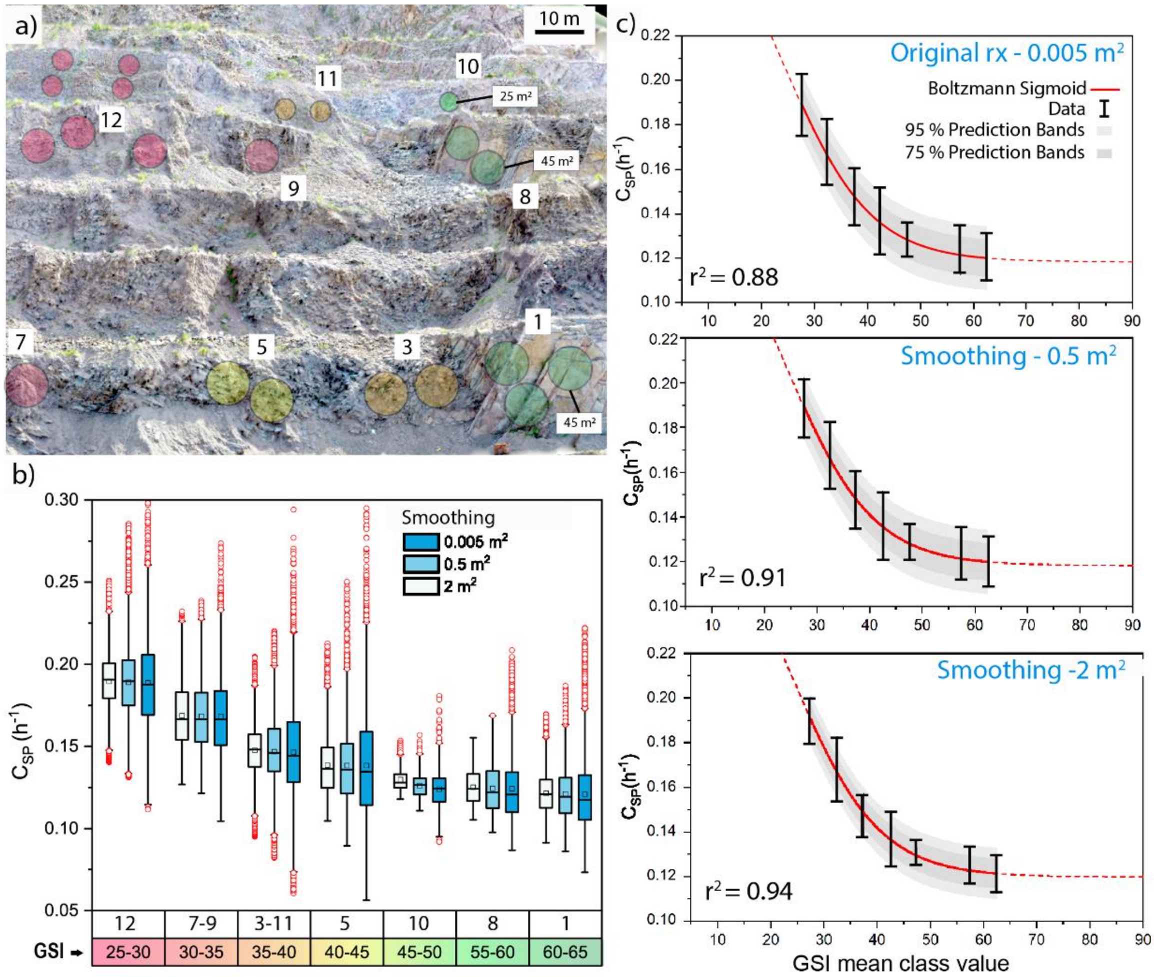

Figure 86 *a) Circular windows used to extract C_{SP} values for each outcrop; (b) boxplots of the CSP value distributions on each outcrop classified by GSI range (GSI range=5, Box=IQR 25%-75%;whiskers=1.5 IQR, red dots=outliers); (c) C_{SP} data were filtered in the IQR(25%-75%) and CSP-GSI relationship fitted with sigmoidal*

function for each smoothed C_{SP} map resolutions (red line = Boltzmann sigmoid; dark-grey area = 75% prediction band; light-grey area = 75% prediction band; r^2 = determination coefficient) (Franzosi et al., 2023b).

The inspection of the boxplots in **Figure 86**.b, reporting C_{SP} value distributions sampled for outcrops characterized by different GSI classes for different smoothing resolutions (**Figure 85**), show a significant variability of calculated C_{SP} values (in terms of interquartile range, IQR). This variability is larger for outcrops in rock mass sectors characterized by a wide distribution of block volumes (e.g. outcrops 5-3-11; **Figure 86**.b) corresponding with the intermedium GSI values (i.e between 45 and 35). Smoothing processing clearly reduces this variability (**Figure 85**, **Figure 86**.b)

The relation suggest that C_{SP} values increase for decreasing GSI value (**Figure 86**.a-b), corresponding with higher fracture intensity and lower rock mass quality classes, in close agreement with previous laboratory-scale findings (Franzosi et al., 2023a).

5.3.3 GSI-CSP relationship

The clear qualitative correlation between C_{SP} and GSI logs showed in **Figure 86**.b motivated the search for a quantitative relationship linking the cooling behaviour of rock masses with their geomechanical quality for practical applications. As explained below, we fitted a Boltzmann sigmoid function to our experimental data at different smoothing resolutions (**Figure 86**.c).

The limit asymptotic values of the function were constrained through experimental measurements of the C_{SP} values for end members of rock mass quality in the scene captured by IRT (**Figure 86**.a). In particular, the upper limit of the sigmoid (**Figure 86**.c) was set to account for C_{SP} data corresponding to debris accumulation zones, i.e. rock mass completely decomposed to granular soils (**Figure 85**), while the lower was fixed following the clearly asymptotic trend of the outcrops with highest GSI classes (**Figure 86**.c). C_{SP}-GSI relationships obtained by non-linear regression of the sigmoidal model relationships (**Figure 86.c**) show an increasing goodness of fit (i.e. higher coefficient of determination, narrower prediction bands) for increasingly smoothed C_{SP} datasets that incrementing the resolution sampling of C_{SP} map (**Figure 81**).

We adopted model with the best goodness-of-fit statistics (resampling at 2 m2, **Figure 86.c**, **Figure 87**) in the form of the following empirical equation:

$$C_{SP} = 0{,}12 + \frac{0{,}18}{\left(1 + e^{\frac{GSI-27}{8}}\right)}$$

Equation 38

Where:

C_{SP} is the Curve Shape Parameter (h^{-1})

GSI is the Geological Strength Index (-)

Equation 38 represents the best-fit empirical correlation equation (**Figure 87**), that allows estimating the local value of the GSI of a rock mass based on its cooling behavior averaged within a sampling area of 2 m^2 (**Figure 81**, **Figure 85**, **Figure 86**.c). This value represents the most correct threshold for returning a C_{SP} map that considers the range of block sizes in rock mass portion and at the same time does not lose spatial representativeness (**Figure 81**). Performing tests, sigmoid model was fitted to experimental data in the GSI range 25-65 (**Figure 87**) and extrapolated towards GSI values < 25 (disintegrated rock masses transitioning to granular materials, i.e upper limit of cooling speed) and > 65 (high quality blocky rock masses passing to intact rock, i.e lower limit of cooling speed). This relationship, characterized by the occurrence of upper and lower plateaus (**Figure 87**), reflects the thermal signature of a transition between "equivalent continuum" granular materials and intact rock, passing through "discontinuum" media whose thermal behaviour is controlled by discrete networks of fractures bounding radiant rock blocks of increasing size (Franzosi et al. 2023a). This kind of dependence of C_{SP} on the GSI is in close agreement with those observed in the literature for other physical parameters like the deformation modulus (Cai et al., 2004) and the P-wave velocity (Agliardi et al., 2016).

In a practical predictive perspective, the proposed empirical correlation between C_{SP} (i.e. the measured variable) and GSI (i.e. the variable to be predicted) is expected to be more discriminant for rock masses characterized by GSI in the range 25-55, i.e. the most critical to slope and mining engineering applications, and seems to loose the ability to distinguish differences beyond very high or very low quality thresholds. Considering the width of the 75% and 95% prediction bands obtained by the non-linear regression analysis, we can expect GSI prediction accuracies within a value of 10, i.e. comparable to common field estimates (Hoek & Brown, 1997; Evert Hoek et al., 1998; Cai et al., 2004) through the inversion of **Equation 38**:

$$GSI = 8ln\left[\left(\frac{0,18}{C_{SP} - 0,12}\right) - 1\right] + 27$$

Equation 39

Where:

C_{SP} is the Curve Shape Parameter (h^{-1})

GSI is the Geological Strength Index (-)

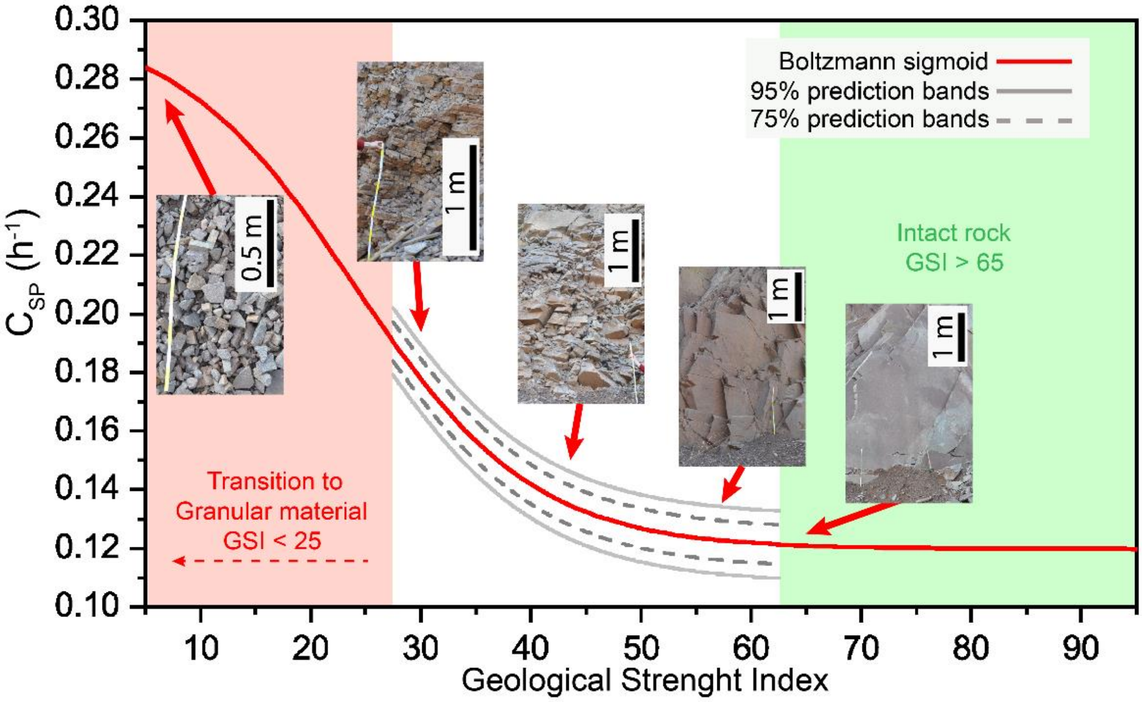

Figure 87 *Empirical relationship between C_{SP} and GSI values fitted with a sigmoidal function (equation 38), using the C_{SP} map resampled at $2m^2$. The asymptotes of the model are represented by the collected data representative of the intact rock (green-dashed area) and the debris, representative of the last step of the transition from rock-mass to granular material with the lower level of GSI (< 10). In the transition zone (white area) we can observe some inset of the outcrops (Figure 73) that clearly show the differences in fracturing state, quality and block-size (Franzosi et al., 2023b).*

5.3.4 Automated slope-scale GSI mapping

For each pixel of the smoothed C_{SP} map 2 m^2(**Figure 85**), **Equation 39** provide a translation of C_{SP} values into corresponding GSI, thus providing spatially distributed maps the GSI at slope scale (**Figure 88**) and different levels of prediction (**Figure 87**).

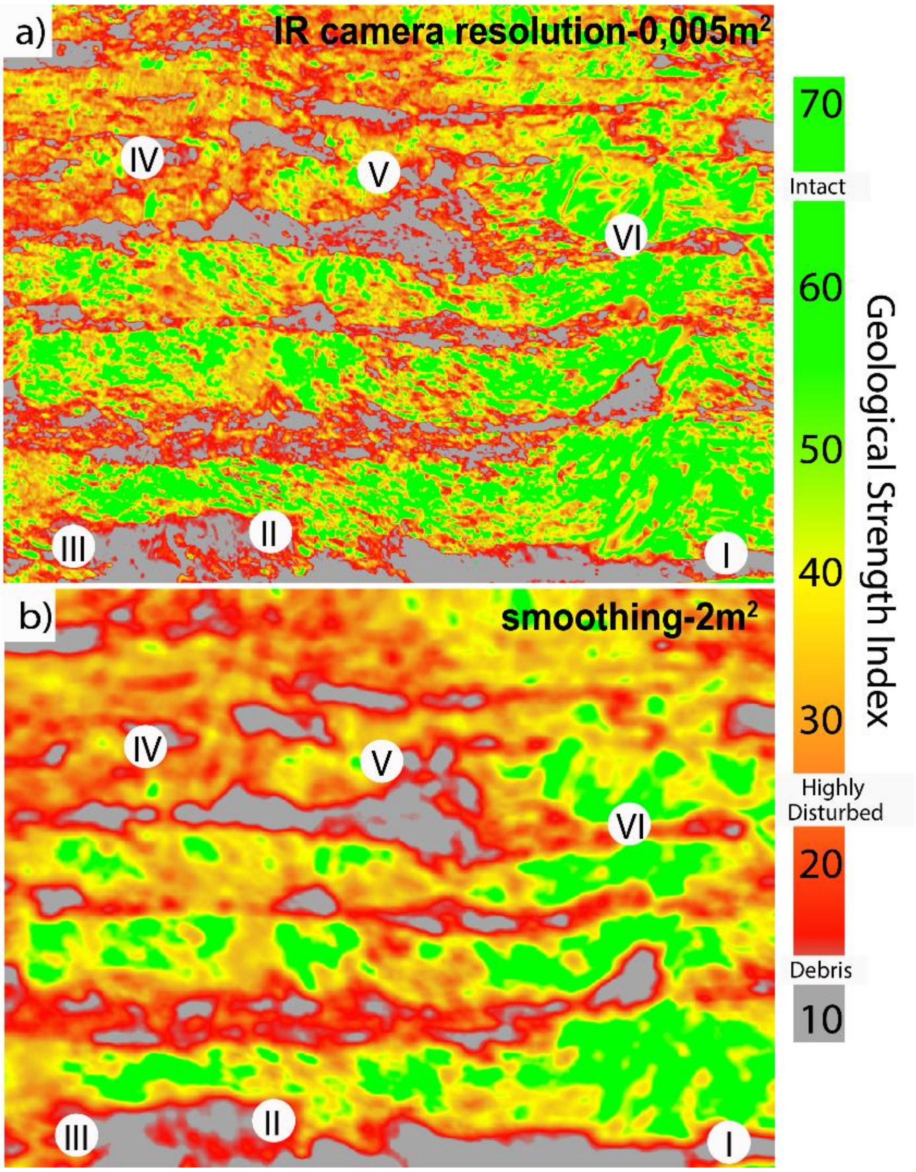

Figure 88 *The figure shows the GSI maps, at slope-scale of the quarry, obtained by applying Eq. 39 to the C_{SP} maps (Figure 85), at different resolutions. In (a) and (b), the clear distinction between the debris at the foot of the steps and the rock-mass outcrops can be observed. Using the insets (I-VI in reference to Figure 89 the mapped GSI values can be compared with the reference quality sectors (Franzosi et al., 2023b).*

As can be seen in **Figure 88** the debris is visibly highlighted (GSI<15, grey band) by the outcrops of the rock mass designed by quarry steps. This allows to realistically predict the spatial distribution of GSI values over the wide surveyed scene. In agreement with field observation (**Figure 83**, **Figure 88**, **Figure 89**), predicted GSI values vary in the range 25-65. Observing the zones characterized by intermediate GSI values (e.g II in **Figure 88-Figure 89**), variability is greater in the areas where the distribution of block-size is widest (**Figure 83**, **Figure 88**.a) in which also acquisition disturbances may increase (experimental noise, 3D geometry, rock cavities). This character is strongly present in **Figure 88**.a but diminishes its effect using maps subjected to homogenization through smoothing procedures (**Figure 85**, **Figure 88**.b) reaching the segmentation of sectors identified by sharp changes in rock mass quality. **Figure 88** provide a slope-scale quality mapping in agreement with the gravitative processes highlighted by previous studies (Agliardi et al., 2013) and field evidences showed in **Figure 89**.

Figure 89 *Examples of outcrops of the slope covered by the analyses clearly show the wide quality range of the material, which varies from extremely intact (I; VI) to strongly disturbed and damaged (III; V) reaching the appearance of disintegrated material (IV). In this transition, the rock mass exhibits strongly discontinuous sectors characterized by wide variability in block size (II) (Franzosi et al., 2023b).*

5.4 Discussion of rock-mass scale investigation results

A reliable assessment of rock mass structure, engineering quality and hydro-mechanical properties is a key aspect in rock slope engineering and mining application, including the design of open-pit mine and engineered slopes, slope stability analysis and the characterization of both inherited and induced states of rock damage in slopes (Hoek & Brown, 1997; Pine & Harrison, 2003; Wyllie & Mah, 2004; Brideau et al., 2009; Agliardi et al., 2013). Starting from a robust theoretical framework and laboratory experimental investigation, we were able to explore the potential of the innovative IRT technique in predictive studies of the fracture state of rock mass. To do this, it was necessary to export the experience, theoretical aspects, and experimental approach developed in the laboratory (Franzosi et al., 2023a) to the *in situ* scale, through the characterization of the cooling behavior of rock mass outcrops and on the development of a shape indicator (C_{SP}) of cooling curves as a function of fracturing.

We based our approach to the problems on a systematic, sequential solution of the main upscaling issues, including: a) definition of suitable rock mass quality descriptors, b) scale effects affecting the definition of fractured rock masses as “continua” vs “discontinua” within a given sampling region (i.e. slope sector, sampling window/outcrop, remote sensing pixel); c) environmental factor and disturbances controlling the applicability of Infrared Thermography to rock mass characterization in outdoor settings, and d) reconstruction and modelling of experimental cooling curves acquired in outdoor, unconstrained environmental conditions.

The correlations observed in **Chapter 5** are based on quantitative descriptors of unbiased fracturing, which by nature are not applicable to many *in situ* contexts especially the one selected in this paper. The response between rock mass fracturing and cooling behavior that has been highlighted in several pioneering papers (Teza et al., 2012; Mineo et al., 2015; Pappalardo et al., 2016) is reconnected to the average reference block size of the rock volume, which in turn is closely related to the intensity of fracturing in the first degree (to which are secondarily added the effects due to air circulation and fracture opening, (Franzosi et al., 2023a). In our study we selected an empirical descriptor of rock mass quality such as the GSI, which is widely used in engineering applications (Evert Hoek et al., 1998; Marinos & Hoek, 2000; Cai et al., 2004; Evert Hoek & Brown, 2019), extremely versatile in different geological conditions and on site that don't allow systematic discontinuities surveys. His strong link with reference block size (Cai et al., 2004) is highlighted in a context characterized by an extremely homogeneous and mono-lithological level of material alteration such as the Mount Gorsa quarry (Agliardi et al., 2013).

The results of the surveys carried out on the accessible outcrops (**Figure 73**, **Figure 83**) certified the wide range of GSI of the rock mass already described by (Agliardi et al., 2013) highlighting the great influence of the intensity of the fracture network respect to the variability of the degree of alteration of the rock material (**Figure 83**).

At the same time, these results showed that the portions of the rock mass characterized by intermediate GSI values were characterized by blocks with rather variable sizes, evidence that made it necessary to adopt analysis and smoothing/sampling techniques that considered the average thermal response of the rock mass portion, both at the scale of the individual block (**Figure 81**) such as at the scale of benches (i.e outcrop window, **Figure 82**).

In order to reduce typical disturbances on IRT acquisition in outdoor settings, we built our experimental approach that allowed us to develop a practical surveying workflow aimed at the specific purpose (**Figure 74**, night time-laps survey and extraction of cooling curves in the absence of solar forcing); developing an innovative experimental method **Figure 76**) to characterize so as to parameterize, in a site-specific manner, the empirical relationship (SDRM, **Equation 34**) that can be used to calibrate and correct (**Figure 77**, **Figure 78**) raw IR-temperature data acquired in outdoor settings.

Our method allows the extraction and parametric modelling of corrected cooling curves and their synthetic description only dependent by the cooling path that rock-mass outcrops at different qualities follow in the same scene. The proposed methodology, despite the variability of the uncontrolled environmental conditions, allow to export the C_{SP} approach used in (Franzosi et al., 2023a) (**Figure 79**) thus maintaining the theoretical link of the thermal response with the reference block size as a direct parametrization of theory in a semi-empirical way.

Using high-resolution and accurate camera, purifying the data from noise and parameterizing the shape of the cooling curves we demonstrate that IRT is significantly applicable to the *in situ* practical characterization of rock mass quality (**Equation 38**, **Figure 87**).

In this study, we have proposed a practical workflow, from the design and execution phase of the survey to the processing and mapping phase, which stands as the basis for an operational methodology for characterizing rock mass quality. The proposed methodology has several strengths as it is contactless (using ground-based calibration points, **Figure 73**, **Figure 83**), physically based and spatially distributed. It allows analyzing the spatial patterns and temporal trends or rock mass cooling over large areas (**Figure 85**, **Figure 88**), and automatically provides continuous maps of C_{SP} and GSI that are explicitly related to specific averaging spatial domains (i.e. scales). In addition, our methodology doesn't need to carry out the time-consuming workflow of complete fracture network characterization (i.e. individual fracture identification and mapping, spacing analysis and the estimation of fracture density), required by traditional rock mass characterization even using remotely-sensed 3D point clouds.

Beside its strengths and innovative character, the approach also has limitations. The analysis allows only a superficial assessment of the quality of the rock mass. The exposure and morphology of the site can be challenging for IRT data acquisitions/processing and are only partially solved through geometric environmental corrections (**Figure 76**) and the choice of specific time windows (**Figure 79**). In fact, not all disturbance factors can be identified, so discrimination of small variations in GSI can be difficult due to experimental noise. Generally, is important to highlight that the approach needs for site-specific parameterization anyway; and can meet possible difficulties in contexts with different lithologies or strong alteration; applying our method to rock masses characterized by different lithological and physico-chemical conditions would require subdividing the study domain in homogeneous sub-domains and a careful calibration and results interpretation.

Given all these considerations, our methodology turns out to be reproducible at different scales and test sites, making it particularly versatile to future implementations through dataset enrichment, strengthening of predictive relationships and engineering of the analytical process. Our paper proposes a method but also an innovative workflow dedicated to characterizing the quality of rock mass that allows rapid assessment of rock masses geomechanical properties, potentially useful in slope stability-related hazard and risk characterization for wide-ranging engineering problems.

6 General discussion and final remarks

Reliable assessing the state of rock fractures is essential for quantifying the geo-hydromechanical properties of rocks, crucial aspects both in natural and engineering problems. However, this task is challenging due to the inherent variability in fracture networks, which are both scale-dependent and heterogeneous, and influenced by statistical biases (orientation and size). In our study, we explored the impact of rock volume fracturing on the cooling process and, consequently, the thermal response of rock materials subjected to thermal forcing for rock fracturing state characterization.

In order to develop an innovative methodology, we identified a remote sensing technique such as Infra-Red Thermography (IRT) to analyze the thermal behavior of the medium and characterize it quantitatively and in a spatially distributed way.

We verified the applicability of the IRT technique in the laboratory approaching the topic of the thermal response of small, fractured rock volumes, highlighting in an innovative way that the ambivalent "continuum vs discontinuum" thermal behavior of fractured rocks is strongly influenced by the fracturing style. Starting from this consideration, we developed a predictive methodology physically based on modeling and parameterization of measured cooling curves that can provide a parameter (Curve Parameter, C_{SP}) empirically related with unbiased fracturing metrics of fractured rock samples computed using Micro-CT technique (P_{33}, P_{32}). Compared to previous literature, our methodology results innovative and does not simply analyze the experimental curves in terms of velocity (Cooling Rate Index, CRI; Pappalardo et al. 2016, Mineo et al., 2016) but finds a synthetic descriptor of cooling behavior correlated with the physical size of the elemental volume (i.e. *rock-block*) isolated from the fractures, suggesting its predictive use in larger-scale contexts. Our results, although not directly applicable to *in situ* fractured rock masses due to different fracture network characteristics on sample and outcrop scales, lay the foundations to upscale our methodology to field conditions in a selected natural laboratory (Mt. Gorsa quarry, TN, Italy).

Upscaling the technique in situ (i.e. *rock mass-scale*), request dealing with the problems associated with both quantifying in situ fracturing and the problems associated with applying the IRT technique in external contexts, systematically resolving the main issues.

In fact, unbiased fracturing descriptors used in laboratory (P_{32},P_{33}), by their nature are not applicable to many *in situ* contexts especially the one selected in this study, while the poor accessibility of the slope and the extreme degree of damage limit the classic in situ sampling techniques to the point of making them inapplicable (Zhang & Einstein, 1998; Mauldon et al., 2001). We selected an empirical rock-mass quality index such as the GSI, that can be applied to an extremely wide range of rock types, heterogeneity and damage conditions using a widely used, mono parametric approach, intrinsically independent on water content. The transition from fracturing indices in laboratory to the use of GSI involves a loss of connection with the issue of fracture opening, which in previous laboratory experience had proven to be an important player within the thermal response of rock samples, influencing the convection process. At the same time, in the laboratory we also noticed that the temperatures of open fractures are different from those of intact rock and that this effect can mask modify the IRT signal if not filtered. Given the resolution of the IRT acquisition at Monte Gorsa, we are not able to distinguish the effect of the openings of the individual fractures, but it remains an important topic that could be in future investigated at a laboratory scale (i.e. carrying out experiments with rock cubes at different distances to simulate less or open fractures) and in situ (i.e. carrying out multi-scale IRT measurements increasing range on a single outcrop).

Furthermore IRT measures are subject to different kind of controlling factors, that can be considered less influent in laboratory acquisition but could became considerable in outdoor measurements, especially regarding large scale problems. Starting from our experimental observations and from the observations suggested by some authors (Spampinato et al., 2011; Guerin et al., 2019; Sass et al., n.d.), we explored the topic of the calibration of outdoor IRT measurements and how the complex morphology of outcrops can influence the latter. That is why we derived through an experimental methodology (starting from theory of IRT principles) an innovative methodology for calibrating IRT data that is also applicable to more general contexts, although we can only suggest as site-specific for our case study, that clearly represents an innovation in the use of outdoor IRT measurements on complex 3D natural outcrop and was never explored by previous literature (Teza et al., 2012; Pappalardo et al., 2016; Grechi et al., 2021).

Through upscaling we introduced a practical/operative workflow from survey design and execution to thermal data processing and mapping. It enables, through an original tool, the analysis of spatial patterns and temporal trends in rock mass cooling over extensive areas and automatically generates continuous maps of C_{SP} and GSI that are explicitly linked to specific spatial domains or scales, taking full advantage of the spatially distributed nature of the IRT technique on rock faces in relation to previous studies (Pappalardo et al., 2016). The introduction of the tool in this context becomes essential because it involves complex analysis of spatially distributed data. In our previous laboratory work (**Chapter 4**), our primary focus was on obtaining averaged responses from relatively small and well-defined samples. However, the current situation presents us with a vast dataset characterized by an unknown and variable distribution. Consequently, the development of a tool to address these challenges has become an important development. Through the relationship founded between C_{SP} and GSI, this workflow serves as a predictive contactless operational method for in situ assessing of rock-mass quality. The methodology proposed is based on the interaction of the solar forcing with the rocky slope, so it can only be considered as a characterization of the quality of the shallower portion of the rock-mass, which does not always reflect the deeper fracturing state conditions as observed by Fiorucci et al. 2018.

It is also important to highlight that our methodology eliminates the need for the time-consuming process of characterizing the complete fracture network, which imply a rather complex processing chain that requires individual fracture identification and mapping, spacing analysis and the estimation of fracture density, that must eventually be correlated to GSI value using similar empirical approaches, even when utilizing remotely-sensed 3D point clouds and could became not applicable to extremely fractured rock domains. This aspect reflects also the relationships founded (laboratory and *in situ*) at different scales between thermal response and fracturing degree emphasize the different nature of the fracturing descriptors (also highlighted in the theoretical aspects of the transition from continuous to discontinuous). Quantitative fracture abundance metrics are linear (intensity) or dimensionless (porosity) ratios, while Geological Strength Index is a parameter that goes to saturation (from intact rock to granular medium; Agliardi et al. 2016). In fact, while fracturing metrics correlate linearly so it is easier to calibrate their relationship with C_{SP}, but *in situ* are difficult to obtain (using DFN approach), GSI is easy to evaluate and versatile (representative of the continuous-discontinuous-continuous transition nature of fractured medium) at the same time more challenging to site-calibration as it correlates using a sigmoidal function with C_{SP}.

The approach developed in the laboratory and applied in situ is extremely innovative, but at the same time requires future improvements for correct wide-ranging application and in different geological contexts. In particular, the empirical relationships found between the C_{SP} and the GSI would be strengthened and better defined by expanding the dataset of experimental measurements in different application contexts, with different lithologies and slope exposure characteristics.

In the case of Monte Gorsa taken into consideration in this study, we observe for usefulness aquarry face with a homogeneous lithology, and a similar degree of rock weathering. For this reason, it was possible to assume a constant emissivity value, but in cases where the rock mass was composed of two or more lithologies (or strong differences in weathering), it would be necessary to highlight the different sectors, producing an emissivity map that can be used in the calibration process automatic data. Furthermore, from a practical point of view, the IRT data calibration methodology is based on the empirical model of the SDRM, which is site-specific and must be parameterized for environmental conditions, such as the different T_{sky} or air temperature, that depends on the cloud cover. In general, where possible, it would be advisable to place a spherical reflector like the one used in the experiment presented in **Figure 76** within the scene captured by the IR camera, in order to obtain a correct SDRM model for each acquisition.

Our work has gone through various stages of the experimental process and at different scales, addressing theoretical, methodological and application issues in an innovative way.

The work suggests possibilities for expanding and developing the potential of the methodology conceived for different purposes such as supporting the characterization of the mechanical or hydraulic properties of rock masses in quarries or underground excavations, while being able to provide the perturbation necessary to measure a response thermal of the rock volume. Further future applications of the methodology may include rockfall risk analysis, through applications that investigate the identification of unstable volumes (i.e possible individual block size characterization) such as characterization of rock bridges extent and thickness.

In conclusion, our developed methodology focuses on rapid remote assessment of geomechanical properties of rock masses using IRT, but has the potential to offer valuable insights into the risk associated with slope stability in a wide range of engineering challenges.

References

Abellán, A., Oppikofer, T., Jaboyedoff, M., Rosser, N. J., Lim, M., & Lato, M. J. (2014). Terrestrial laser scanning of rock slope instabilities. Earth Surface Processes and Landforms, 39(1), 80–97. https://doi.org/10.1002/esp.3493

Agisoft, L. L. C. (2018). Photoscan professional edition. St. Petersburg: Agisoft.

Agliardi, Dobbs, M. R., Zanchetta, S., & Vinciguerra, S. (2017). Folded fabric tunes rock deformation and failure mode in the upper crust. Scientific Reports, 7(1), 1–9. https://doi.org/10.1038/s41598-017-15523-1

Agliardi, F., Crosta, G. B., Meloni, F., Valle, C., & Rivolta, C. (2013). Structurally-controlled instability, damage and slope failure in a porphyry rock mass. Tectonophysics, 605, 34–47. https://doi.org/10.1016/j.tecto.2013.05.033

Agliardi, F., Sapigni, M., & Crosta, G. B. (2016). Rock Mass Characterization by High-Resolution Sonic and GSI Borehole Logging. Rock Mechanics and Rock Engineering, 49(11), 4303–4318. https://doi.org/10.1007/s00603-016-1025-x

Agliardi, Zanchetta, S., & Crosta, G. B. (2014). Fabric controls on the brittle failure of folded gneiss and schist. Tectonophysics, 637, 150–162. https://doi.org/10.1016/j.tecto.2014.10.006

Baecher, G. B. (1983). Statistical analysis of rock mass fracturing. Journal of the International Association for Mathematical Geology, 15, 329–348.

Baghbanan, A., & Jing, L. (2008). Stress effects on permeability in a fractured rock mass with correlated fracture length and aperture. International Journal of Rock Mechanics and Mining Sciences, 45(8), 1320–1334.

Bakulin, A., Grechka, V., & Tsvankin, I. (2000). Estimation of fracture parameters from reflection seismic data—Part II: Fractured models with orthorhombic symmetry. Geophysics, 65(6), 1803–1817.

Baroň, I., Bečkovský, D., & Míča, L. (2014). Application of Infrared thermography for mapping open fractures in deep-seated rockslides and unstable cliffs. Landslides, 11, 15–27.

Barreira, E., & de Freitas, V. P. (2007). Evaluation of building materials using Infrared thermography. Construction and Building Materials, 21(1), 218–224. https://doi.org/10.1016/j.conbuildmat.2005.06.049

Barton, N. (1973). Review of a new shear-strength criterion for rock joints. Engineering Geology, 7(4), 287–332.

Barton, N. (2007). Rock mass characterization for excavations in mining and civil engineering. Proceedings of the International Workshop on Rock Mass Classification in Underground Mining, 3–14.

Barton, N., Lien, R., & Lunde, J. (1974). Engineering classification of rock masses for the design of tunnel support. Rock Mechanics, 6, 189–236.

Barton, N. (1978). Recent experiences with the Q-system of tunnel support design.

Bathe, K. (2007). Finite element method. Wiley Encyclopedia of Computer Science and Engineering, 1–12.

Bellian, J. A., Kerans, C., & Jennette, D. C. (2005). Digital outcrop models: applications of terrestrial scanning lidar technology in stratigraphic modeling. Journal of Sedimentary Research, 75(2), 166–176.

Bergman, T. L., Bergman, T. L., Incropera, F. P., Dewitt, D. P., & Lavine, A. S. (2011). Fundamentals of heat and mass transfer. John Wiley & Sons.

Bieniawski, Z. T. (1993). Classification of rock masses for engineering: the RMR system and future trends. In Rock Testing and Site Characterization (pp. 553–573). Elsevier.

Bistacchi, A., Mittempergher, S., & Martinelli, M. (2022). Digital outcrop model reconstruction and interpretation. 3D Digital Geological Models: From Terrestrial Outcrops to Planetary Surfaces, 11–32.

Brideau, M.-A., Yan, M., & Stead, D. (2009). The role of tectonic damage and brittle rock fracture in the development of large rock slope failures. Geomorphology, 103(1), 30–49.

Buckley, S. J., Howell, J. A., Enge, H. D., & Kurz, T. H. (2008). Terrestrial laser scanning in geology: data acquisition, processing and accuracy considerations. Journal of the Geological Society, 165(3), 625–638.

Cai, Kaiser, P. K., Uno, H., Tasaka, Y., & Minami, M. (2004). Estimation of rock mass deformation modulus and strength of jointed hard rock masses using the GSI system. International Journal of Rock Mechanics and Mining Sciences, 41(1), 3–19.

Cai, X., Zhou, Z., Tan, L., Zang, H., & Song, Z. (2020). Water Saturation Effects on Thermal Infrared Radiation Features of Rock Materials During Deformation and Fracturing. Rock Mechanics and Rock Engineering. https://doi.org/10.1007/s00603-020-02185-1

Caliò, D., Mineo, S., & Pappalardo, G. (2023). Digital Rock Mass Analysis for the Evaluation of Rockfall Magnitude at Poorly Accessible Cliffs. Remote Sensing, 15(6), 1515.

Clark, M. R., McCann, D. M., & Forde, M. C. (2003). Application of Infrared thermography to the non-destructive testing of concrete and masonry bridges. NDT and E International, 36(4), 265–275. https://doi.org/10.1016/S0963-8695(02)00060-9

Clauser, C., & Huenges, E. (1995). Thermal conductivity of rocks and minerals. Rock Physics and Phase Relations: A Handbook of Physical Constants, 3, 105–126.

De Dreuzy, J. R., Méheust, Y., & Pichot, G. (2012). Influence of fracture scale heterogeneity on the flow properties of three-dimensional discrete fracture networks (DFN). Journal of Geophysical Research: Solid Earth, 117(11), 1–21. https://doi.org/10.1029/2012JB009461

Deere, D. U., & Deere, D. W. (1967). The Rock Ouality Designation (ROD) Index.

Deere, D. U., & Miller, R. P. (1966). Engineering classification and index properties for intact rock. National Technical Information Service Springfield, VA, USA.

Dershowitz, W.S & Herda, H. (1992). Interpretation of fracture spacing and intensity. The 33rd US Symposium on Rock Mechanics (USRMS).

Dershowitz, W., & Miller, I. (1995). Dual porosity fracture flow and transport. Geophysical Research Letters, 22(11), 1441–1444.

Dershowitz, W S. (1998). FracMan interactive discrete feature data analysis, geometric modeling and exploration simulation. User Documentation.

Dershowitz, W. S. (1984). Rock joint systems. Massachusetts Institute of Technology.

Dorn, C., Linde, N., Doetsch, J., Le Borgne, T., & Bour, O. (2012). Fracture imaging within a granitic rock aquifer using multiple-offset single-hole and cross-hole GPR reflection data. Journal of Applied Geophysics, 78, 123–132.

Eberhardt, E, Stead, D., & Coggan, J. S. (2004). Numerical analysis of initiation and progressive failure in natural rock slopes—the 1991 Randa rockslide. International Journal of Rock Mechanics and Mining Sciences, 41(1), 69–87.

Eberhardt, E. (2012). The Hoek – Brown Failure Criterion. 981–988. https://doi.org/10.1007/s00603-012-0276-4

Edelbro, C. (2004). Evaluation of rock mass strength criteria. Luleå tekniska universitet.

Einstein, H. H., & Dershowitz, W. S. (1990). Tensile and shear fracturing in predominantly compressive stress fields - a review. 29, 149–172.

Fiorucci, M., Marmoni, G. M., Martino, S., & Mazzanti, P. (2018). Thermal response of jointed rock masses inferred from Infrared thermographic surveying (Acuto test-site, italy). Sensors (Switzerland), 18(7). https://doi.org/10.3390/s18072221

Fisher, N. I., Lewis, T., & Embleton, B. J. J. (1993). Statistical analysis of spherical data. Cambridge university press.

Flir Corporation. (n.d.). User's manual FLIR T10xx series.

Fossen, H. (2016). Structural geology. Cambridge university press.

Francioni, M., Simone, M., Stead, D., Sciarra, N., Mataloni, G., & Calamita, F. (2019). A new fast and low-cost photogrammetry method for the engineering characterization of rock slopes. Remote Sensing, 11(11), 1267.

Franzosi, F., Casiraghi, S., Colombo, R., Crippa, C., & Agliardi, F. (2023a). Quantitative Evaluation of the Fracturing State of Crystalline Rocks Using Infrared Thermography. Rock Mechanics and Rock Engineering, 0123456789. https://doi.org/10.1007/s00603-023-03389-x

Franzosi, F., Crippa, C., Derron, M.-H., Jaboyedoff, M., & Agliardi, F. (2023b). Slope-Scale Remote Mapping of Rock Mass Fracturing by Modeling Cooling Trends Derived from Infrared Thermography. Remote Sensing, 15(18), 4525.

Frodella, W., Gigli, G., Morelli, S., Lombardi, L., & Casagli, N. (2017). Landslide mapping and characterization through Infrared Thermography (IRT): Suggestions for a methodological approach from some case studies. Remote Sensing, 9(12). https://doi.org/10.3390/rs9121281

Gigli, G., & Casagli, N. (2011). Semi-automatic extraction of rock mass structural data from high resolution LIDAR point clouds. International Journal of Rock Mechanics and Mining Sciences, 48(2), 187–198. https://doi.org/10.1016/j.ijrmms.2010.11.009

Gischig, V. S., Giardini, D., Amann, F., Hertrich, M., Krietsch, H., Loew, S., Maurer, H., Villiger, L., Wiemer, S., & Bethmann, F. (2020). Hydraulic stimulation and fluid circulation experiments in underground laboratories: Stepping up the scale towards engineered geothermal systems. Geomechanics for Energy and the Environment, 24, 100175.

Grasmueck, M. (1996). 3-D ground-penetrating radar applied to fracture imaging in gneiss. Geophysics, 61(4), 1050–1064.

Grechi, G., Fiorucci, M., Marmoni, G. M., & Martino, S. (2021). 3D thermal monitoring of jointed rock masses through Infrared thermography and photogrammetry. Remote Sensing, 13(5), 957.

Gu, J.-C., Rice, J. R., Ruina, A. L., & Simon, T. T. (1984). Slip motion and stability of a single degree of freedom elastic system with rate and state dependent friction. Journal of the Mechanics and Physics of Solids, 32(3), 167–196.

Gudmundsson, A. (2011). Rock fractures in geological processes. Cambridge University Press.

Guerin, A., Jaboyedoff, M., Collins, B. D., Derron, M. H., Stock, G. M., Matasci, B., Boesiger, M., Lefeuvre, C., & Podladchikov, Y. Y. (2019). Detection of rock bridges by Infrared thermal imaging and modeling. Scientific Reports, 9(1), 1–19. https://doi.org/10.1038/s41598-019-49336-1

Harthong, B., Scholtès, L., & Donzé, F.-V. (2012). Strength characterization of rock masses, using a coupled DEM–DFN model. Geophysical Journal International, 191(2), 467–480.

Ho-Le, K. (1988). Finite element mesh generation methods: a review and classification. Computer-Aided Design, 20(1), 27–38.

Hodgetts, D. (2013). Laser scanning and digital outcrop geology in the petroleum industry: A review. Marine and Petroleum Geology, 46, 335–354.

Hoek, & Brown, E. T. (1997). Practical estimates of rock mass strength. International Journal of Rock Mechanics and Mining Sciences, 34(8), 1165–1186.

Hoek, & Diederichs, M. S. (2006). Empirical estimation of rock mass modulus. International Journal of Rock Mechanics and Mining Sciences, 43(2), 203–215.

Hoek, E. (1983). Strength of jointed rock masses. 3, 187–223.

Hoek, Evert, & Bray, J. D. (1981). Rock slope engineering. CRC press.

Hoek, Evert, & Brown, E. T. (1980). Empirical strength criterion for rock masses. Journal of the Geotechnical Engineering Division, 106(9), 1013–1035.

Hoek, Evert, & Brown, E. T. (1988). The Hoek-Brown failure criterion–a 1988 update. Proc. 15th Can. Rock Mech. Symp, Toronto, Canada.

Hoek, Evert, & Brown, E. T. (2019). The Hoek–Brown failure criterion and GSI–2018 edition. Journal of Rock Mechanics and Geotechnical Engineering, 11(3), 445–463.

Hoek, Evert, Carranza-Torres, C., & Corkum, B. (2002). Hoek-Brown failure criterion-2002 edition. Proceedings of NARMS-Tac, 1(1), 267–273.

Hoek, Evert, Kaiser, P. K., & Bawden, W. F. (1995). Support of underground excavations in hard rock. CRC Press.

Hoek, E., Marinos, P., & Benissi, M. (1998). Applicability of the Geological Strength Index (GSI) classification for very weak and sheared rock masses. The case of the Athens Schist Formation. Bulletin of Engineering Geology and the Environment, 57, 151–160.

Howell, I. (2018). PhD thesis FABRICATION OF HIGH REFRACTIVE INDEX, PERIODIC, COMPOSITE NANOSTRUCTURES FOR PHOTONIC AND SENSING APPLICATIONS. November. https://scholarworks.umass.edu/dissertations_2

Hudson, J A, & Priest, S. D. (1983). Discontinuity frequency in rock masses. International Journal of Rock Mechanics and Mining Sciences & Geomechanics Abstracts, 20(2), 73–89.

Hudson, John A, & Harrison, J. P. (2000). Engineering rock mechanics: an introduction to the principles. Elsevier.

Ibarra-Castanedo, C., Sfarra, S., Klein, M., & Maldague, X. (2017). Solar loading thermography: Time-lapsed thermographic survey and advanced thermographic signal processing for the inspection of civil engineering and cultural heritage structures. Infrared Physics & Technology, 82, 56–74.

ISPRA. (2009). Carta Geologica d'Italia – 1:50.000 Progetto CARG: modifiche ed integrazioni al quaderno n. 1/1992. Servizio Geologico d'Italia, Quaderni Serie III, 12(3). http://www.isprambiente.gov.it/en

ISRM. (1978). Suggested methods for the quantitative description of discontinuities in rock masses. ISRM, International Journal of Rock Mechanics and Mining Sciences & Geomechanics Abstracts, 15(6), 319–368.

Jaboyedoff, M., & Derron, M.-H. (2020). Landslide analysis using laser scanners. In Developments in Earth Surface Processes (Vol. 23, pp. 207–230). Elsevier.

Jaboyedoff, M., Metzger, R., Oppikofer, T., Couture, R., Derron, M.-H., Locat, J., & Turmel, D. (2007). New insight techniques to analyze rock-slope relief using DEM and 3Dimaging cloud points: COLTOP-3D software. ARMA Canada-US Rock Mechanics Symposium, ARMA-07.

Jing, L., & Stephansson, O. (2007). Fundamentals of discrete element methods for rock engineering: theory and applications. Elsevier.

Kang, F., Zhong-Ci, S., Kang, F., & Zhong-Ci, S. (1996). Finite element methods. Mathematical Theory of Elastic Structures, 289–385.

Keller, A. (1998). High resolution, non-destructive measurement and characterization of fracture apertures. International Journal of Rock Mechanics and Mining Sciences, 35(8), 1037–1050.

Kelsey, V., Riley, S., & Minschwaner, K. (2022a). Atmospheric precipitable water vapor and its correlation with clear-sky Infrared temperature observations. Atmospheric Measurement Techniques, 15(5), 1563–1576.

Kelsey, V., Riley, S., & Minschwaner, K. (2022b). Atmospheric precipitable water vapor and its correlation with clear-sky Infrared temperature observations. Atmospheric Measurement Techniques, 15(5), 1563–1576. https://doi.org/10.5194/amt-15-1563-2022

King, M. S. (2009). Recent developments in seismic rock physics. International Journal of Rock Mechanics and Mining Sciences, 46(8), 1341–1348.

Krauland, N., Söder, P., & Agmalm, G. (1989). Determination of rock mass strength by rock mass classification—Some experiences and questions from Boliden mines. International Journal of Rock Mechanics and Mining Sciences & Geomechanics Abstracts, 26(1), 115–123.

Lai, J., Liu, B.-C., Li, H.-B., Pang, X.-J., Liu, S.-C., Bao, M., & Wang, G.-W. (2022). Bedding parallel fractures in fine-grained sedimentary rocks: recognition, formation mechanisms, and prediction using well log. Petroleum Science, 19(2), 554–569.

Landis, E. N., & Keane, D. T. (2010). X-ray microtomography. Materials Characterization, 61(12), 1305–1316.

Laslett, G. M. (1982). Censoring and edge effects in areal and line transect sampling of rock joint traces. Journal of the International Association for Mathematical Geology, 14, 125–140.

Leberl, F., Irschara, A., Pock, T., Meixner, P., Gruber, M., Scholz, S., & Wiechert, A. (2010). Point clouds. Photogrammetric Engineering & Remote Sensing, 76(10), 1123–1134.

Lisle, R. J., & Leyshon, P. R. (2004). Stereographic projection techniques for geologists and civil engineers. Cambridge University Press.

Loiotine, L., Andriani, G. F., Derron, M.-H., Parise, M., & Jaboyedoff, M. (2022). Evaluation of Infrared thermography supported by UAV and field surveys for rock mass characterization in complex settings. Geosciences, 12(3), 116.

Mandl, G. (2005). Rock joints. Springer.

Marinos, P., & Hoek, E. (2000). GSI: a geologically friendly tool for rock mass strength estimation. ISRM International Symposium.

Markel, J. (1972). The SIFT algorithm for fundamental frequency estimation. IEEE Transactions on Audio and Electroacoustics, 20(5), 367–377.

Martinelli, M., Bistacchi, A., Mittempergher, S., Bonneau, F., Balsamo, F., Caumon, G., & Meda, M. (2020). Damage zone characterization combining scan-line and scan-area analysis on a km-scale Digital Outcrop Model: The Qala Fault (Gozo). Journal of Structural Geology, 140, 104144.

Martino, J. B., & Chandler, N. A. (2004). Excavation-induced damage studies at the underground research laboratory. International Journal of Rock Mechanics and Mining Sciences, 41(8), 1413–1426.

Mauldon, M., Dunne, W. M., & Rohrbaugh Jr, M. B. (2001). Circular scanlines and circular windows: new tools for characterizing the geometry of fracture traces. Journal of Structural Geology, 23(2–3), 247–258.

Miller, R. P. (1965). Engineering classification and index properties for intact rock. University of Illinois at Urbana-Champaign.

Miller, S. M. (1983). A statistical method to evaluate homogeneity of structural populations. Journal of the International Association for Mathematical Geology, 15, 317–328.

Min, K. B., Jing, L., & Stephansson, O. (2004). Determining the equivalent permeability tensor for fractured rock masses using a stochastic REV approach: Method and application to the field data from Sellafield, UK. Hydrogeology Journal, 12(5), 497–510. https://doi.org/10.1007/s10040-004-0331-7

Mineo, S., Caliò, D., & Pappalardo, G. (2022). UAV-based photogrammetry and Infrared thermography applied to rock mass survey for geomechanical purposes. Remote Sensing, 14(3), 473.

Mineo, S., & Pappalardo, G. (2016). The Use of Infrared Thermography for Porosity Assessment of Intact Rock. Rock Mechanics and Rock Engineering, 49(8), 3027–3039. https://doi.org/10.1007/s00603-016-0992-2

Mineo, S., & Pappalardo, G. (2021). Rock emissivity measurement for Infrared thermography engineering geological applications. Applied Sciences (Switzerland), 11(9). https://doi.org/10.3390/app11093773

Mineo, S., Pappalardo, G., Rapisarda, F., Cubito, A., & Di Maria, G. (2015). Integrated geostructural, seismic and Infrared thermography surveys for the study of an unstable rock slope in the Peloritani Chain (NE Sicily). Engineering Geology, 195, 225–235. https://doi.org/10.1016/j.enggeo.2015.06.010

Mineo, S., & Pappalardo, G. (2019). Infrared Thermography presented as an innovative and non-destructive solution to quantify rock porosity in laboratory. International Journal of Rock Mechanics and Mining Sciences, 115, 99–110.

Minkina, W., & Klecha, D. (2016). Atmospheric transmission coefficient modelling in the Infrared for thermovision measurements. Journal of Sensors and Sensor Systems, 5(1), 17–23. https://doi.org/10.5194/jsss-5-17-2016

Montemagno, & Pyrak-Nolte, L. J. (1999). Fracture network versus single fractures: measurement of fracture geometry with X-ray tomography. Physics and Chemistry of the Earth, Part A: Solid Earth and Geodesy, 24(7), 575–579.

Moran, M. S. (2004). Thermal Infrared measurement as an indicator of plant ecosystem health. In Thermal remote sensing in land surface processes (pp. 256–282). CRC press.

Nesbit, P. R., & Hugenholtz, C. H. (2019). Enhancing UAV–SFM 3D model accuracy in high-relief landscapes by incorporating oblique images. Remote Sensing, 11(3), 239.

Neuman, S. P. (2005). Trends, prospects and challenges in quantifying flow and transport through fractured rocks. Hydrogeology Journal, 13, 124–147.

Oda, M., Nemat-Nasser, S., & Konishi, J. (1985). Stress-induced anisotropy in granular masses. Soils and Foundations, 25(3), 85–97.

Palmstrom, A. (2005). Measurements of and correlations between block size and rock quality designation (RQD). Tunnelling and Underground Space Technology, 20(4), 362–377. https://doi.org/10.1016/j.tust.2005.01.005

Palmstrom, A. (1982). The volumetric joint count—a useful and simple measure of the degree of rock mass jointing. International Association of Engineering Geology. International Congress. 4, 221–228.

Palmström, A. (1996). The weighted joint density method leads to improved characterization of jointing. Conference on Recent Advances in Tunnelling Technology, New Delhi.

Pappalardo, G., Mineo, S., Zampelli, S. P., Cubito, A., & Calcaterra, D. (2016). Infrared Thermography proposed for the estimation of the Cooling Rate Index in the remote survey of rock masses. International Journal of Rock Mechanics and Mining Sciences, 83, 182–196. https://doi.org/10.1016/j.ijrmms.2016.01.010

Paterson, M. S., & Wong, T. (2005). Experimental rock deformation: the brittle field (Vol. 348). Springer.

Peacock, D. C. P., Dimmen, V., Rotevatn, A., & Sanderson, D. J. (2017). A broader classification of damage zones. Journal of Structural Geology, 102, 179–192.

Pine, R. J., & Harrison, J. P. (2003). Rock mass properties for engineering design. Quarterly Journal of Engineering Geology and Hydrogeology, 36(1), 5–16.

Priest, S. D., & Hudson, J. A. (1976). Discontinuity spacings in rock. International Journal of Rock Mechanics and Mining Sciences & Geomechanics Abstracts, 13(5), 135–148.

Priest, S. D., & Hudson, J. A. (1981). Estimation of discontinuity spacing and trace length using scanline surveys. International Journal of Rock Mechanics and Mining Sciences And, 18(3), 183–197. https://doi.org/10.1016/0148-9062(81)90973-6

Priest, S. D. (1993). Discontinuity analysis for rock engineering. Springer Science & Business Media.

Rafael, R. A., L.F. Pottie, D., Leonardo, L. H., J. Cardoso Filho, B., & P. Porto, M. (2019). A directional-spectral approach to estimate temperature of outdoor PV panels. Solar Energy, 183(January), 782–790. https://doi.org/10.1016/j.solener.2019.03.049

Rawling, G. C., Goodwin, L. B., & Wilson, J. L. (2001). Internal architecture, permeability structure, and hydrologic significance of contrasting fault-zone types. Geology, 29(1), 43–46.

Ren, F., Ma, G., Fan, L., Wang, Y., & Zhu, H. (2017). Equivalent discrete fracture networks for modelling fluid flow in highly fractured rock mass. Engineering Geology, 229(September), 21–30. https://doi.org/10.1016/j.enggeo.2017.09.013

Riquelme, A. J., Abellán, A., & Tomás, R. (2015). Discontinuity spacing analysis in rock masses using 3D point clouds. Engineering Geology, 195, 185–195.

Riva, F., Agliardi, F., Amitrano, D., & Crosta, G. B. (2018). Damage-Based Time-Dependent Modeling of Paraglacial to Postglacial Progressive Failure of Large Rock Slopes. Journal of Geophysical Research: Earth Surface, 123(1), 124–141. https://doi.org/10.1002/2017JF004423

Rives, T., Razack, M., Petit, J.-P., & Rawnsley, K. D. (1992). Joint spacing: analogue and numerical simulations. Journal of Structural Geology, 14(8–9), 925–937.

Rogers, S. F., Bewick, R. P., Brzovic, A., & Gaudreau, D. (2017). Integrating photogrammetry and discrete fracture network modelling for improved conditional simulation of underground wedge stability. Deep Mining 2017: Proceedings of the Eighth International Conference on Deep and High Stress Mining, 599–610.

Rohrbaugh Jr, M. B., Dunne, W. M., & Mauldon, M. (2002). Estimating fracture trace intensity, density, and mean length using circular scan lines and windows. AAPG Bulletin, 86(12), 2089–2104.

Rottura, A., Bargossi, G. M., Caggianelli, A., Del Moro, A., Visona, D., & Tranne, C. A. (1998). Origin and significance of the Permian high-K calc-alkaline magmatism in the central-eastern Southern Alps, Italy. Lithos, 45(1–4), 329–348.

Rudnick, R. L., & Gao, S. (2003). Vol. 3: The Crust, 3.01–The Composition of the Continental Crust. Treatise on Geochemistry, 1–64.

Rutqvist, J., Rinaldi, A. P., Cappa, F., & Moridis, G. J. (2015). Modeling of fault activation and seismicity by injection directly into a fault zone associated with hydraulic fracturing of shale-gas reservoirs. Journal of Petroleum Science and Engineering, 127, 377–386.

Rutqvist, J., & Stephansson, O. (2003). The role of hydromechanical coupling in fractured rock engineering. Hydrogeology Journal, 11, 7–40.

Sagar, B., & Runchal, A. (1982). Permeability of fractured rock: Effect of fracture size and data uncertainties. Water Resources Research, 18(2), 266–274. https://doi.org/10.1029/WR018i002p00266

Salisbury, J. W., & D'Aria, D. M. (1992). Emissivity of terrestrial materials in the 8–14 μm atmospheric window. Remote Sensing of Environment, 42(2), 83–106.

Sanderson, D. J., & Zhang, X. (1999). Critical stress localization of flow associated with deformation of well-fractured rock masses, with implications for mineral deposits. Geological Society Special Publication, 155, 69–81. https://doi.org/10.1144/GSL.SP.1999.155.01.07

Sanz-Ablanedo, E., Chandler, J. H., Rodríguez-Pérez, J. R., & Ordóñez, C. (2018). Accuracy of unmanned aerial vehicle (UAV) and SfM photogrammetry survey as a function of the number and location of ground control points used. Remote Sensing, 10(10), 1606.

Sass, O., Bauer, C., Fruhmann, S., Harald, S., Kropf, F., & Gaisberger, C. (n.d.). Infrared Thermography Monitoring of Rock Faces�Potential and Pitfalls. Available at SSRN 4407790.

Schultz, R. A. (2019). Geologic fracture mechanics. Cambridge University Press.

Shanley, R. J., & Mahtab, M. A. (1974). A computer program for clustering data points on the sphere (Vol. 8624). United States Department of the Interior, Bureau of Mines.

Shannon, H. R., Sigda, J. M., Van Dam, R. L., Hendrickx, J. M. H., & McLemore, V. T. (2005). Thermal camera imaging of rock piles at the Questa Molybdenum Mine, Questa, New Mexico. Proc. 2005 National Meeting of the American Society of Mining and Reclamation, June, 19–23.

Song, Z., Zhang, Q., Zhang, Y., Wang, J., Fan, S., & Zhou, G. (2021). Abnormal precursory information analysis of the Infrared radiation temperature (IRT) before sandstone failure. KSCE Journal of Civil Engineering, 25(11), 4173–4183.

Spalla, M. I., Carminati, E., Ceriani, S., Oliva, A., & Battaglia, D. (1999). Influence of deformation partitioning and metamorphic re-equilibration on P–T path reconstruction in the pre-Alpine basement of central Southern Alps (Northern Italy). Journal of Metamorphic Geology, 17(3), 319–336.

Spampinato, L., Calvari, S., Oppenheimer, C., & Boschi, E. (2011). Volcano surveillance using Infrared cameras. Earth-Science Reviews, 106(1–2), 63–91. https://doi.org/10.1016/j.earscirev.2011.01.003

Spearman, C. (1961). The proof and measurement of association between two things.

Sturzenegger, M., & Stead, D. (2009). Close-range terrestrial digital photogrammetry and terrestrial laser scanning for discontinuity characterization on rock cuts. Engineering Geology, 106(3–4), 163–182.

Swan, A. R. H., & Sandilands, M. (1995). Introduction to geological data analysis. International Journal of Rock Mechanics and Mining Sciences and Geomechanics Abstracts, 8(32), 387A.

Terzaghi, R. D. (1965). Sources of error in joint surveys. Geotechnique, 15(3), 287–304.

Teza, G., Marcato, G., Castelli, E., & Galgaro, A. (2012). IRTROCK: A MATLAB toolbox for contactless recognition of surface and shallow weakness of a rock cliff by Infrared thermography. Computers and Geosciences, 45, 109–118. https://doi.org/10.1016/j.cageo.2011.10.022

Teza, G., Marcato, G., Pasuto, A., & Galgaro, A. (2015). Integration of laser scanning and thermal imaging in monitoring optimization and assessment of rockfall hazard: a case history in the Carnic Alps (Northeastern Italy). Natural Hazards, 76(3), 1535–1549. https://doi.org/10.1007/s11069-014-1545-1

Trommsdorff, V., Montrasio, A., Hermann, J., Müntener, O., Spillmann, P., & Gieré, R. (2005). The geological map of Valmalenco. Schweizerische Mineralogische Und Petrographische Mitteilungen, 85(1), 1–13.

Turkey, J. W. (1977). Exploratory Data Analysis, vol. 2. Addison-Wesley Publishing Company.

Usamentiaga, R., Venegas, P., Guerediaga, J., Vega, L., Molleda, J., & Bulnes, F. G. (2014). Infrared thermography for temperature measurement and non-destructive testing. Sensors (Switzerland), 14(7), 12305–12348. https://doi.org/10.3390/s140712305

Van Riel, S. (2016). Exploring the use of 3D GIS as an analytical tool in archaeological excavation practice.

Vollmer, M. (2009). Newton's law of cooling revisited. European Journal of Physics, 30(5), 1063.

Vollmer, M., & Mollmann, K. P. (2010). Advanced methods in IR imaging. Infrared thermal imaging: fundamentals, research and applications. Weinheim: Wiley-VCH Verlag.

Vollmer, M., & Möllmann, K.-P. (2018). Fundamental of Infrared Thermal Imaging. In An Automated Irrigation System Using Arduino Microcontroller (Issue 1967, pp. 2–6).

Wang, J.-A., & Park, H. D. (2002). Fluid permeability of sedimentary rocks in a complete stress–strain process. Engineering Geology, 63(3–4), 291–300.

Wang, X. (2005). Stereological interpretation of rock fracture traces on borehole walls and other cylindrical surfaces. Virginia Tech.

Wang, Xin, & Cai, M. (2020). A DFN–DEM Multi-scale Modeling Approach for Simulating Tunnel Excavation Response in Jointed Rock Masses. Rock Mechanics and Rock Engineering, 53(3), 1053–1077. https://doi.org/10.1007/s00603-019-01957-8

Watkins, H., Bond, C. E., Healy, D., & Butler, R. W. H. (2015a). Appraisal of fracture sampling methods and a new workflow to characterise heterogeneous fracture networks at outcrop. Journal of Structural Geology, 72, 67–82.

Watkins, H., Bond, C. E., Healy, D., & Butler, R. W. H. (2015b). Appraisal of fracture sampling methods and a new workflow tocharacterise heterogeneous fracture networks at outcrop. Journal of Structural Geology, 72(February), 67–82. https://doi.org/10.1016/j.jsg.2015.02.001

Welch, M. J. (n.d.). Modelling the Evolution of Natural Fracture Networks.

Westoby, M. J., Brasington, J., Glasser, N. F., Hambrey, M. J., & Reynolds, J. M. (2012). 'Structure-from-Motion'photogrammetry: A low-cost, effective tool for geoscience applications. Geomorphology, 179, 300–314.

Whaley, D. L. (2005). The interquartile range: Theory and estimation. East Tennessee State University.

Wiecek, B., & De Mey, G. (2011). Thermovision in Infrared–basics and applications. Measurement Automation Monitoring Publishing House, Warszawa.

Wilkinson, M. W., Jones, R. R., Woods, C. E., Gilment, S. R., McCaffrey, K. J. W., Kokkalas, S., & Long, J. J. (2016). A comparison of terrestrial laser scanning and structure-from-motion photogrammetry as methods for digital outcrop acquisition. Geosphere, 12(6), 1865–1880.

Wolfe, W. L., & Zissis, G. J. (1978). The Infrared handbook. The Office.

Wyllie, D. C., & Mah, C. (2004). Rock slope engineering. CRC Press.

Zar, J. H. (2005). Spearman rank correlation. Encycl Biostat.

Zhang, L., & Einstein, H. H. (1998). Estimating the mean trace length of rock discontinuities. Rock Mechanics and Rock Engineering, 31, 217–235.

Zienkiewicz, O. C. (1975). Methode derfiniten Elemente. Fachbuchverlag, Leipzig.